AN ABSTRACT OF THE DISSERTATION OF

Kenya K. Hazell for the degree of Doctor of Philosophy in Materials Science presented on June 22, 2022

Title: Potential Additive-Manufacturing of Ablative Thermal Protection Systems

Abstract approved:

_____

Vincent T. Remcho

Electrodeposition is a versatile polymer deposition technique to create nano-microscale materials using an electrical field generated from a charged droplet of solution and a grounded collector. Electrospinning or electrospraying can occur during electrodeposition, leading to the creation of nanofibers or bead-like materials depending on the process parameters. Photopolymerization of the electrodeposited solution has been used to cure the material during the flight of the charged droplets and/or produce a core-shell morphology of different polymer compositions. Acrylate monomers have been used in photopolymerization reactions due to their fast reaction time and reduction of moisture sensitivity. One drawback of acrylate monomers is the increase in oxygen-sensitivity, which requires an inert environment. The primary focus of using photopolymerization in this manuscript's evaluation was to cure the acrylate monomers during flight, in of hopes of producing a distinct film morphology.

The purpose of this manuscript's evaluation, which was conducted in collaboration with Nanovox, LLC on a NASA funded project, was to utilize electrospinning as a manufacturing method for the production of thermal protection systems (TPS). The main goal of this manuscript's evaluation was to optimize the electrodeposition process. The materials' properties obtained from the electrodeposited films were observed to determine if electrodeposition was a viable way to produce a TPS. Previous methods of manufacturing TPS are more labor intensive and expensive due to material costs. Electrospinning was investigated as an environmentally friendly alternative manufacturing technique to solve the intensive labor and material cost issues with the added benefit of possibly controlling the overall morphology of the film.

The products generated in the electrospinning process were fully cured polymer films with high thermal stability and non-porous film morphology. The most successful set-up was a vacuum chamber, which allowed for a N_2 (g) rich environment with a light vacuum applied to keep the chamber gas pressure close to atmospheric. The shape of the films was determined by the distance from the collector. As the distance increased, a higherdegree of arcing was observed. The most consistent surface morphology that was observed was a non-porous film with bumpy ridges. Upon closer inspection under the SEM, the non-porous surface appeared to have droplets that were deposited in a bead-like shape rather than a fiber-like shape, which was more indicative of electrospraying, although some indication of electrospinning was observed sporadically.

A comparative analysis of the reinforced composites found few differences between the control and reinforced films due to the lack of filler deposited. Fillers are used within TPS to provide additional structural and thermal reinforcement. The fillers aid in the production of the char layer for insulation and pores in order to allow the pyrolysis gas to travel to the surface. The majority of the filler was observed to be trapped within the plastic body of the needle before reaching the metal portion when processing the electrodeposited samples. The design of the needle's plastic body led to a reduction in the filler distribution for the reinforced composite films. The thermal

behavior of the reinforcement composite films was similar to the control because the filler distribution in the composite film was uneven. The HGMB showed a slight improvement in the thermal stability and char residual from the cast samples created.

Cure-inflight electrodeposition was shown to have successfully produced a fully cured film that exhibited high thermal stability. Electrodeposition showcased its capabilities to photopolymerize the polyhedral oligomeric silsesquioxane/aliphatic urethane acrylate monomers in flight, which is a more environmentally friendly method. While some issues did arise with the production of the reinforcement composite films, overall, electrodeposition can produce a reinforced composite film.

Potential Additive-Manufacturing of Ablative Thermal Protection Systems

By

Kenya K. Hazell

A DISSERTATION

submitted to

Oregon State University

in partial fulfillment of
the requirements for the
degree of

Doctor of Philosophy

Presented June 22, 2022
Commencement June 2023

Doctor of Philosophy dissertation of Kenya K. Hazell presented on June 22, 2022

APPROVED:

Major Professor, representing Materials Science

Head of the School of Mechanical, Industrial, and Manufacturing Engineering

Dean of the Graduate School

I understand that my dissertation will become part of the permanent collection of Oregon State University libraries. My signature below authorizes release of my dissertation to any reader upon request.

Kenya K. Hazell, Author

ACKNOWLEDGEMENTS

I would first like to acknowledge the efforts made by Dr. Julie Tucker and Dr. David Cann in helping me to complete my Ph.D. Despite everything, you both are the reason I am here and have made it to the end. You have truly made my experience within the Materials Science department a positive one.

I would like to thank my advisor, Dr. Vincent Remcho, who took me on when I needed it most and helped me to get as far as I am now in my Ph.D. My knowledge of analytical chemistry has expanded while working with you and I will continue to find why to use the skills you have taught.

Within the Remcho lab group, Saichon Sumantakul, Michelle Tran, Erin Kalbugh, Tara Hurley, Bokun Zhou, and Mia Malgrini, I have received guidance, support, and a sense of comradery. Though we did not work within the same areas, you shared your knowledge and expertise in ways that have only benefitted me. I can only hope we keep in touch as we go through life.

I would like to express sincere appreciation towards Edward Elliot from Nanovox, LLC for his contribution to the project and support and also thank the National Aeronautics and Space Administration (NASA) for funding this project under contract number 80NSSC20C0300.

Lastly, I would like to acknowledge the support and efforts of my friends and family. Your contributions and efforts have been tremendous and greatly appreciated. I can only hope I continue to turn what you have given.

CONTRIBUTION OF AUTHORS

This project was proposed by Nanovox, LCC in conjunction with OSU to help develop an alternative method for deposition of TPS. The design of the polymer system was performed by Dr. Edward Elliot, who offered materials and knowledge to help push the project forward. The mechanical properties results were collected by his lab for comparative analysis. The XRD data were collected by Tara Hurley, who also lent her knowledge of the instrument to collect the best results possible for the material. Chad Armstrong assisted with fixing and making the electrical cables needed for the power supply.

TABLE OF CONTENTS

Page

TABLE OF CONTENTS (continued)

Page

LIST OF FIGURES

Page

LIST OF FIGURES (continued)

Page

LIST OF FIGURES (continued)

Page

LIST OF FIGURES

Page

LIST OF FIGURES (continued)

Page

LIST OF TABLES

Table Page

LIST OF APPENDICES

Appendix Page

LIST OF APPENDIX FIGURES

Figure Page

LIST OF APPENDIX TABLES

Table | Page

DEDICATION

This is a dedication to my family, who has never stopped supporting me physically, mentally, and financially, and to my friends, who have been there every step of the way with some eagerly awaiting to change my server name again in our group chat.

Thank you for everything, I will always remember and appreciate it.

Chapter 1 Introduction

Over the last couple of years, there has been a growing interest in space exploration with an increase in the desire to explore another potential moon landing and investigate signs of life on other extraterrestrial bodies. While current research studies are investigating ways to detect life on different extraterrestrial planets, further research into how to protect space vehicles in varying environments is needed. More customizable materials and manufacturing methods need to be developed for components of space vehicles to improve durability upon atmospheric re-entry.[1,2] Thermal protection systems (TPS) are a primary component of space vehicles for atmospheric re-entry applications. They are responsible for shielding the space vehicle from thermal degradation due to the heat generated upon re-entry. Current high-velocity TPS consists of a heavy and expensive ablative coating which requires a labor-intensive installation due to the complex design and shape of the space vehicle's heat shield.[3,4] This also has an additional drawback of needing industry gained expertise (know-how) as the commercial systems used are "heritage" systems.[1,3] Better and more modern alternatives to manufacturing TPS are needed to address these issues and aid in the expansion of exploration for life on extraterrestrial plants.

Electrodeposition is a versatile additive manufacturing technique that requires less material, energy, and labor, and can potentially be used to produce a TPS material with the necessary specifications for different planetary bodies.[5–7] Electrospinning (ES) and electrospraying are two techniques used in this area. Electrospinning is a well-researched method for electrodeposition as shown in Figure 1.1 with an increasing number of publications published each year. The basic system design only needs three components and a dilute concentration solution, resulting in less cost and material needed to achieve a nanofiber composite film. While the basic system design is simple to develop, the process has been investigated and limited to lab-scaled research.

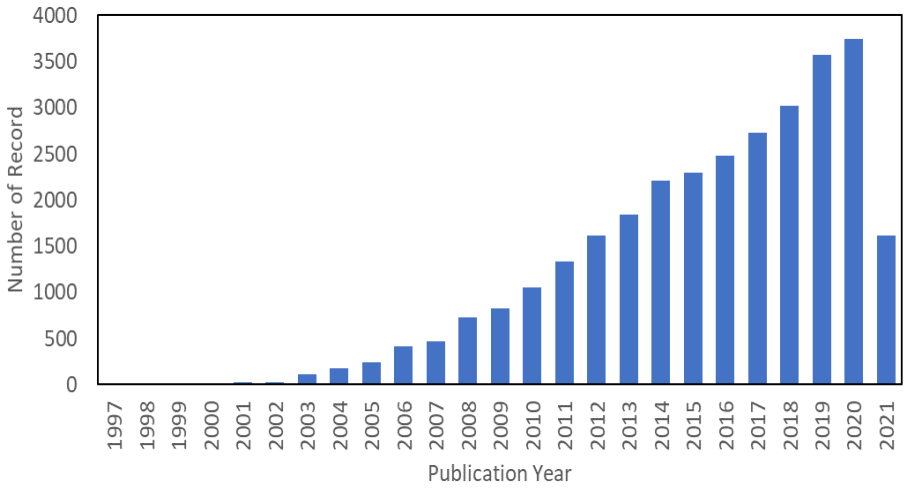

Figure 1.1: Number of publications on ES by year

This dissertation proposes to design and optimize an ES process in which a viable TPS can be produced and applied to a space vehicle for re-entry applications. The focus of this ES method is the use of an acrylo-polyhedral oligomeric silsesquioxane (A-POSS) cage mixture monomer, which exhibits the potential thermal behavior needed for a composite resin used for high-temperature thermal stability applications. Due to having an acrylo-terminated end group and its photosensitivity, it can be readily copolymerized using an ultraviolet (UV) light source, reducing the need for a heat source to be applied.

To develop an alternative TPS, this project was done in collaboration with Dr. Edward Elliot and Dr. Ngoc Nguyen from Nanovox, LLC (Beaverton, OR). The design and optimization of the ES system were executed by our lab with further optimization done in conjugation with Nanovox of the thermoset development as the project progresses. The evaluation of the ablation properties was conducted by Nanovox, LCC as well.

In order to demonstrate the potential of this new system design, several characterization experiments will be performed to ensure that the final material meets the need of National Aeronautics and Space Administration (NASA) specifications (Table 1). The initial stages of the system design will involve the development of a composite film composed of A-POSS and a secondary monomer using only UV light

in an ambient environment. The initial stage will be validated through chemical analysis using a Fourier transform infrared instrument to ensure a reaction occurred. A thermal analysis will be performed using thermal gravimetric analysis and differential scanning calorimeter to observe the thermal degradation profile, % char yield of the thermoset resin, and heat flow behavior. During the initial phase, successful electrodeposited runs will be observed under scanning electron microscopy to determine the patterning with the potential runs leading to the introduction of a filler. Once a final composite composition has been formed, further chemical and thermal analysis will be used to determine if the resultant mat has the basic properties needed before conducting ablative testing.

Table 1.1: TPS Specifications.

Metric	**Target**
Density	< 0.7 g/cm^3
Heating	> 100 W/cm^2
Char yield	> 50 %
Thermal conductivity	Low
Coefficient of thermal expansion	< 1E-6
Deposition	Direct on pre-built structure
Area	> 20 m^2
Post-cure anneal	< 350 ^oF

Chapter 2 Literature Review

2.1 Thermal Protection Systems

TPS are a critical part of space vehicles for re-entry into the earth's atmosphere or other planetary orbits. There are two types of TPS used for re-entry applications of space vehicles: reusable and ablative. Reusable TPS are used for low-velocity re-entry where the primary source of heat protection is the material's ability to reflect and re-radiate heat. Ablative TPS is used for high-velocity re-entry, where the primary mechanism used to protect the space vehicle is pyrolysis and charring of the TPS.[4,8]

An example of the TPS system is shown in Figure 2.1, with the graph depicting the boundary at which a reusable or ablative type TPS can be used depending on the Mach number, density, and altitude. On the lower end of the Mach number, a reusable TPS for the space shuttle, Orbiter (Figure 2.1 bottom-left), is shown in the black regions. For an ablative TPS, space probe for the Mars Science Laboratory mission (Figure 2.1 bottom-right), the yellow area of the space vehicle shows where the materials are applied.[3,9]

2.1.1 Ablative Mechanism

Ablative TPS are an effective shielding material due to their composition that aids in the primary mechanism for thermal protection: charring. Ablative TPS can be made from thermoset (phenolic- and epoxied-based) and thermoplastic composites with silica or carbon-based filler material.[10] The most common types of ablative TPS used are phenolic-based composites with a carbon or silica filler and carbon-carbon composites.[2,11] The charring mechanism is shown in Figure 2.2, which explains how pyrolysis begins. As a convective and radiation heat source is applied to the surface of the material upon re-entry into the atmosphere, it begins to pyrolyze. This begins the formation of the porous char (carbonaceous) layer. As the material continues to thermally and chemically degrade, pyrolysis gases diffuse through the porous char layer, cooling it and creating a gaseous layer above it, which aids in reducing the

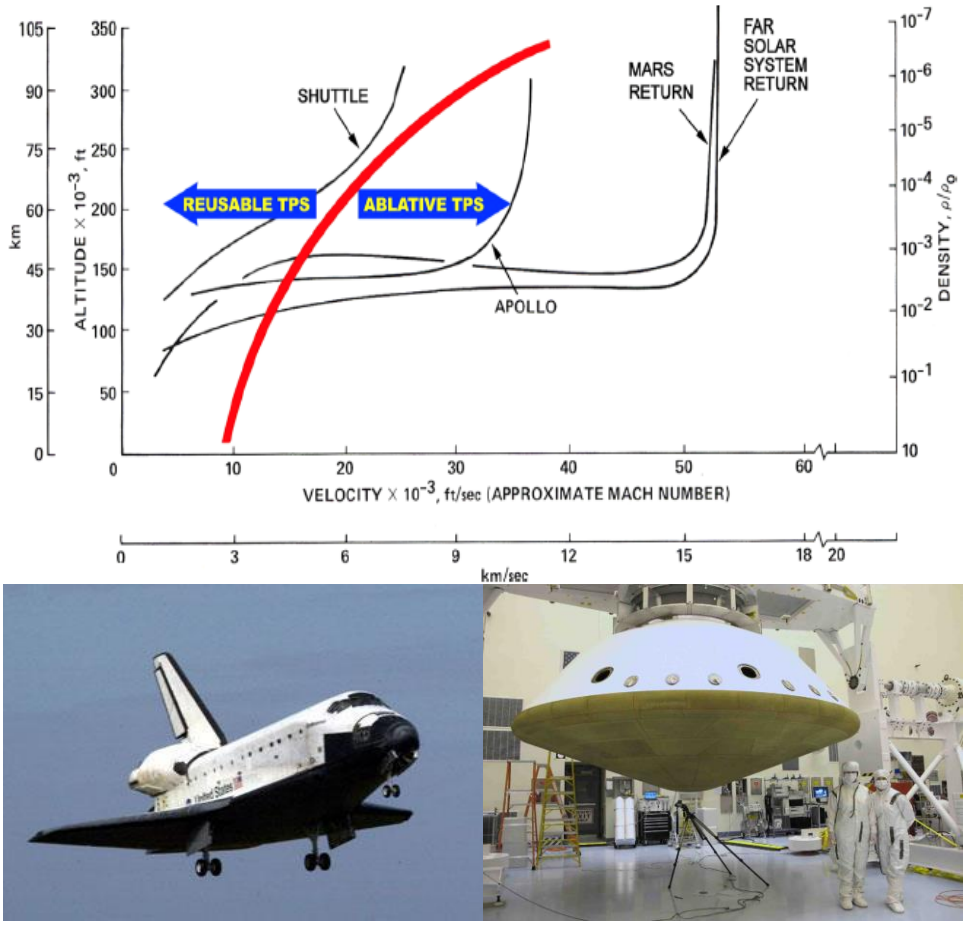

Figure 2.1: TPS used for re-entry application. The top plot depicts the velocity, density, and altitudes for past and future missions and the relative TPS used for each. The bottom images are two examples of space vehicles: a space shuttle (left) and a space probe(right).

amount of convective heat applied to the material through transpiration cooling.[12,13] The char layer continues to protect the layer of virgin material while the material is removed through further degradation and surface recession.[11,14,15] The addition of the filler helps to maintain the structural integrity of the carbonaceous layer and improve char retention.[16] The filler also acts as an additional heat sink for convective heat traveling through the TPS. The protection of the TPS degrades once the virgin material has pyrolyzed, stopping the production of the pyrolysis gas. The only insulation available, the residual char layer, is exposed to erosion from friction and mechanical forces from atmospheric pressure. This mechanism has been modeled for various systems (AVCOAT[17–20], carbon-phenolic[21,22], and carbon silica-phenolic[23]) to

improve the understanding of how the ablation is influenced by composite materials and to provide a way to simulate ablative degradation for future material designs.

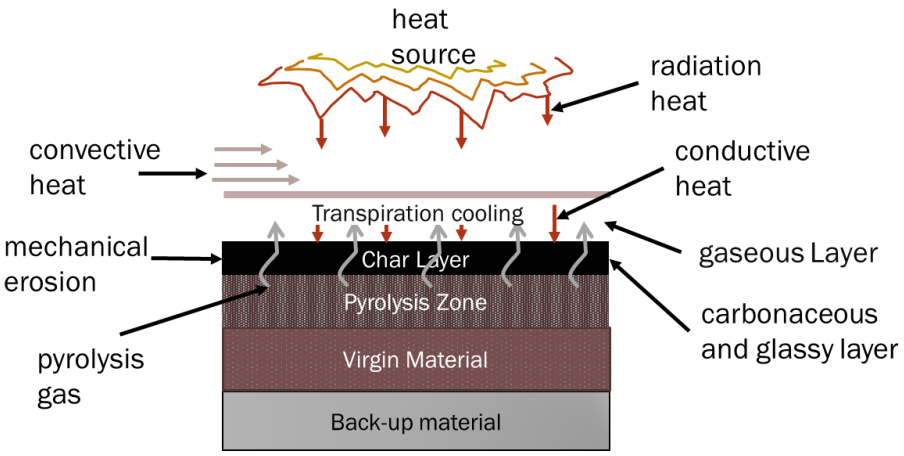

Figure 2.2: Diagram of charring mechanism (Mishra, 2020)

2.1.2 Manufacturing Methods

Typical methods of manufacturing ablative TPS depend on the type of systems used. The selection of the matrix and filler material depends on the thermal degradation behavior of both components in order to meet material specifications need and pass the arc jet test. For the matrix material, high thermal stability and the production of the char layer are important as this helps to create the carbonaceous insulation layer. The type of matrix materials used are phenolic-based (phenol-formaldehyde and resole formaldehyde), thermoplastic, and epoxy. [4,24] The types of filler used are primarily carbon and/or silica-based due to their improvement of the structure's mechanical properties, ability to decrease the TPS density, thermal, and ablative properties. The use of a filler as reinforcement has been shown to decrease the thermal degradation behavior, improve the formation of the char layer, and allow for a better degree of pyrolysis gas flow.[25] The ratio between the resin content and filler was studied by Kumar et al. for pre-preg material to investigate the optimal ratio[26] It was concluded that for pre-preg composites, 35 – 40% and 40 – 45% resin content for silica and carbon phenolic, respectively, produced the best mechanical and thermal properties. Of the current TPS explored today, the most common ones known are AVCOAT and PICA.

The AVCOAT system, a mid-density TPS, comprises a phenolic glass fiber reinforced honeycomb structure filled with an epoxy-phenolic matrix reinforced with phenolic microspheres and silica fibers. A nine-step process is required to manufacture AVCOAT as shown in Figure 2.3.[3] What makes this process labor-intensive, is that each honeycomb hole must be filled individually and due to the rigidness of the material, it must be made part by part in order to assemble onto the shielding body. It is expensive to manufacture as this process uses aged-out materials which would be considered special commodity materials. [3,4,27]

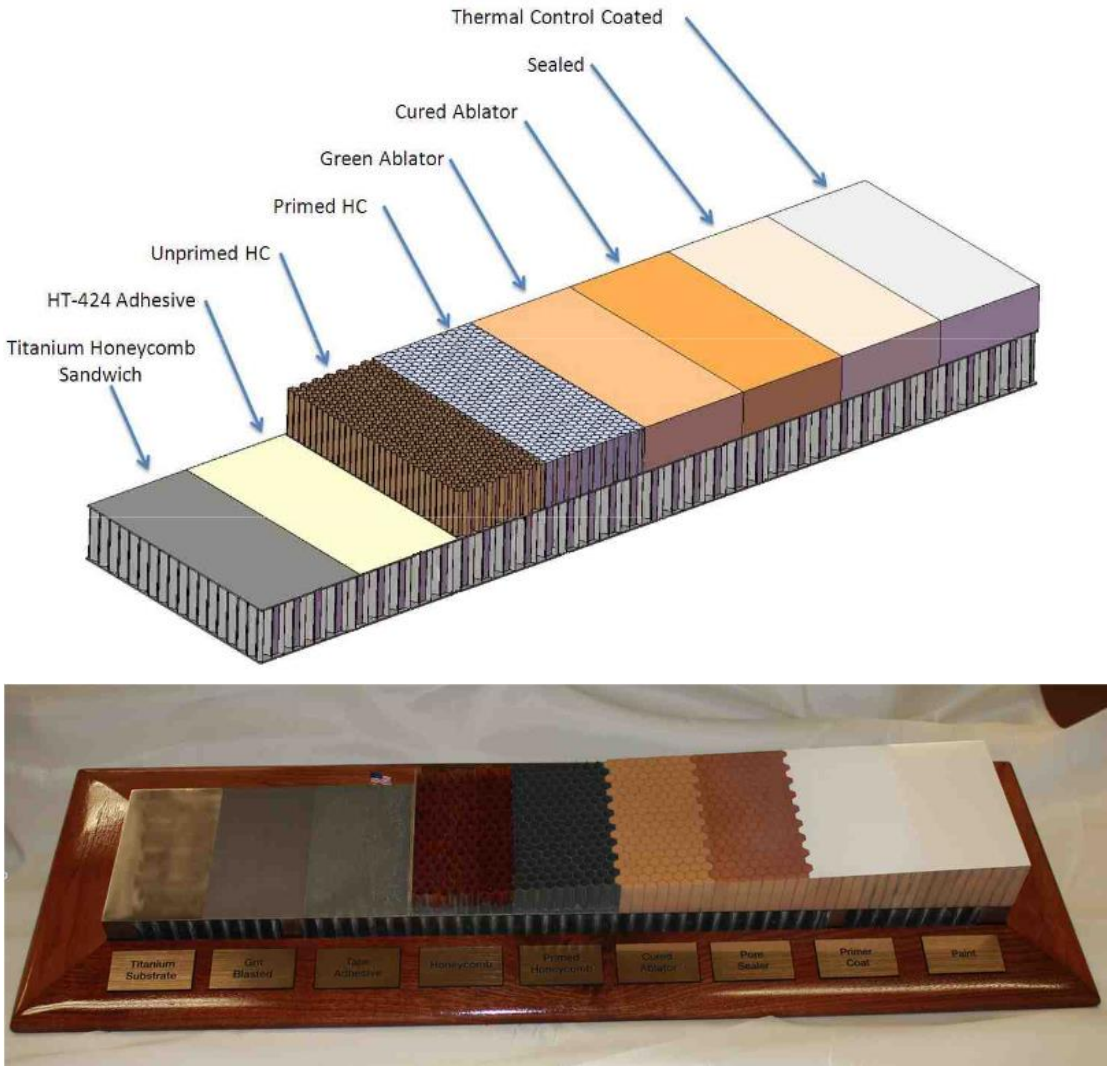

Figure 2.3: AVCOAT manufacturing process (NASA, 2020)

The phenolic impregnated carbon ablator (PICA) is a type of low-density ceramic ablator offered as a competitive alternative to ablators such as the AVCOAT. [24] PICA is comprised of carbon felt and fiber form that is impregnated with a water-soluble phenolic resin before going through a curing and drying cycle. PICA is cheaper to manufacture compared to the AVCOAT and is used in a tiled configuration which offers some disadvantages from potential defects generated at the seams.

2.2 Electrospinning

ES is a well-developed electrohydrodynamic process for the production of micro- to nanoscale fibers that was first theorized by William Gilbert in the late 1600s. The original concept was developed from the observation of the phenomena of applying an electric field to a water droplet. [28] This concept was later expanded upon by Bose in 1745, who observed the formation of aerosols using electrical potential[6], Lord Rayleigh in 1885, who studied the amount of electrical charge needed to eject a jet from a charged droplet[29], and G. I. Taylor, for which the "Taylor cone" is attributed to for his calculation of conical deformed droplet.[30] By 1902 and 1903, this technique was patented by John Cooley and William Moore, respectively.[31,32] As technological advancements were made, a resurgence in researching electrospinning begin in the late 1990s within research groups led by Darrell Reneker[33–35] and Gregory Rutledge[36,36–39] beginning to investigate the theory and develop the fundamentals of how this process works. Since then, many studies have been performed on how to apply, optimize, and expand upon its capabilities.[5,6]

2.2.1 Electrospinning Process

Electrospinning is a process that can be simplified into a few steps.[40–42] The initial step is the extrusion of the solution through the needle or capillary tube to form a droplet using surface tension forces. This is then followed by the application of an electric field at the tip of the nozzle, creating a charged droplet that leads to the formation of a Taylor cone (a deformed droplet). Once the Taylor cone is formed, electrostatic charges of similar signs begin to repel each other causing a jet to eject in a straight line from the Taylor cone once the limit for the electrostatic repulsion

forces is reached. As the acceleration of the jet reaches a constant value, instabilities (Rayleigh, bending, or axisymmetric) can occur at the end of the straight-line region as shown in Figure 2.4.[33,34] The instability region of the jet reaches the grounded collector, where the material is then deposited onto the surface, forming micro- to nano-scale fibers with varying morphologies. The morphologies of the fibers are influenced by many parameters including the length of the straight-line and instability region as stretching and expansion of the jet primarily occur.[41,43,44]

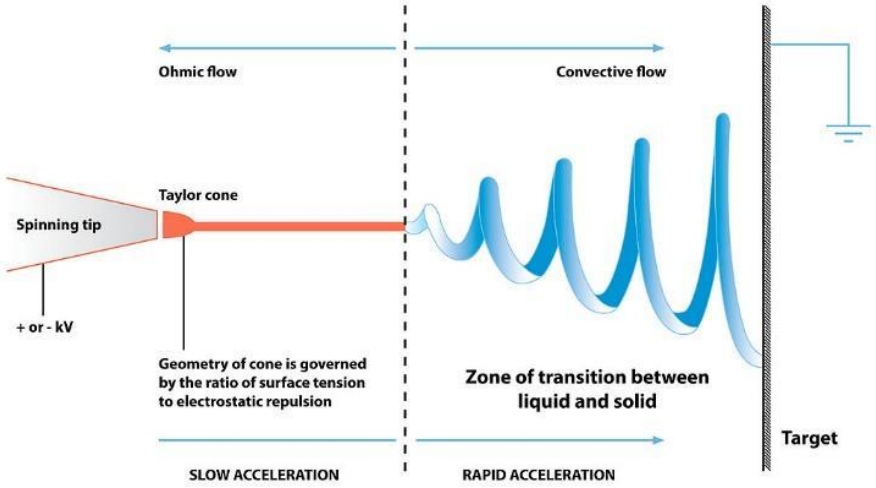

Figure 2.4: ES diagram depicts the region of fluid flow for a charged droplet. The ohmic region is driven by the electrical charge of the droplets while the convective flow is the instability region in which the spinning occurs. (Wiki, 2020)

2.2.2 Theory

The theory behind ES can be divided into different regions in order to understand how the electrostatic and viscoelastic forces affect the solution in a way to form micro- to nano-scale fibers.[40,45] The initial droplet formation in the viscoelastic region is caused by surface tension forces which produce a straight-line jet. The straight jet region relies on viscoelastic forces and electrostatic forces to drive the fluid towards the collector. [35,46,47] The fluid jet's aerodynamics and trajectory can be investigated in the bending instability region as this region helped to produce the nanoscale fibers which are the desired product.[48] The theoretical model for the jet's path can be described using four governing equations: the conservation of mass (Eq. 1),

conservation of charge (Eq. 2), conservation of momentum (Eq. 3), and Coulomb's law (Eq. 4).

Conservation of mass (Q)

$$\frac{\boldsymbol{d(\pi R^2 v)}}{\boldsymbol{dz}} = \mathbf{0} \qquad \text{Eq. 1}$$

R = radial component [m]

v = kinematic viscosity [m^2/s]

Conservation of charge (I)

$$\frac{\boldsymbol{d}}{\boldsymbol{dz}}\left(\boldsymbol{2\pi R\sigma v + \pi R^2 KE}\right) = \mathbf{0} \qquad \text{Eq. 2}$$

σ = surface charge density [C/m^2]

K = conductivity of the liquid [S/m]

E = axial(x)-component of the electric field [N/C]

Conservation of momentum (linear momentum)

$$\frac{d(\pi R^2 \rho v^2)}{dz} = \pi R^2 \rho g + \frac{d}{dz}\left(\pi R^2(-P + \tau_{zz})\right) + \frac{\gamma}{R}\left(2\pi R\left(\frac{dR}{dx}\right)\right) + 2\pi R\left(t_t^e - t_n^e\left(\frac{dR}{dz}\right)\right) \qquad \text{Eq. 3}$$

ρ = liquid density [kg/m^3]

P = pressure [N/m^2]

g = gravitational acceleration [m/s^2]

τ_{zz} = axial viscous normal stress [N/m^2]

γ = surface tension [mN/m]

t_t^e = tangential tractions on the surface of the jet due to electricity [N/m^2]

t_n^e = normal tractions on the surface of the jet due to electricity [N/m^2]

Coulomb's integral for tangential electric field inside the jet

$$E - \ln\frac{1}{x}\left[\frac{\beta}{2}\frac{d^2(R^2E)}{dz^2} - \frac{1}{\epsilon_{air}}\frac{d(\sigma R)}{dz}\right] = E_\infty \qquad \text{Eq. 4}$$

x = axial component [m]

β = charge induction = $\frac{\varepsilon}{\bar{\varepsilon}} - 1$

ϵ = fluid dielectric constant

$\bar{\varepsilon}$ or ϵ_{air} = air dielectric constant

The ohmic flow region (viscoelastic region) is driven by the electrical charge droplet. While the Taylor cone is the conical shape most mentioned as a visual indicator of the electrostatic overcoming the surface tension forces, Yarin et al, report that the production of a half cone shape works as well as an increase in the voltage tends to shrink the shape of the cone producing a smaller half-cone.[35] It was also reported by Yangying et al., that slope of the jet current and portion of the Taylor cone of the nozzle influences the uniformity of the fibers.[49]

The bending instability region has been heavily investigated to produce a better understanding of the jet's path, fiber formation, and the reasoning behind the instability or whipping that occurs along the jet path.[39] The bending instability region was modeled by Reneker et al, to explain how it is caused and to provide a mathematical model of this region.[33] The mathematical model was further explained to predict the jet's path for a test solution of PEO in water/ethanol. The mathematical model corresponded with experimental data when solvent evaporation was taken into account, however, the model was limited by a lack of knowledge of the rheological changes the solution undergoes as it travels to the grounded collector. A study conducted by Hohman et al. found that bending instability was influenced by the surface charge density of the droplet and the radius of the initial jet. The phenomena of jet branching and beading were observed by Yarin and Reneker, showing that a higher applied voltage the production of beading will occur along with an increase in branching within the bending region, and later studied by Lee and Sallam, who

concluded that a greater degree of instability led to thinner fibers due to jet branching.[45,50] The effect of buckling instability on a patterned deposition was investigated by Han et al and Reneker and Xin.[51,52] Han et al. conducted a comparison experiment between charged and uncharged jets to note the buckling frequency influenced by the velocity and diameter of the jet, as well as the viscosity and density of the solution. Reneker and Xin looked at the effect that voltage and distance had on the bending pattern produced during fiber collection.[52] It was observed that distance played a part in determining the shape of the bending after a voltage was selected which produced a straight jet, the control variable.

2.2.3 Parameters

One of the advantages of ES is the simplicity of the processing method which works by passing a polymer solution through an electric field generated at the tip of a nozzle or syringe needle, electrifying the solution droplets to deposit onto a grounded substrate ES consists of three major components: high voltage power supply, syringe needle or capillary tube, and a ground collector. The voltage supply drives the process by generating an electric field which enables the polymer solution to disperse onto the collector in a designated pattern based on the processing parameters. The resultant fiber diameter is influenced by the size of the needle diameter as well as other factors in the process.[41,53] The key parameters for electrospinning are shown in Table 2.1. The solution properties, while not essential to ES the polymer, are important for understanding how the ES parameters and fiber morphology are affected by them.

Table 2.1: Key solution properties and ES parameters

Solution properties	**ES parameters**
Viscosity	Applied Voltage
Conductivity	Distance from needle to the collector
Polymer concentration	Solution feed rate
Surface tension	Needle diameter
Molecular weight	Humidity/Temperature
	ES environment

The fiber morphology is influenced by viscosity, molecular weight, polymer concentration, and surface tension. The formation of fiber, rather than beads, depends

on reducing the viscosity and surface tension while maintaining a high enough molecular weight and polymer concentration. When aiming for a fiber-like morphology, is it important to observe these solution properties when troubleshooting the process. To ensure that fiber formation is obtained, the polymer concentration is a factor that can be increased to increase fiber formation and reduce the presence of spherical particles. In terms of the ES solution parameters, an increase in surface tension and concentration will lead to an increase in applied voltage needed to produce the charged jet. Increasing surface tension can also increase the formation of beaded fibers. A change in molecular weight, concentration, and viscosity will affect the flow rate with an increase leading to a lower flow rate. The fiber morphology is influenced by the ES process parameters as well. The distance to the collector can influence the fiber diameter, distribution, and morphology[54]. As the electric field or solution path can be divided into two regions (straight jet and bending region), the fiber morphology is influenced by where the ground collector is placed: by the end of the jet region (near-field ES)[43,55,56] or further into the bending region (far-field ES).[57–59] This parameter has also been used to produce order or aligned nanofibers.[60] The applied voltage also determines the product. Too much charge is more likely to produce an electrospray pattern with droplets instead of the desired fiber-like pattern. Charge density is also a factor that affects fiber formation as a higher charge density can lead to thinner fibers due to jet branching. The flow rate of the solution helps to drive the fiber formation and morphology, as faster flow rates can increase the chance of beads forming. An increase in flow rate increases the fiber diameters but can also drive the system away from electrospinning if too high. For the ES environment, humidity can affect the beading size and fiber length as it can influence solvent evaporation.[61]

2.2.4 Applications

ES has been used in various fields from biomedical to textiles to improve the material properties or manufacturing process of a product. Within the textile field, ES has been used to produce synthetic silk. [41] In the biomedical field, it is a way to manufacture wound dressing made with modified organic frameworks and polylactic acid [62,63] or

engineer tissue scaffolds with collagen, silk, or chitin.[64,65] Within the composites field, ES has been used as a method to produce nanoscale fiber mats with or without reinforcement materials[6,66] and filtration membranes.[67,68] ES has also been used for melt spinning applications[69,70], ES with a pure polymer above its glass transition temperature, and gel spinning[71] While using ES has been used for unique applications, the ability to scale up this process is hampered by a lack of control over the fiber orientation/position, which while address in some papers is still a limitation, the low mass produced due to dilute solutions, and polymer material applicable for this method mainly polymer which can be readily dissolved volatile solvents.[72]

2.3 Photopolymerization

Photopolymerization is a processing method used with photocurable polymers, allowing one to polymerize a monomer or monomer mixture without the necessity of heat or additional chemicals. Photopolymerization is environmentally friendly, due to its applicability with solvent-free systems, reduction of volatile organic compound by-products, and faster and energy-efficient reaction times without requiring heat to drive the reaction.[73–76] Water-based acrylate monomers were studied for their properties as a potential "greener" coating.[77,78]

ES with in-situ photopolymerization (or curing in-flight ES) is a technique used due to its ability to influence the fiber morphology by taking advantage of the photosensitivity of select polymers.[79,80] The curing in-flight technique has been used to produce "core and shell" morphology using thio-lene click chemistry to control the overall composition across the fiber diameter and create fibers with unique morphologies.[44,81,82] This technique has been applied to the sample as it hits the grounded collector as well as during its flight path. Despite these advantages, photopolymerization reactions are limited depending on the type of reactions. For this dissertation, a free-radical vinyl photopolymerization reaction was used for the formation of the composite film.

2.3.1 Free radical polymerization

Free radical polymerization is a reaction driven by radical addition commonly initiated in the presence of an initiator. Falling within the category of chain-growth polymerization, it consists of three steps: initiation, propagation, and termination. The initiation step starts with the creation of the free radicals (Eq. 5) mainly using heat, photonic light, or electrochemical sources.[83] The free radical generated will then react with a monomer to make a monomer radical (Eq. 6). Once the monomeric free radicals are created, the propagation step (Eq. 7) occurs, reacting the monomers to create the polymer chain. During this step, the rate of propagation can be affected by the reactivity of the monomer and the active polymer chain along with the temperature of the reaction. Any interactions between the active polymer chains will reduce the rate the propagation before the reaction reaches the end. This step will continue until the termination step (Eq. 8) which occurs either due to quenching or when the initiator concentration is low.

Free radical formation	$I \overset{k_d}{\rightarrow} 2R\cdot$	Eq. 5
Initiation	$R\cdot + M \overset{k_i}{\rightarrow} RM\cdot$	Eq. 6
Propagation	$RM\cdot + nM \overset{k_p}{\rightarrow} P_{\mathrm{n}} + 1$	Eq. 7
Termination	$P_{\mathrm{n}}\cdot + P_{\mathrm{m}}\cdot \overset{k_t}{\rightarrow} polymer$	Eq. 8

I = initiator
R = radical molecule
M = monomer
n = mole of monomer
P = polymer chain; subscript denotes growing chain length
k_i = rate constant for that reaction step

Three ways in which the reaction can be terminated are combination, disproportionation, and chain transfer. Combination (Eq. 9) is the reaction of two

separate polymer chains to create one long inactive polymer. Disproportionation and chain transfer both prematurely terminate active polymer chains, with disproportionation (Eq. 10) occurring when one active polymer chain removes a proton from another active polymer chain creating two inactive polymer chains and chain transfer (Eq. 11) using a free radical created from anything within in the reaction (solvent, monomer, photoinitiator, or inactive polymer) to remove a proton from an active polymer chain. Combination and disproportionation are common ways to terminate a reaction with combination happening more frequently as disproportionation requires more energy to occur. Chain transfer termination is often used to create polymers with lower molecular weight.

Combination	$P_x^{\cdot} + P_y^{\cdot} \xrightarrow{k_{t,c}} P_x P_y$	Eq. 9
Disproportionation	$P_x^{\cdot} + P_y^{\cdot} \xrightarrow{k_{t,d}} P_x + P_y$	Eq. 10
Chain Transfer	$P_x^{\cdot} + T - X \xrightarrow{k_{t,xt}} P_x - X + T^{\cdot}$	Eq. 11

Vinyl polymerization, a common type of free radical polymerization, is a reaction between two carbon-carbon double molecules. This reaction is beneficial as the photopolymerization method can be used to react vinyl monomers. Characteristics of this method are a fast reaction time and lower sensitivity to moisture compared to other polymerization reaction types, such as catatonic polymerization.[84,85] However, reactions involving acrylates have a greater sensitivity to oxygen leading to a higher degree of inhibition when conducted in an oxygen-rich environment. Due to this, oxygen can be used to terminate the reaction as the free radical scavenger.

When selecting a system for photopolymerization, it is important to consider the reactivity of the monomers and photoinitiator, the intensity of the light source, and solvent interactions. For the monomers, reactivity plays a part in determining the rate of the reaction for the propagation step as well as determining the final structure of the polymer. The reactivity of the monomer can depend on steric hindrance, polarity, and resonance of the molecular structure.[86] An example of this is the decreasing reactivity of the following monomers: butadiene > styrene > methyl methacrylate >

acrylonitrile > methyl acrylate > vinyl ethyl ether.[87,88] This plays an important role in copolymerization reactions. Copolymerization are reactions in which 2 or more monomers interact with one another to form a mixed polymer chain. Different types of copolymers formed are block, alternate, graft, and random. As shown in Eq. 12 - 15, copolymerization can occur in any of the four ways. The formation of the polymer chain depends on the reactivity of the 2 monomers. Equation 16 and 17 shows how each monomer reactivity is determined using the values for r_1 and r_2.

$$M_1^{\cdot} + M_1 \xrightarrow{k_{11}} M_1M_1^{\cdot} \quad \text{Eq. 12}$$

$$M_1^{\cdot} + M_2 \xrightarrow{k_{12}} M_1M_2^{\cdot} \quad \text{Eq. 13}$$

$$M_2^{\cdot} + M_1 \xrightarrow{k_{21}} M_2M_1^{\cdot} \quad \text{Eq. 14}$$

$$M_2^{\cdot} + M_2 \xrightarrow{k_{22}} M_2M_2^{\cdot} \quad \text{Eq. 15}$$

M_1 = first monomer

M_2 = second monomer

k_{ij} = rate constant of the rate

If $r_1 > 1$, the first monomer is more likely to react with itself first before it reacts with the second monomer. If $r_1 < 1$, the 2nd monomer will have a similar reaction. An ideal copolymer reaction has a $r_1 r_2 = 1$. While this is unlikely to happen realistically, having a $r_1 r_2$ value closer to 1 is preferred to ensure interaction between the two monomers.

$$r_1 = \frac{k_{11}}{k_{12}} \quad \text{Eq. 16}$$

$$r_2 = \frac{k_{22}}{k_{21}} \quad \text{Eq. 17}$$

Monomers with 2 or alkene bonds tend to lead to branching from the main chain and aid in crosslinking to create a network polymer. This effect is reduced to varying degrees when working with diluted solutions compared to pure mixtures. Monomers with aliphatic acrylates and aromatic rings were observed by Bowman et al. to have a reduction in reactivity.[89] The degree of crosslink in dilution solution was observed to contribute to the physical properties of the polymer. Solutions with low

concentrations saw more of a gel effect in select solvents with some swelling while high concentration solutions led to more brittle polymers.[90] Within dilute solutions, the presence of dissolved oxygen contributes to the reduction in polymer molecular weight. This can be resolved by sparging the solvent with an inert gas prior to or during the reaction.

The photoinitiator is the primary driver of photopolymerization. Selecting the correct photoinitiator is important to obtain the desired result. There are two types of initiators, Norrish I and II, which are characterized by how they generate the free radical. Norrish I photoinitiators generate a free radical through a homolytic cleavage or fragmentation of the molecule chain.[91] As shown in Eq. 18, the cleavage of phosphine oxide between the carbonyl and phosphonyl occurs to generate two radicals. Examples of type I photoinitiators are peroxides, benzoin ethers, dialkoxyacetophenones, oxyamines, and phosphine oxide derivatives.[92] For Norrish II photoinitiators (eq. 19 and 20), a radical is generated either upon a hydrogen abstraction in which hydrogen is donated to form 2 radicals or upon an electron transfer to an electron/photoinitiators donor to form a radical. Examples of type II photoinitiators are benzophenone, coumarin, thioxanthone, and diketones. These typically consist of two-components systems with methyl diethanol amine, mercaptans, and benzoxazines known as hydrogen donors/ co-initiators, and diphenyl iodonium salt and benzophenone/phosphonium salt are electron acceptors.[92]

Norrish type I photoinitiators typically demonstrate high reactivity and thermal stability and are used for clear coatings. The reactivity of the photoinitiator is affected by the molecular structure and efficiency of the photochemical process. The molecular structure factors into the amount of light absorbed at a specific wavelength range (250 - 450 nm), and the ability of the molecule to transfer electrons and diffuse through the reactive medium during polymerization. The efficiency of the photochemical process determines the yield and whether it is likely to be quenched by other molecules within the reaction. Other factors to consider when picking a photoinitiator are odor produced, potential yellowing, photodegradation, degree of oxygen quenching, etc. The efficiency of photoinitiators was studied by Lee et al.

using real-time FTIR[93] and photocuring DSC[94]. It was found that the presence of a ketone functional group performed better when curing in the air with a higher degree of conversion. In another study by Tauber et al., diphenyl(2,4,6-trimethylbenzoyl)phosphine oxide (TPO) was found to not be suited to curing aqueous polyurethane acrylate due to having a higher molecular weight which led to restrictions in diffusion as the curing progress.[95] It was also reported that polymerization increased with increasing photoinitiators and UV intensity, and in an inert environment.

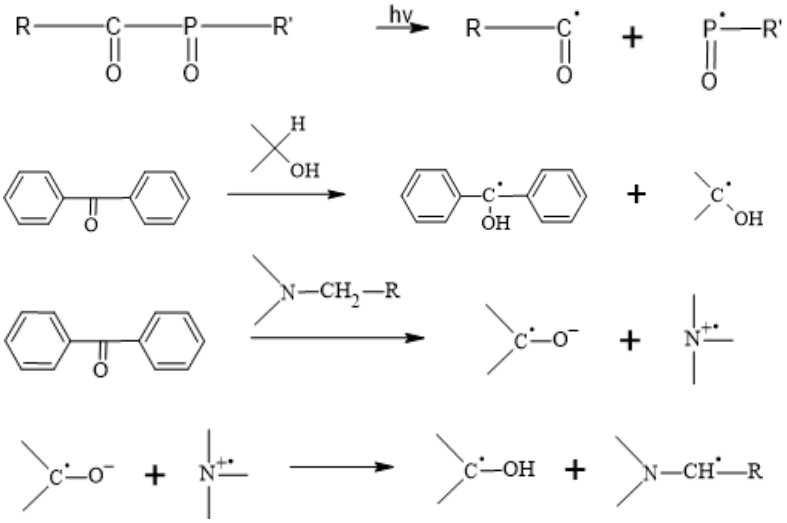

Eq. 18

Eq. 19

Fouassier, 2021[91]

Eq. 20

Fouassier, 2021[91]

One issue with free radical polymerization is the diffusion of the free radicals through the polymer medium. As the polymer chains grow and the degree of crosslinking increases creating polymer clusters, which become networks, diffusion of the free radical becomes more difficult. This eventually leads to a cage effect, where the free radicals are trapped.[96] Due to this, termination of photopolymerization reactions is caused by both combination and chain transfers. A way to estimate the chain length for such reactions is shown in Eq. 21, where the number of functional groups is considered along with the number of radicals generated. As UV intensity contributes to the generation of free radicals, the use of filter light or filler within the monomer mixture was found to reduce cure speed.[97] Similar results were found with low photoinitiator concentration or efficiency and poor reactivity monomers or functional oligomers.[98]

$$v = \frac{x n_{m0}}{n_{rg}} \qquad \text{Eq. 21}$$

x = conversion of functional group

n_{m0} = initial number of functional groups

n_{rg} = total number of radicals generated

Oxygen inhibition becomes more prominent when ES. As the solution droplets travel down the flight path and get smaller and smaller, so does the concentration of the photoinitiator until only a small amount is left. The result is an environment around the droplet with a higher oxygen concentration than the polymer itself, inhibiting the reaction. This disadvantage is addressed by carrying out the reaction in an inert environment using nitrogen gas or other non-reactive gas and/or increasing the amount of photoinitiator used to overcome the inhibition.[98,99]

2.4 Polyhedral oligomeric silsesquioxane

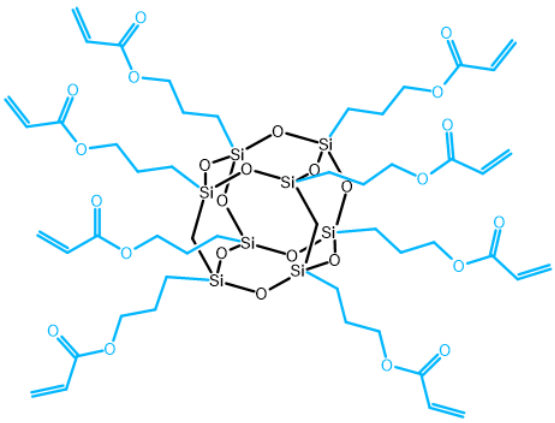

Figure 2.5: Acrylic POSS Cage Mixture

Polyhedral oligomeric silsesquioxane (POSS) is a molecule with an inorganic framework and an organic branch group that exhibits enhanced mechanical properties, thermal stability, and ablation performance. Due to its inorganic framework, POSS can achieve higher thermal stability than most acrylic-based polymers.[100] The silicon-oxide base aids in ablation properties since silica has been known to exhibit high performance for ablation applications.[101,102] POSS monomers are typically paired with two or more monomers to enhance the overall composites' material properties. Various studies have been performed utilizing POSS molecules as either a filler[103,104] or matrix[105,106] material to improve the thermal[107–110], mechanical[111], ablation[112–114], electrical[115,116], and chemical[117,118] properties. In terms of TPS applications, Philips et al. highlighted that

development of the SiO2 layer under ablation introduced the potential for self-healing while under thermal stress.[119] Kim et al. studied the mechanism in which nanocomposites mitigate thermal damage under oxygen bombardment.[120] It was found that the silica cage structure aided in shielding the matrix polymer and preventing the delamination with the formation of a ceramic char layer. Wang et al. investigated the anti-oxidation properties of POSS when incorporated into phenolic resins finding an increase in the onset temperature for thermal degradation.[121] POSS molecules also have been successfully electrospun as both filler and polymer materials for different applications.[122–127] For this project, a POSS monomer was paired with an urethane acrylate monomer to produce a flexible composite with thermal and ablative capabilities. POSS/polyurethane acrylate composites have been reported to increase flexibility while maintaining thermal stability.[128–130]

Chapter 3 Materials and method

The materials used in this dissertation were donated by Nanovox, LLC (Beaverton, OR, USA). The MA0736 acrylo polyhedral oligomeric silsesquioxane (A-POSS) cage mixture was obtained from Hybrid Plastics (Hattiesburg, MS), with the aliphatic urethane acrylate monomer, Ebecryl ® 4858 (EB), from Allnex GmbH (Germany). Other monomers explored were methyl 2-((allyloxy)methyl)acrylate (AOMA^{TM}, Nippon Shokubai Co., Ltd., Japan), diethylene glycol diacrylate (DEDGA, Sartomer, Exton, PA), diurethane dimethacrylate (DUDMA, (Sigma-Aldrich, St. Louis, MO), tetraethylene glycol diacrylate (TEDGA, Polysciences, Inc., Warrington, PA), and bisphenol A ethylene acrylate (BPAEA, Aldrich, St. Louis, MO). The photoinitiator used was diphenyl(2,4,6-trimethylbenzoyl)phosphine oxide (TPO) from Aldrich (St. Louis, MO).

The solvents used were ethanol (VWR, Radnor, PA), acetone (PharmCo by Greenfield Global, Brookfield, CT, USA), and tetrahydrofuran (THF, EMD Millipore Corporation, Billerica, MA, USA). The filler components were 1/16” milled glass fibers (MGF), hollow glass microballoons (HGMB), and microphenoset (MP) (cured phenol-formaldehyde spheres) from Fibre Glast Development Corporation (Brookville, OH), Alumlite (Kalamazoo, MI), and Malayan Adhesives and Chemicals (Selangor, Malaysia), respectively. For the dyes trials, the materials selected were thymol blue (Alfa Aesar, Tewksbury, MA), methylene red sodium salt (Alfa Aesar, Tewksbury, MA), quinaldine red (Alfa Aesar, Tewksbury, MA), coumarin 500 (Lambda Physik GmbH, Germany), rhodamine B (Eastman, Rochester, NY), azobenzene (Aldrich, St. Louis, MO), O-dianiside dihydrochloride (Sigma Aldrich, St. Louis, MO), acid yellow 34 (MP Biomedicals LLC, Solon, OH), fluorescein (Lambda Physik GmbH, Goettingen, Germany), methylene blue sodium salt (Beantown Chemical, Hudson, NH), and iodine (Sigma-Aldrich, St. Louis, MO).

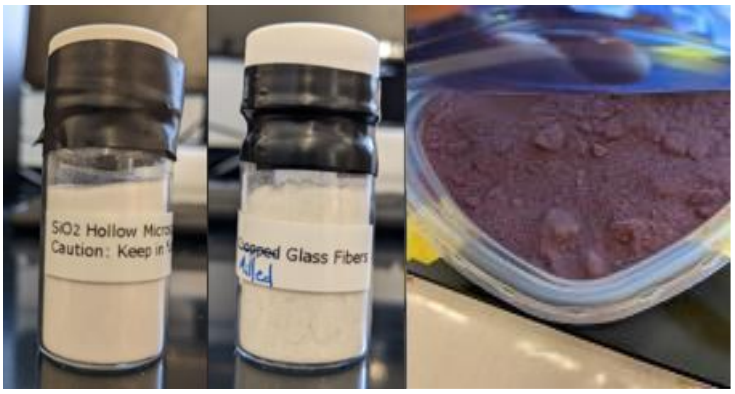

Figure 3.1: Filler appearance. HGMB (left), GF (middle), and MP (right)

3.1 Polymer solution

Each polymer solution had a 1:1 ratio of both monomers with a photoinitiator concentration of 3-5% w/v relative to the total amount of monomer in the solution. The solvents explored were ethanol, acetone, and THF. After the monomers and photoinitiator were added to the sample vial, a portion of the solvent volume was added. The mixture was sonicated for 60 minutes to dissolve the TPO before the rest of the solvent volume was added. The mixture was stirred overnight using a magnetic stirrer to further homogenize the solution. With the addition of fillers, 5 - 15% of the total weight of monomers and photoinitiator was used and added in after the control solution was mixed overnight.

3.2 ES System

The ES apparatus used for this dissertation is based on previous in-house designs, as shown in Figure 3.2 and Figure 3.3. Modifications were made to the apparatus to improve the stability of the needle position and allow for the application of UV curing in-flight along the ES path. The door for the unit was modified to allow for UV light sources to be applied using different types of lamps: xenon and mercury.

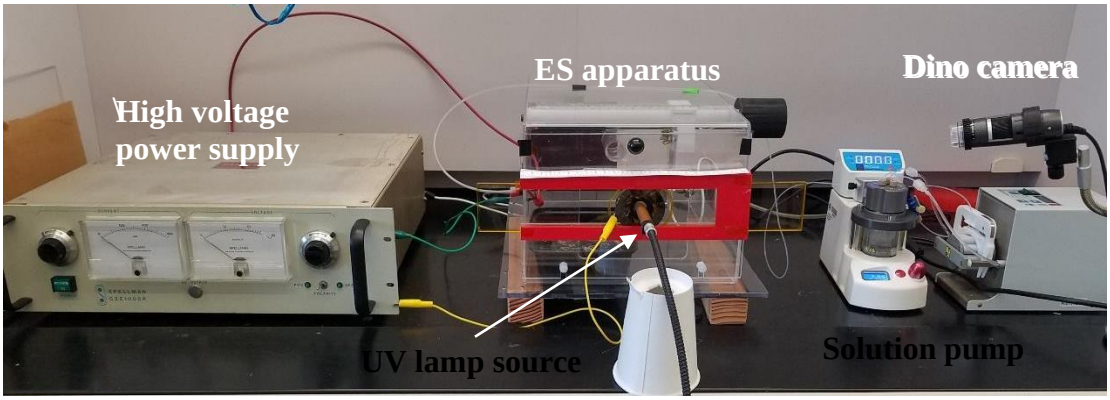

Figure 3.2: Initial ES set-up

The high voltage power supplies were a Spellman CZE1000R with a max voltage of 30 kV and a Deluxe dual power supply (10 V max) connected to an amplifier, TREK model 10-1 with a max voltage of 10 kV. The syringe pumps were a Harvard Apparatus PhD 2000 and Pump 33. The UV lamps used to cure the polymer were a Hamamatsu Photonics K.K. lamp house unit continuous mode xenon lamp (Model E7536) and an EFO Novacure 100 W mercury lamp (Model #N2001-A1). The digital microscope used to observe the ES operation was a Dino camera. The relative humidity and temperature were measured with a ThermoPro TP50 digital hygrometer placed within the fume hood.

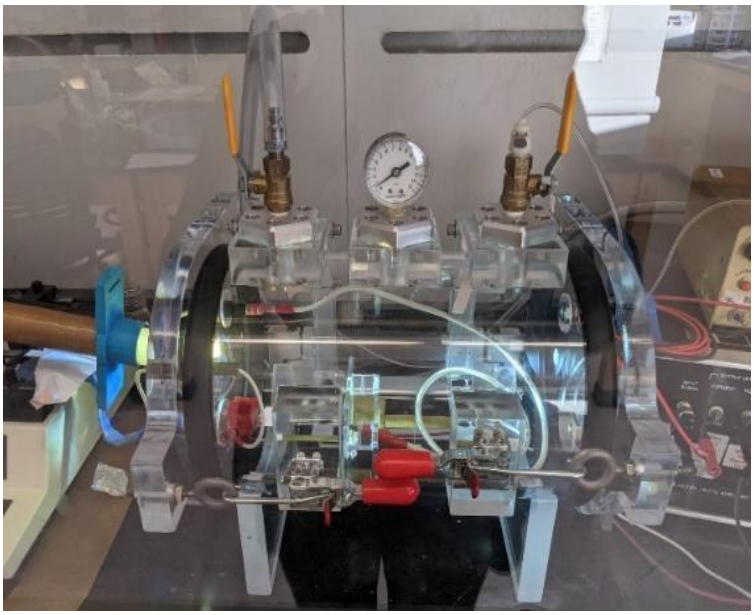

Figure 3.3: ES vacuum chamber set-up

The set-up shown in Figure 3.2, is for the ES process conducted in an atmospheric environment, where the UV light source was positioned either parallel or perpendicular to the jet path right to determine which provided the most efficient curing. The collector used to deposit the film sample was either an aluminum foil or a standard SEM stub for future SEM measurements. The next setup, shown in Figure 3.3, was a vacuum chamber with a vacuum applied at the left inlet and nitrogen introduced on the right to reduce the presence of oxygen and improve the cure rate of the electrodeposited polymers. The needle gauges used are shown in Table 3.1, depicting the relative inner diameter of the needle to the gauge values.

Table 3.1: Inner diameter of the needle in relation to gauge size

Needle Gauge	Color	Diameter [mm]
18	Pink	0.99
20	Yellow	0.64
22	Black	0.46
25	Dark blue	0.30
27	Grey	0.22
30	Lavender	0.15

3.3 Characterization

A series of image, chemical, and thermal analyses were performed to evaluate that the composite's properties met the specifications stated in Table 1.

3.3.1 Image Analysis

Figure 3.4: Scanning electron microscope

Scanning electron microscopy (SEM, FEI Quanta 600), shown in Figure 3.4, was used to determine the surface morphology and deposition pattern of the films. The samples were coated with Au-Pd for 30 seconds before imaging to make the surface conductive with copper tape to adhere the sample to the stub. Optical light microscopy (Carl Zeiss Axio, Image1m) was used to detect the presence of fillers in the reinforced composites and compare the macro features of the films. The filler length/diameter was

measured using ImageJ. Further image analysis was performed using an energy dispersive x-ray (EDX) on the SEM to obtain an elemental analysis of the surface for a sample before and after thermal degradation.

3.3.2 Chemical Analysis

The chemical composition of the thermoset resin solution (uncured and cured) was determined using FT-IR (Perkin Elmer Spectrum Two) using an attenuated total reflection (ATR) set-up with a wavelength range of 400 to 4000 cm^{-1} for 16- 64 scans. The crystallinity of the composites was measured using x-ray powder diffraction (XRD, Rigaku Miniflex 600) with a Cu-K_{a1} source at $\lambda = 1.5406$ Å for a scan range of 10 – 50 2θ at 2^{o}/min. All XRD data was normalized. UV/Vis measurements were made with an Eppendorf Biophotometer between the wavelength of 250 nm – 800 nm, with ethanol as the reference solvent, in a standard polystyrene 10 mm cuvette.

Figure 3.5: FTIR (left), XRD (middle), and UV-Vis (right) instruments

3.3.3 Thermal Analysis

A thermal analysis was performed to evaluate the overall ablative performance of the material. The thermal degradation behavior was measured using thermal gravimetric analysis (TGA) with a TA Q500 (Figure 3.6) for a temperature range of 20 ^{o}C to 900 ^{o}C in nitrogen and a ramp rate of 20 ^{o}C/min. A differential scanning calorimeter (DSC, TA Q2000), shown in Figure 3.6, was used to determine the heat flow behavior of the thermoset material as a method of determining the degree of curing that occurred during the electrospinning process and if a glass transition temperature was observed on the second heating curve. The testing schedule used was a heating

ramp from 20 ºC to 300 ºC, a cooling ramp from 300 ºC to 20 ºC, and a second heating ramp from 20 ºC to 300 ºC with a ramp rate of 10 ºC/min for each one. A hermetic pan was used to enclose all samples. The second heating ramp was used for comparison. While the melting behavior of a thermoset using a DSC will typically show a downward curve with little to no peaks, the presence of a melting temperature peak would potentially indicate that the film was not fully cured. The glass transition temperature was observed as well.

Figure 3.6: TGA (left) and DSC (right) instruments

Chapter 4 Results and discussion

The electrodeposition solution components were selected by Dr. Edward Elliot (Nanovox, LLC) in conjunction with OSU to evaluate the ability of the polymer system to be electrodeposition. Several trials were performed to optimize the system and obtain a composite film sample. The final selection of the polymer matrix and fillers were evaluated for their materials properties.

4.1 Initial trials

The focus of the initial trials was the production of a "Taylor cone" and observing the depositions onto the grounded collector. For each electrodeposition trial, a droplet was created before the application of an electric field to test the syringe pump. Once a starting voltage (below 10 kV) was selected, the droplet was observed through the Dino camera and recorded and photographed to observe for changes in the droplet shape and jet pattern as the ES parameters were changed. Once the system stabilized, the solution was left to run with or without the application of UV light to evaluate the equipment set-up and ensured that the polymer was deposited onto the collector. The deposited material was collected on a 1.5" x 1.5" grounded aluminum sheet to evaluate deposition, properties, and how the UV light influenced the deposition/morphology of the sample. The original set-up depicted in Figure 4.1, shows the UV being introduced perpendicular to the path of the jet.

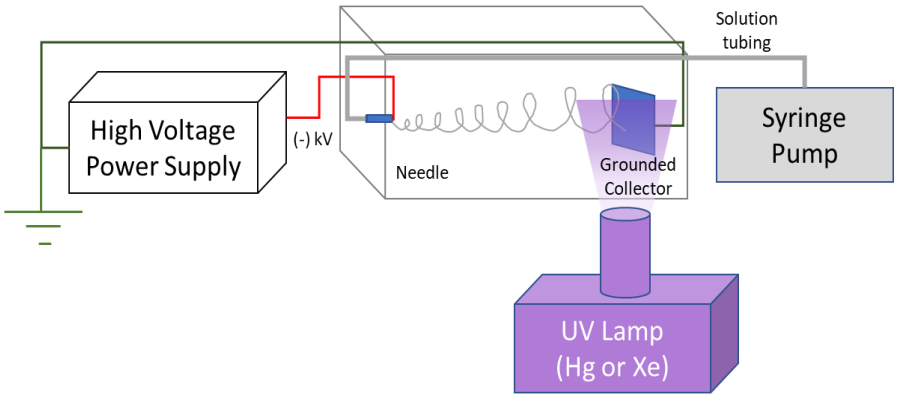

Figure 4.1: Initial electrodeposition set-up (Air only)

4.1.1 A-POSS/AOMA composite

Initial ES experiments conducted utilized AOMA (Figure 4.2) as a second monomer in ethanol with TPO and A-POSS. The AOMA was added to help increase the flexibility of the film and possibly introduce a cyclic functional group into the polymer.[131,132] To determine the optimal monomer ratio for increased flexibility, a series of tensile tests were conducted by Nanovox, LLC (Figure 4.3). A 1:1 ratio of A-POSS/AOMA was decided upon as it exhibited an elastic response as shown in Figure 4.2.

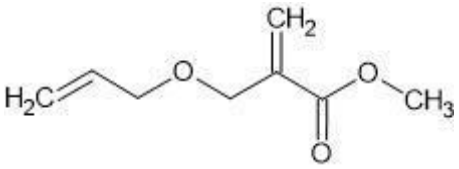

Figure 4.2: Methyl 2-((allyloxy)methyl)acrylate (AOMA™)

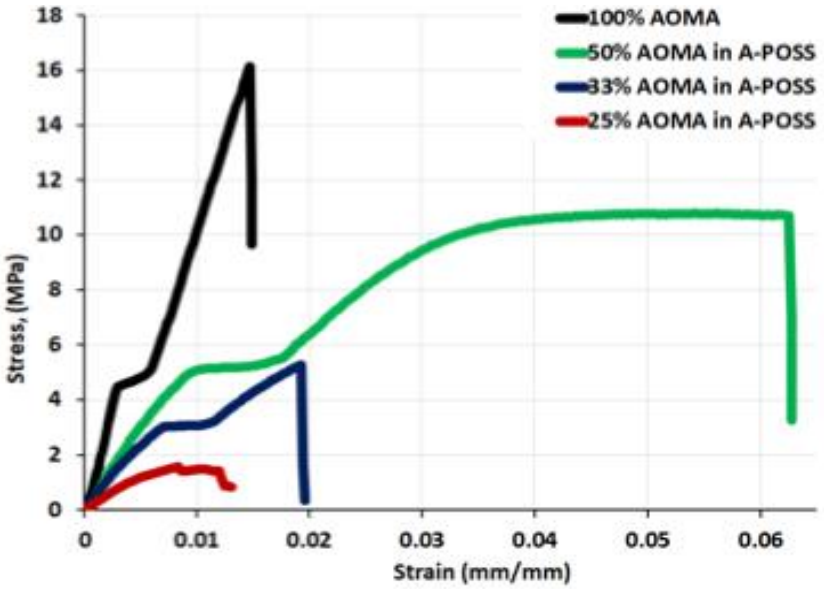

Figure 4.3: Result from an experiment conducted by Nanovox, LCC (Nanovox, 2020)

One of the main focuses of the ES experiments was to produce a Taylor cone using a 1 wt.% 1:1 solution of A-POSS/AOMA and observe how the material was deposited onto the grounded collector. As shown in Figure 4.4, a Taylor was producible with a voltage of approximately 10 kV, and polymer material was deposited onto the collector. UV light was introduced using the Hg lamp and the Xe lamp. Both UV lamps produced uncured material deposited onto the collector even with slower flow

rates to reduce build-up. These results led to the question of whether the polymer required longer curing times or whether it could be cured at all.

Cure studies were conducted to determine the curing behavior of the monomers. These were carried out by just using a droplet of monomer mixture and applying the Hg lamp onto the droplet for different time intervals (10 seconds, 30 seconds, 1 minute, 5 minutes, and 10 minutes) for a maximum of 10 minutes. Similar studies were performed for the monomers in ethanol solution with a 2 wt.% concentration. Early trials with the droplet mixtures produced signs of the pure A-POSS/AOMA, however, the pure AOMA droplets remained in the liquid phase. The solution cures showed the same results with the AOMA monomer as shown in Figure 4.5. A chemical analysis of the polymer product using FTIR (Figure 4.6) and trials conducted with just the AOMA monomer showed that it did not polymerize nor react with the A-POSS monomer.

Figure 4.4: Image of a Taylor cone produced from the A-POSS/AOMA solution

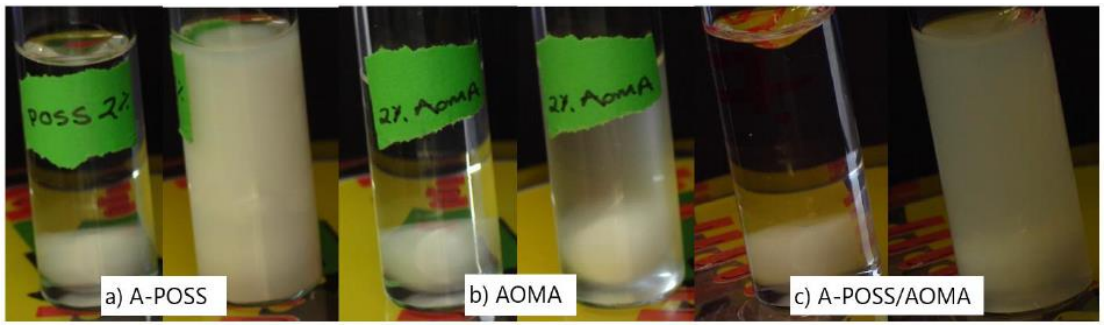

Figure 4.5: Solution cure trial for A-POSS (a), AOMA (b), and A-POSS/AOMA (c) in ethanol

The cured monomer mixture, in Figure 4.6, has an identical spectrum to that of the cured POSS. This measurement was repeated showing a similar trend indicating that the AOMA was not reacting with the A-POSS monomer. These results correlated with what was observed during the ES trials as attempts to produce a cured sample continually showed an uncured coating was deposited.

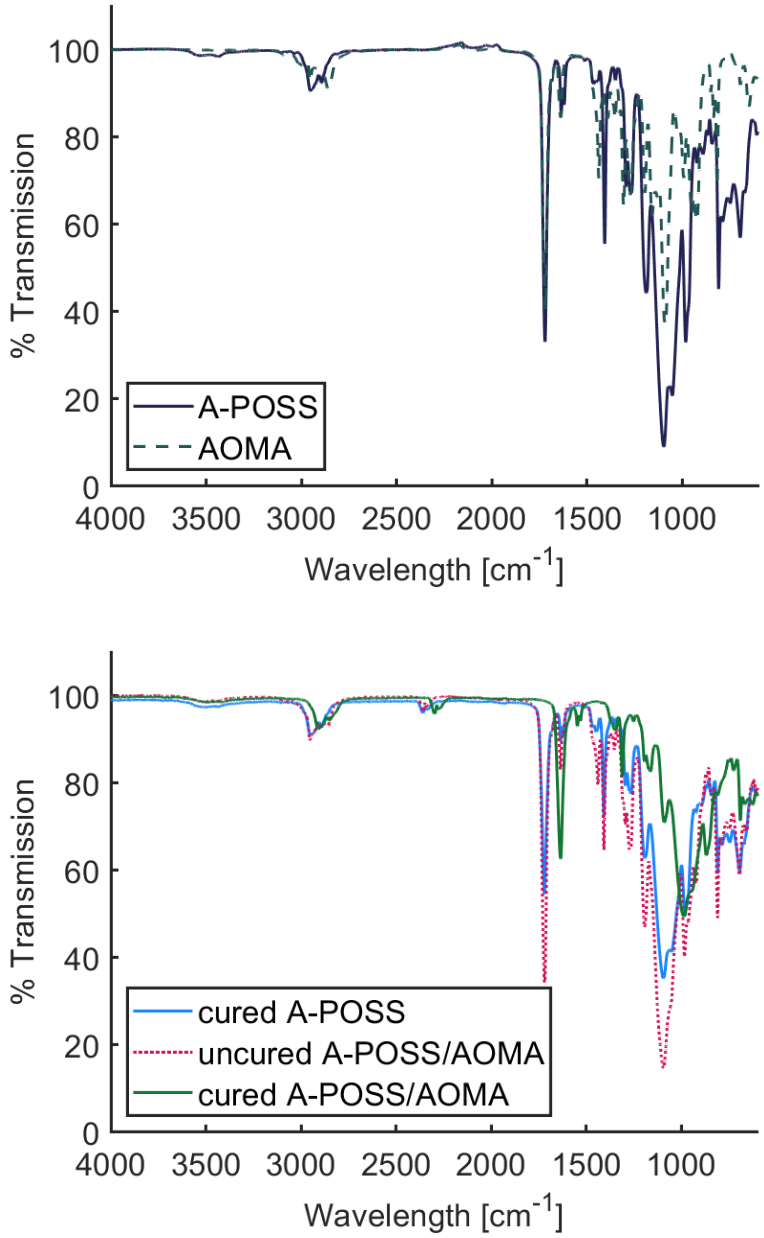

Figure 4.6: FTIR spectra of A-POSS and AOMA

For experiments conducted in the rectangular set-up (in an air environment), the majority were uncured to semi-cured with only one successful cured sample. The semi-cured sample showed curing only at the bottom of the aluminum foil despite the majority of the sample dripping off. The fully cured sample showed a light coating of a sample deposit. A white deposit was possible if the solution cured while wet on the collector, since the solution used was a 1 wt.% A-POSS in ethanol. This result was

observed for photopolymerization trials performed in ethanol solution. (Figure 4.8) To ensure that the material was absorbing efficiently at the recommended wavelength for the photoinitiator (365 nm), a quick UV absorption was run as shown in Figure 4.7, where the maximum absorption for A-POSS with TPO in an ethanol solution was at 380 nm. Due to this, the 365 nm filter was removed from the Hg lamp for later trials.

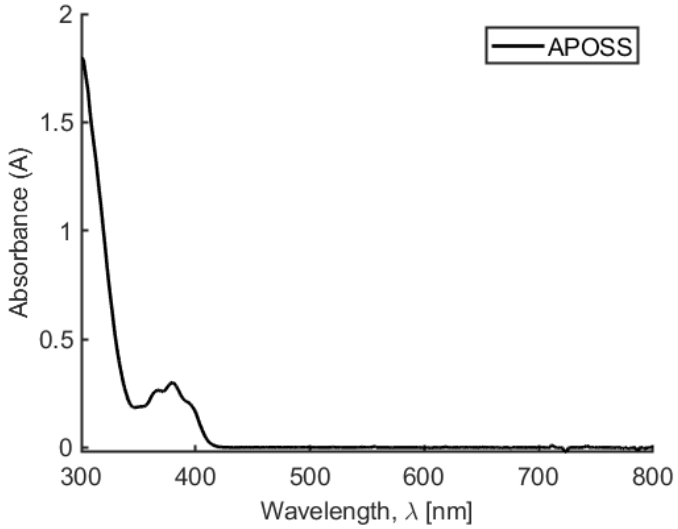

Figure 4.7: UV spectra of A-POSS (1 wt.%) with TPO (3 wt.%/monomer) in ethanol solution

Figure 4.8: Deposition of A-POSS solution onto Al foil (left and middle) with the solution of A-POSS in ethanol post-cure (right).

After the AOMA was proven to not work as intended, subsequent trials were performed using only the A-POSS until another monomer was selected. Similar to the previous trials, curing continued to be an issue due to different reasons. Two UV lamps were used during the trials to compare how effective they were in curing the

material as the light intensity was an important factor to consider. The Hg lamp, which allowed for more control of this parameter showed an overall weaker intensity compared to the Xe lamp, which includes the UV and visible light spectrum. An FTIR analysis, using just a droplet of the solution, showed that there was no difference in the functional group chemistry between the two products (Figure 4.9). From the spectra, the conversion of the acrylate bonds was exhibited with the disappearance of the C=C bonds at ~1650 cm^{-1}. A reduction of the carbonyls at ~1680 cm^{-1}, C-H stretch at ~ 3075 cm^{-1}, and Si-O-Si bonds at ~1100 cm^{-1} was observed.[133,134]

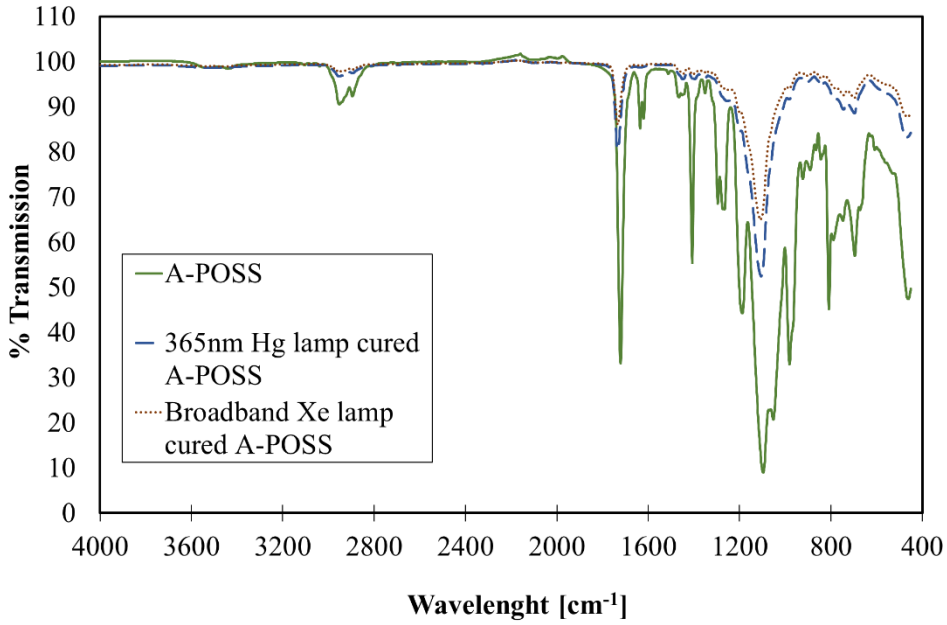

Figure 4.9: FTIR Spectra of A-POSS cured with different UV lamps (Xe and Hg)

As no chemical difference was shown, the trials were carried out to visually judge the degree of curing which occurred on the Al collector. The light was applied as shown in Figure 4.1 but closer to the collector compared to the needle. The result of the trials was a greater degree of curing with the Xe lamp samples compared to the Hg lamp. Part of this difference was due to different lamp intensities, but the spot size also played a role as the Hg lamp has a < 0.25” lens and the Xe lamp has a ~ 1.5” lens. Since the spot size was larger with the Xe lamp, more of the sample was cured on the

Al foil. Both lamp methods still showed a common issue of having the solution flow down to the bottom of the foil. Even at closer distances, this still proved to be an issue showing that the polymer system had a high degree of oxygen sensitivity, which is common with acrylate monomers.

The thermal gravimetric analysis of the cured polymer was performed using a pure sample of A-POSS. (Figure 4.10). On the spectra of the pure A-POSS shown in Figure 4.10, two potential peaks are exhibited in the derivative weight analysis where the curve of weight loss vs. temperature indicates the loss of the organic molecules in A-POSS, leaving only the glassy material, SiO_2, behind. This was expected as the Si-O cage structure will react under thermal degradation to form SiO_2 molecules.

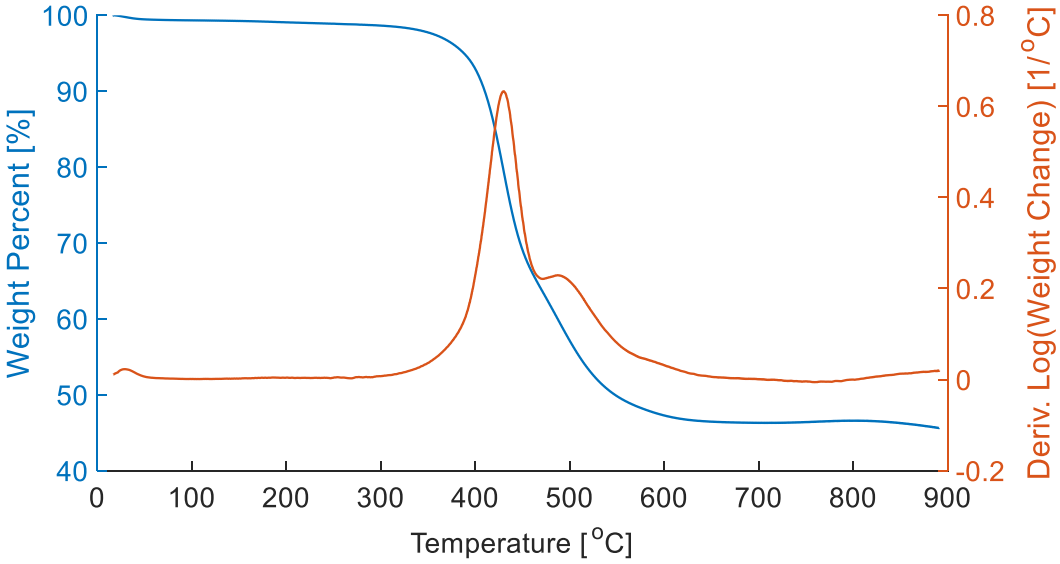

Figure 4.10: TGA of pure A-POSS

4.1.2 A-POSS with TEDGA, DEDGA, DUDMA, or BPAEA monomers

A series of trials were conducted using four monomers suggested: DEDGA, DUDMA, TEDGA, and BPAEA (Figure 4.11) to determine which monomer with A-POSS had the fastest chemical reaction and displayed the best thermal stability. Drop cure studies showed that each monomer was able to cure on its own and react with A-POSS. To compare the cure speed, a sample size of 5 mL was used with a 1% concentration (w/v) of A-POSS and the second monomer with a 1:1 ratio. Due to the

presence of inhibitors in the monomer solutions, each monomer was run through an alumina column for removal to improve curing. The trials were conducted using a time scale of ten seconds, thirty seconds, one minute, and five minutes. Each trial showed signs of curing after one minute, however, the TEDGA and DEDGA were completely cured in solution before 5 mins, while the DUDMA and BPAEA did not stop curing until 10 minutes were reached. A UV analysis was run to judge the absorbance of each solution compared to the A-POSS one. The TEDGA and BPAEA showed similar absorbance values to the A-POSS for a solution at 1 wt.% concentration with TPO present as shown in Figure 4.12. The presence of the TPO is shown in the broad peak between 350 – 400 nm.

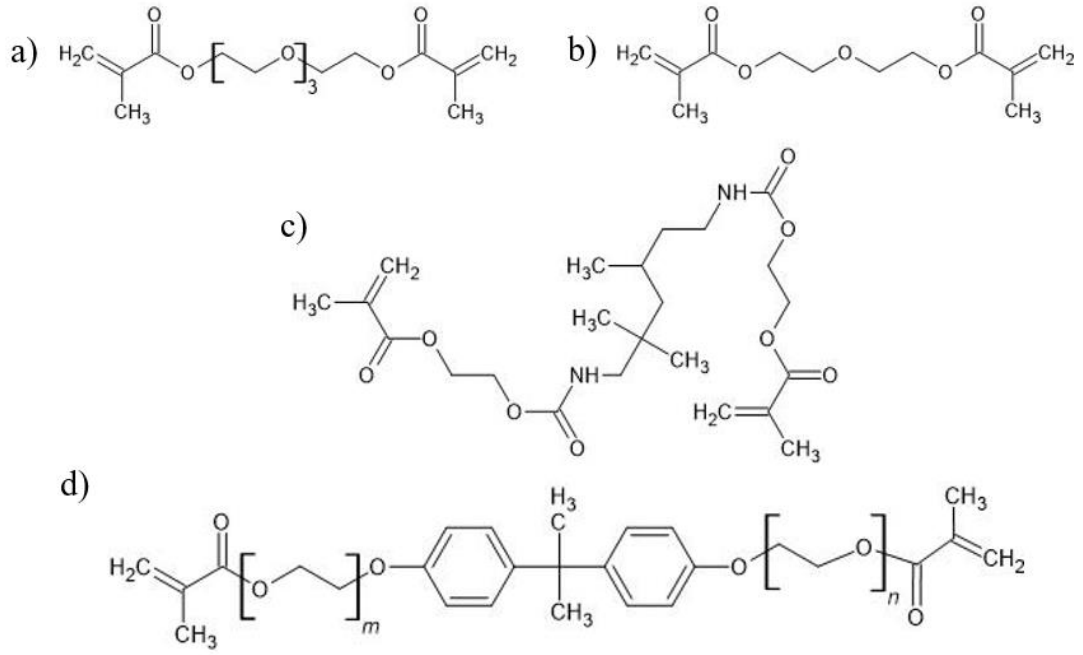

Figure 4.11: Chemical structure of a) TEDGA, b) DEDGA, c) BPAEA, and d) DUDMA

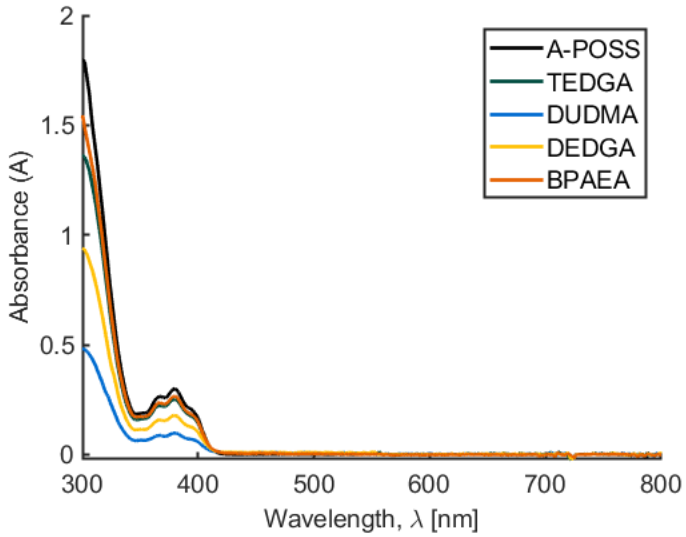

Figure 4.12: UV spectra of A-POSS, TEDGA, DUDMA, DEDGA, and BPAEA 1 wt.% solutions in ethanol.

The FTIR spectra for the four monomers are shown in Figure 4.13. This provides a confirmation of the functional groups present as the DUDMA showed a N-H peak at about 3400 cm^{-1}, which is due to the urethane functional group. The presence of the C=C and C=O bonds, about 1650 cm^{-1} and 1750 cm^{-1}, indicate acrylate functional groups. Aromatic undertones between 2500 – 2000 cm^{-1} are observed for BPAEA which are indicative of the resonance from benzene rings.

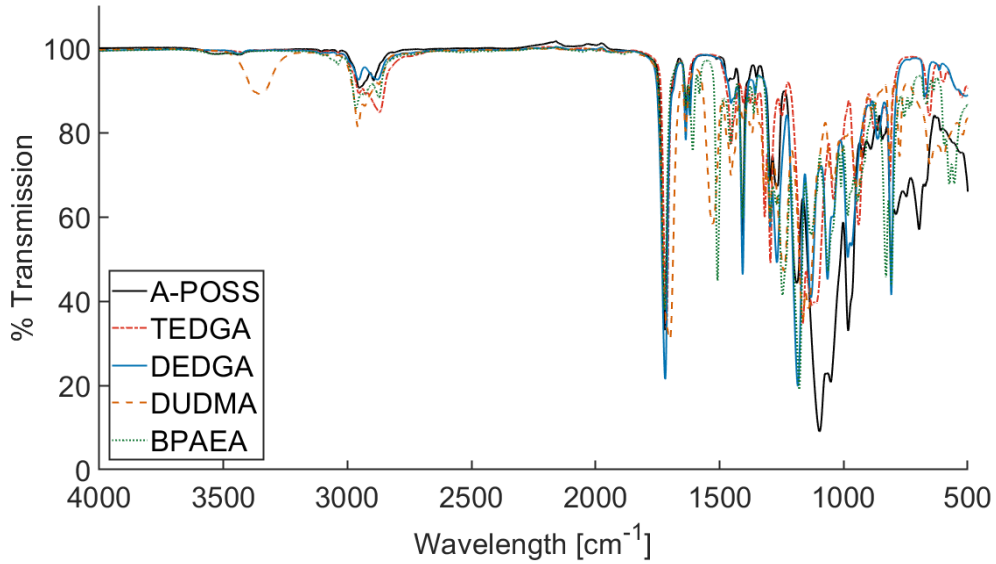

Figure 4.13: FTIR spectra for the four monomers (DUDMA, DEDGA, TEDGA, and BPAEA) compared to A-POSS.

The FTIR spectrums of TEDGA, DEDGA, DUDMA, and BPAEA with A-POSS show the degree to which the reaction occurred using similar cure times for three drops of a pure monomer mixture with TPO (Figure 4.14). The mixtures were prepared by sonicating for one hour and then mixing overnight with a magnetic stir bar. A reduction of acrylate and carbonyls are observed in the spectra for each compound at about ~1650 cm^{-1} and 1670 cm^{-1}, respectively. The BPAEA exhibits a lower degree of conversion compared to the other three which may be due to differences in viscosity or chemical structure as BPAEA has benzene rings which may further inhibit the diffusion of the free radicals.

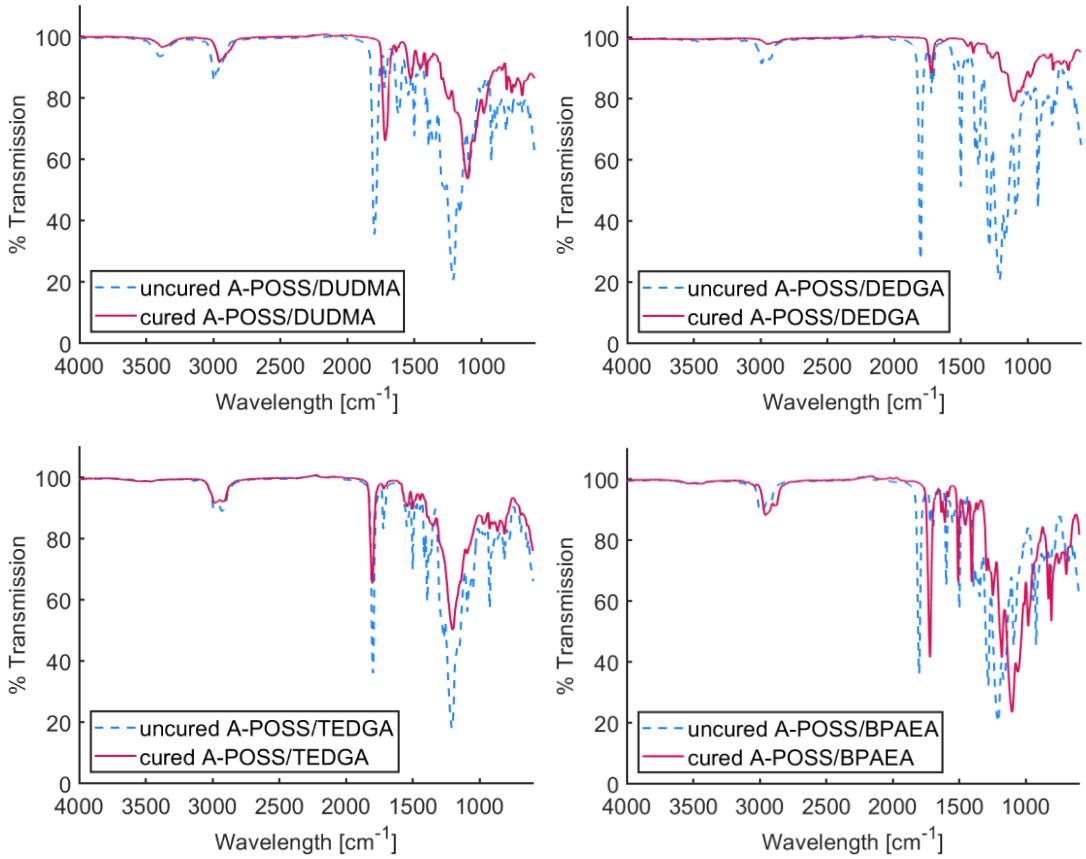

Figure 4.14: FTIR spectra of the a) A-POSS/DUDMA, b) A-POSS/DEDGA (top-right), c) A-POSS/TEDGA (bottom-left), and d) A-POSS/BPAEA (bottom right)

DEDGA and TEDGA were the better options to use based on the results from the FTIR and TGA. DEDGA shows higher thermal stability compared to the TEDGA when using just the TGA data (Figure 4.15). The two initial peaks shown for

DUDMA and BPAEA are due to residual uncured material present in the sample. TEDGA had the earliest onset of degradation starting below 350 ºC. BPAEA showed the best char residual results of the four monomers, which could be attributed to the phenyl groups present. DEDGA had a faster rate of curing, which is necessary for in-situ photopolymerization electrospinning, and was selected to investigate further for ES trials.

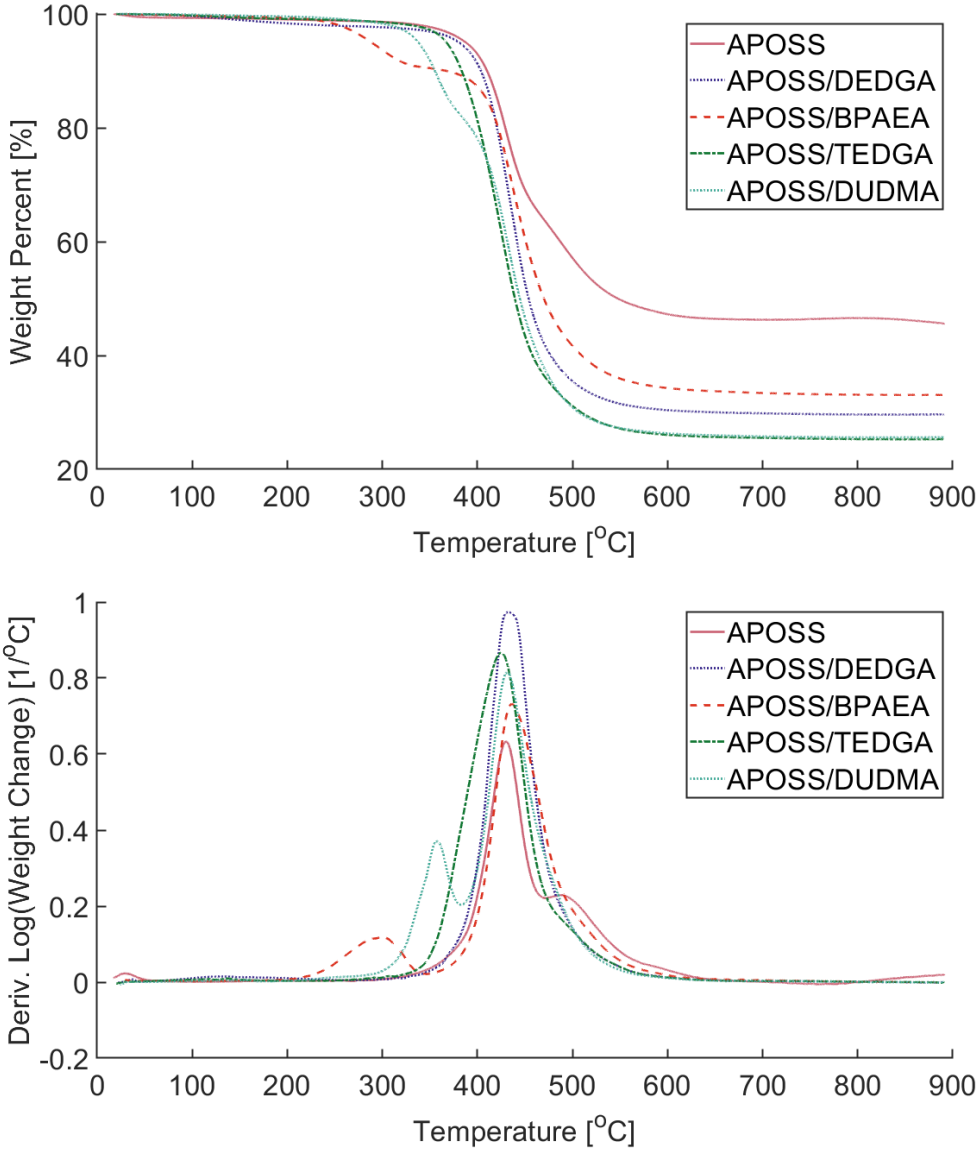

Figure 4.15: TGA spectra of A-POSS, A-POSS/DEDGA, A-POSS/BPAEA, A-POSS/TEDGA, and A-POSS/BPAEA

Table 4.1: Dyes used within well plate reader

Dyes in row B	Result	Dyes in row G	Results
1) Thymol blue	Cured	1) Methylene red sodium salt	Cured, separated in solution
4) Coumarin 500 (acid yellow 75)	Cured, separated in solution	4) Rhodamine B	Cured
6) Iodine	No reaction, uncured	6) Methylene blue sodium salt	Cured, dye settled at the bottom
8) Quinaldine red	Cured, separated in solution	8) Acid Yellow 34	Cured, separated in solution
10) Azobenzene	Cured	10) Fluorescein	Cured, separated in solution
12) N/A	N/A	12) O-dianiside dihydrochloride	Cured, colorless (eliminate)

One of the main issues with evaluating the degree of curing was the transparency of the deposit materials, as it is difficult to visually judge deposition or curing for a clear material on a metallic surface. While the deposited polymer mixture did have some yellow tint due to the TPO, the overall clarity was difficult to compare or collect photographic data. The dyes were utilized to make the comparison easier. Several dyes were utilized to determine which will allow for curing and which would interfere with the curing process. The dyes evaluated are shown in Table 4.1.

A clear well plate was used to compare the dyes with only a small amount of dye added to each well with a tweezer (Figure 4.16). In each well, four drops of pure A-POSS/TEDGA solution were added and mixed with a toothpick. Once the dyes were well-mixed, the Hg lamp was used to apply the UV light within a black foamboard cutout for 30 minutes. The most successful dyes were azobenzene, rhodamine B, and thymol blue as shown in Figure 4.16 of the well plate and the result in Table 4. Some of the dye did show some degree of curing however, any evidence of uncured material eliminated that dye as an option. The thymol blue was discarded since higher contrasting colors were preferred. Azobenzene and rhodamine B were selected for the ES trials with methylene blue added due to reported success in literature studies for acrylate monomers.

Electrodeposition trials were conducted with three dyes to confirm that curing was observed and to obtain a visual comparison of the deposition and curing. The dyes

Figure 4.16: Image of dyes tested in well-plate. The dyes are listed in Table 4 to the corresponding location on the well plate.

were added to a 1 wt.% solution of A-POSS/EB and mixed overnight. The first dye used for ES was azobenzene. Despite having a fully cured well sample, the azobenzene solution showed very little curing. The material mostly ran down and dripped off the aluminum foil sample collector (Figure 4.17a). The system was flushed with ethanol after each trial to reduce contamination between solutions. The rhodamine B solution was used next and showed visual improvement. The deposition shown in Figure 4.17b, proves that the solution is hitting the sample periodically by the spread of solution shown on the surface of the collector. The collected sample did show some curing; however, it also had a high degree of material loss, which gathered at the bottom and dripped off. Both attempts with the Hg and Xe lamp produced similar results. The methyl blue solution showed similar results at first to the rhodamine B (Figure 4.17c) however, with a reduction in the flowrate, there was a marked decrease in the run-off with more curing in the middle of the samples (Figure 4.17d). The utilization of the methylene blue allowed us to gain a visual representation of how the material was depositing and a comparison of the difference in flow rates.

Electrodeposition trials were performed using the set-up shown in Figure 4.1 using the TEGDA monomer first. Trials were conducted with or without UV light provided

from a Xe or Hg source lamp. Curing in-flight was attempted during these trials with the lamp placed perpendicular to the flight path using both lamp sources to judge

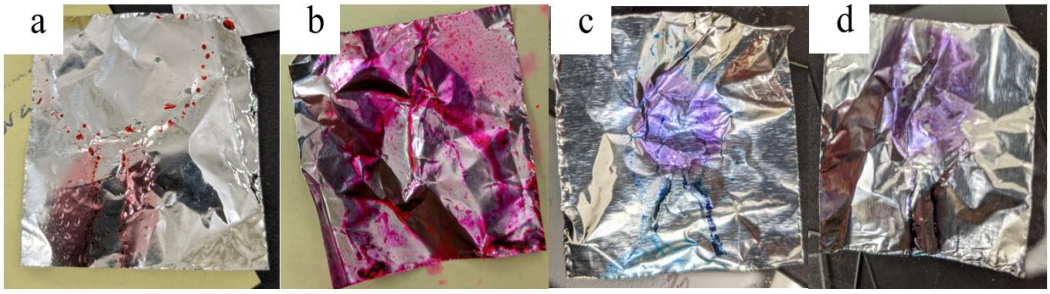

Figure 4.17: Deposition appearance of the dyed A-POSS solution after ES. The dyes used are (a) azobenzene, (b) rhodamine B, and (c + d) methylene blue with (d) showing the result with a lower flow rate.

effectiveness. The results of these trials show the solution depositing on the Al sheet is still in a liquid state with little curing. The UV lamp source was redirected to shine mainly onto the collector to improve the intensity applied. The majority of the cured polymer was collected towards the bottom of the Al film indicating that the solution dripped down the collector before curing. More polymer is cured in the center: however, this still shows that curing is an issue during flight. The oxygen environment proved to be too much of an inhibitor to conduct the free radical polymerization reaction based on evaluating the distance to the collector parameter.

The set-up was then changed to a vacuum chamber apparatus to provide a more inert environment for in-flight polymerization. (Figure 4.18) The UV lamp was positioned onto the collected with a vacuum outlet and nitrogen inlet to perform an initial purge of oxygen followed by a low stream of nitrogen. A light vacuum was still applied during electrospinning to maintain an environment close to atmospheric. Successful polymerization trials were observed to improve the curability of the system. Despite this improvement in curing, no film was formed, and the cured sections had a viscous layer on top. Before more trials were conducted, a new secondary monomer was selected, EB, which could potentially improve the flexibility of the polymer composite.

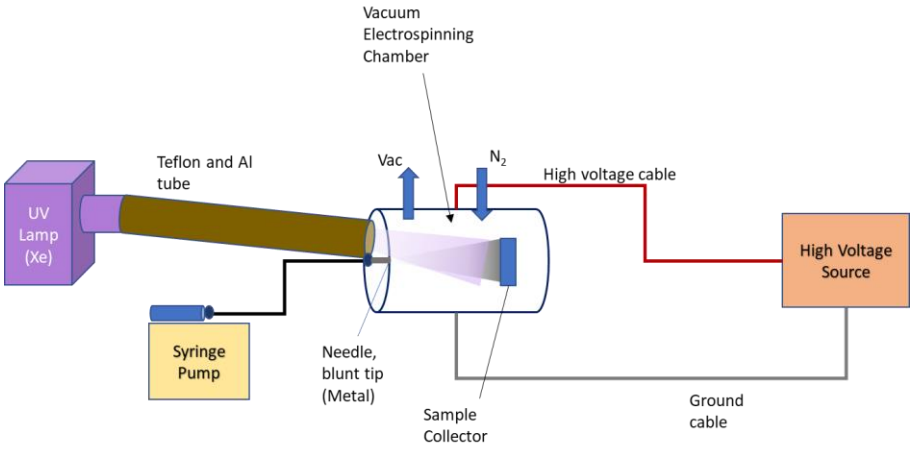

Figure 4.18: ES set-up with the UV light (Xe) aimed at the collector parallel to the flight path.

4.2 A-POSS/Ebecryl composite trials

Using EB as the secondary monomer showed early promise of increasing flexibility of the A-POSS composites as a successful trial produced a film that was observed to be easier to handle compared to previously cured materials, which were more rigid and broke easier. (Figure 4.19) SEM images of the deposited materials and film showed a lack of distinct morphology, which suggest that the solvent was not drying fast enough to allow for the deposited material to maintain a shape. The FTIR analysis (Figure 4.20) of the composite showed that a vinyl polymerization reaction occurred due to a reduction in the C=C bonds at ~1600 cm^{-1} with a reduction of the N-H bonds from the EB monomer at ~3400 cm^{-1}. The spectra of the A-POSS/EB do not show a complete reduction of C=C bonds, inferring that some of the material was not fully cured. The final structure of the polymer was undetermined as attempts to analyze the structure of the polymer using traditional methods were inhibited by the insolubility of the cured polymer in stronger solvents (dichloromethane and toluene) to perform nuclear magnetic resonance or mass spectrometry.

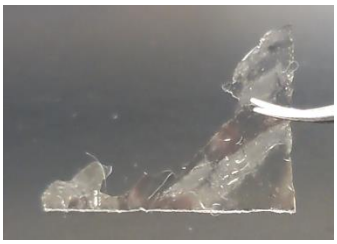

Figure 4.19: ES film produced from A-POSS/EB in EtOH

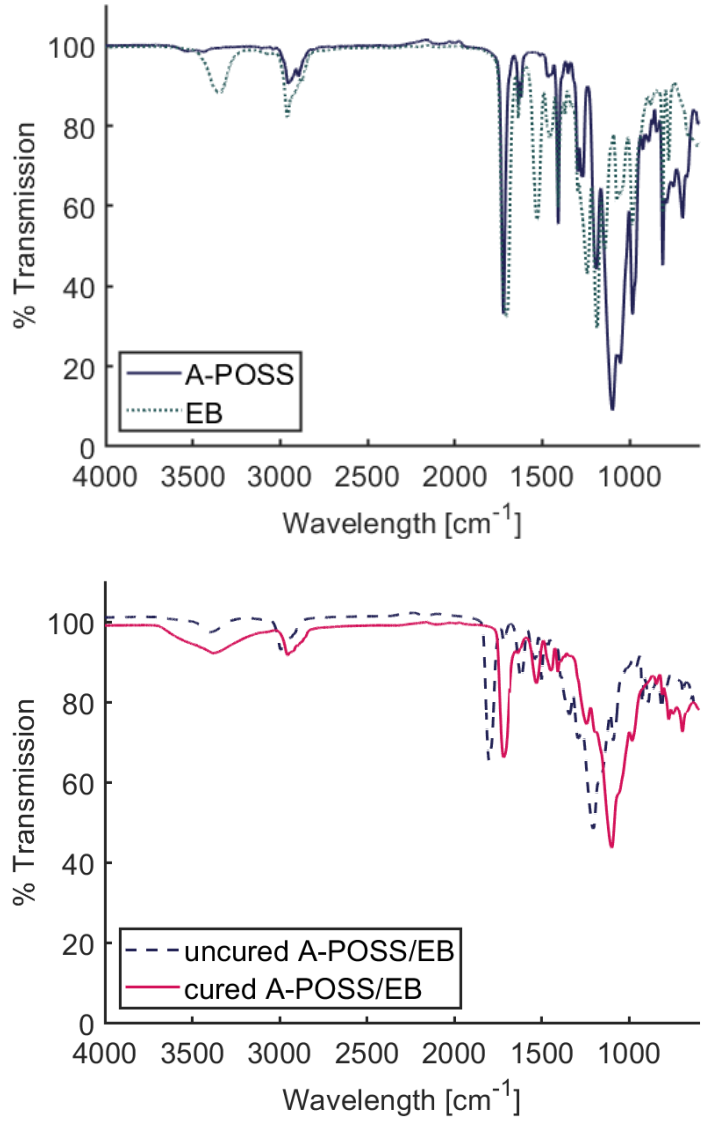

Figure 4.20: FTIR of the uncured A-POSS and EB, cured A-POSS, A-POSS/EB film

While a film was produced with the A-POSS/EB solution, the results of the trials were largely inconsistent and rarely produce a film. Different parameters were investigated with the distance increased and flow rate decreased to provide a longer time to cure. Attempts to reproduce the results shown in Figure 4.21, using the same parameters were unsuccessful with most showing a low degree of curing and drippage down the collector. The majority of the literature published on electrospinning polymers used halogenated or non-polar/polar solvent mixtures with higher volatility.

Solvent trials were performed to evaluate whether the solvent choice was the cause of the issue.

Figure 4.21: Deposition appearance of ES samples during the solvent trials. Images (a) show the typical depositions observed for EtOH samples. Image (b) shows the collector appearance on a more even coating that has been collected. Images (c + d) show the appearance of the completed cured film which often splits after a drying phase.

A new solvent system was investigated by referencing the literature and choosing a solvent that could be a reference. As the desired result was to evaluate this system as a potential TPS manufacturing method, ethanol was the initial solvent picked for ES. While chloroform was used as a reference for solvent properties, preference went to choosing a non-halogenated solvent with less toxicity. The vapor pressure and surface tension were used to compare the solvents as shown in Table 4.2.

Table 4.2: Surface tension and vapor pressure of different solvents for electrospinning

Solvent	Surface Tension [mN/m] @20 ºC	Vapor Pressure [hPa] @20 ºC
Ethanol	22.10	59
Chloroform **(Reference)**	27.50	210
Isopropyl Alcohol	23.00	44
Acetone	25.20	240
Tetrahydrofuran	26.40	200

Since solvent evaporation plays an important factor in electrospinning, solvents with a higher vapor pressure were preferred for increased volatility. Low surface tension

was ideal to maintain a low applied voltage. Acetone and tetrahydrofuran (THF) were chosen to test for improved polymer deposition and curing. Different mixtures were tested with a 1:1 or 2:1 ratio of ethanol, acetone, or THF with pure solvents included as controls (Table 4.3) with the results shown in Table 4.4.

Table 4.3: Solvent trials for a 1:1 or 2:1 solvent ratio

1:1 solution	**Acetone**	**THF**
Ethanol	X	X
Acetone	X	X
THF	X	O
2:1 solution	**Acetone (1)**	**THF (1)**
Ethanol (2)	X	X

Table 4.4: Solvent trials results

1:1 solution	**Acetone**	**THF**
Ethanol	Uncured deposition. Clear with only cured part at the bottom of the collector. Mostly droplets.	Semi-cured but slight a mostly uncured deposit coating with agglomeration at the bottom of the film.
Acetone	No deposition. Crackling heard when a voltage applied.	Uncured to semi-cured coating.
THF	X	Successfully produced a film with an opaque appearance. No uncured or viscous layer observed.
2:1 solution	**Acetone (1)**	**THF (1)**
Ethanol (2)	X (Unattempted)	Uncured to semi-cured coatings.

Acetone was first eliminated as it proved to be a safety concern during electrospinning as crackling was heard even at low voltages. The mixture of ethanol and acetone did not show any improvement in curing as well as sample collected looked like Figure 4.21a. Before the pure THF solution was used, the ethanol/THF

solutions were ran first in the hope of achieving a successful trial as THF is still a fairly toxic solvent. From the ethanol/THF trails, a semi-cured coating was seen as shown in Figure 4.21b, where there is little drippage or agglomerate seen. THF was tested next with an improvement in the deposit. The collected sample still looked like Figure 4.21b but showed less of the viscous uncured layer.

Two attempts were performed using a preheated collected removed from the oven right before ES to see if the heat would help with solvent evaporation. As shown in Figure 4.21(c + d), a more noticeable film was achieved that was removable from the Al foil collector without any grease layer or uncured residual. Based on this trial, pure THF was chosen as a solvent for future ES. Further trials with THF proved to continuously form polymer films (Figure 4.22) with a vacuum applied and nitrogen fed into the system. Other solvent mixtures of ethanol and THF were attempted (2:1 or 3:1 THF/ethanol) with lesser degrees of success and no film production. Attempts to ES with just air and vacuum showed a decrease in curing while using just nitrogen made ES for a long period unstable due to pressure build-up.

Figure 4.22: ES film from A-POSS: EB in THF solvent. Left is the deposited film onto the Al foil collector with right showing the film's appearance.

SEM images were taken of the initial films in order to observe the morphology of the films. An image of APOSS/EB films in THF, in Figure 4.23, is shown for the preheated samples using similar parameters: distance = 20.5 cm, flow rate = 0.3 mL/hr, and applied voltage = 9 kV and 11 kV, respectively, in a nitrogen environment with a vacuum applied using a Xe lamp for photopolymerization. The sample in the top image showed a more beaded deposit with clusters of beads formed throughout the surface. The sample on the bottom image showed random areas in which fibers

were deposited and coated with A-POSS/EB matrix. This sample showed that it was possible to obtain nanofibers using the A-POSS/EB solution with a THF solvent.

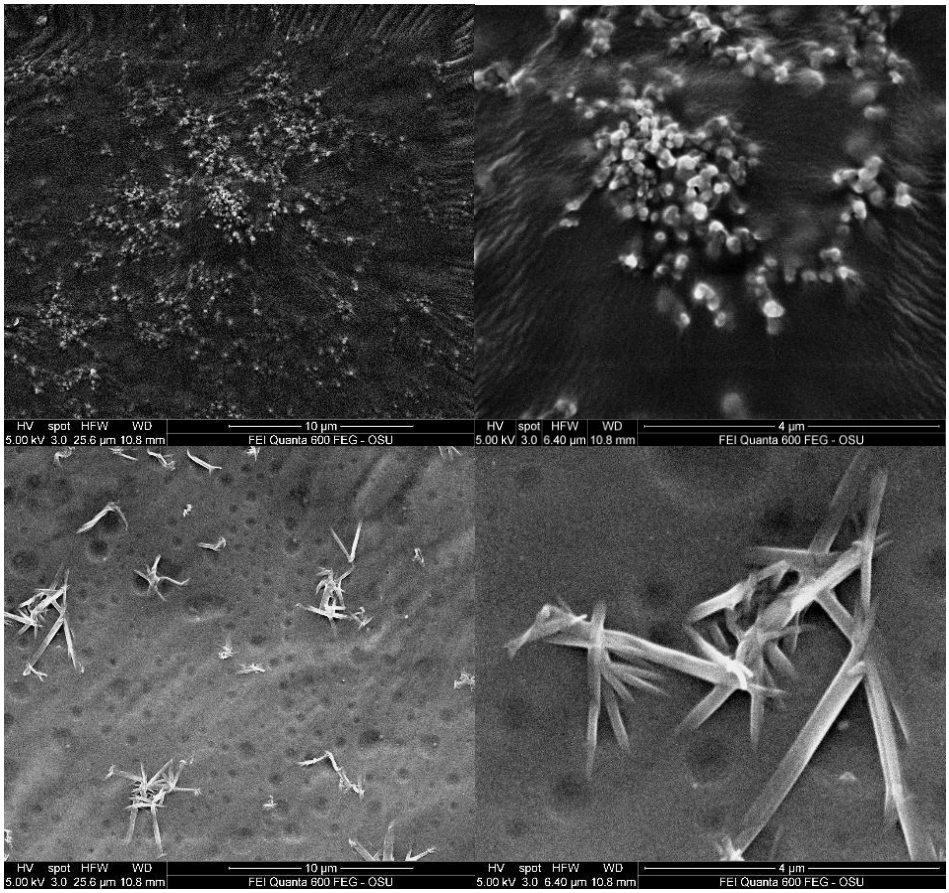

Figure 4.23: SEM images of A-POSS/EB in THF preheated samples. The same parameters were used for both with a duration of 30 mins for ES. The top row is the first sample taken while the bottom is the second. Magnifications are 200x (left) and 4,000x (right).

The use of THF as a solvent resulted in further changes to the setup to accommodate for any incompatibility. One major change was to switch the positioning of the Xe lamp to be perpendicular to the collector (Figure 4.25). The visual results of this change in the

Figure 4.24: Film appearance after changing UV lamp position.
(A-POSS/EB samples)

film's appearance are shown in Figure 4.24. While consistent curing was obtained, the shape of the film changed to match the pattern of the UV lamp on the foil. Arcing of the film was also observed. The further the collector was from the needle, the more the film sample arced upward towards the top of the collector. This was later confirmed to be a result of the distance from the needle when electrospinning PLA in DCM solution.

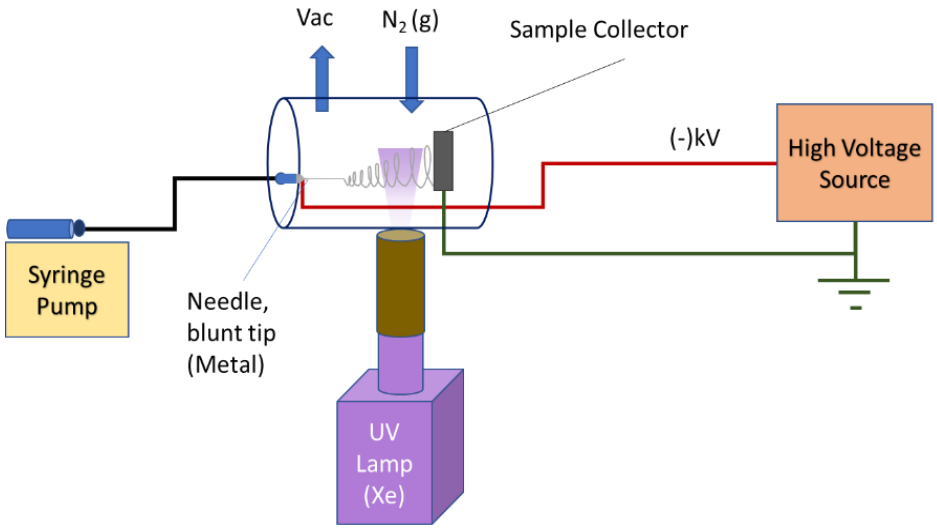

Figure 4.25: Electrodeposition set-up within a vacuum chamber

Different morphologies should have been observed depending on the distance from the needle to the collector and applied voltage, as the distance affects the fiber/deposition size of the materials. The images viewed under optical microscopy did not show any fiber formation, but rather a bumpy surface, which suggests that the droplets or beads were deposited but were not fully cured to be distinct. The majority of the film samples exhibited macro features with bumpy surfaces. Only a few with smooth surfaces had streaks across due to the Al foil as shown in Figure 4.26. There were no major differences observed for films with similar macro-features using SEM. The presence of a few outliers demonstrates the inconsistency of the ES process when multiple factors influence the morphology of the sample. Figure 4.27 - Figure 4.29 shows the different film morphologies of the A-POSS/EB film in THF.

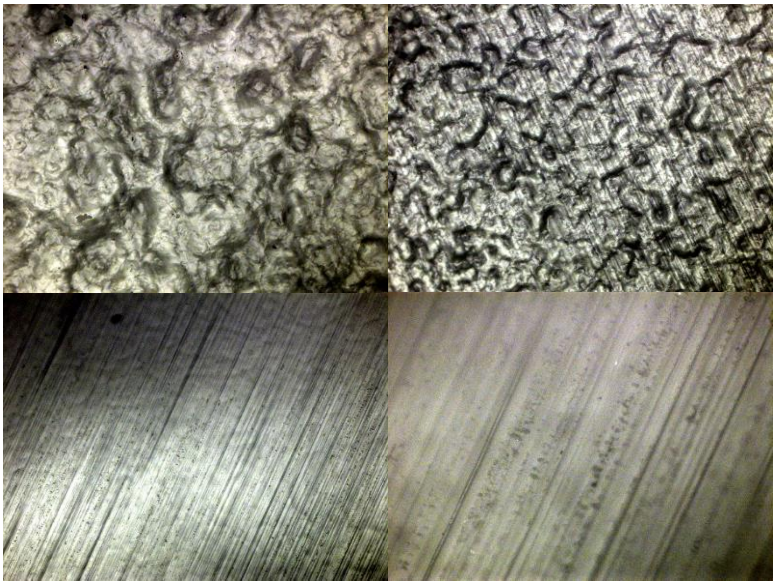

Figure 4.26: Optical microscope images taken of A-POSS/EB in THF samples. (Left - 5x; right – 20x) The image shows the different macro features obtained using the same solution was similar parameters.

One of the issues observed during this project, which was previously mentioned, was the inconsistency of the ES film when it came to obtaining fiber deposition. The creation of a film sample was consistent with the parameters and system used. Odd cases, shown in Figure 4.29, where fibers were deposited onto the collector all embedded within the cured A-POSS/EB matrix suggest that it was possible to produce fibers. Replications of the experiments, which produced those samples, saw constant failure despite using the same parameters within our control (neglecting humidity and temperature effects).

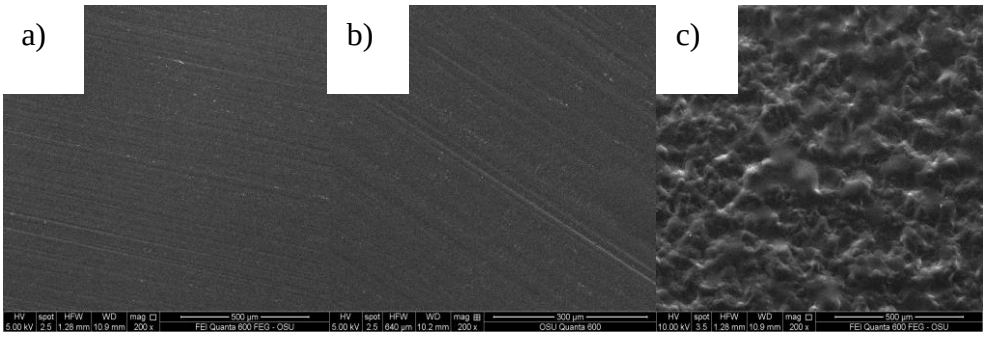

Figure 4.27: SEM micrographs of different morphology of A-POSS/EB in THF film for a smooth surface. Images (a + b) show the lack of distinct surface features with only the pattern shown due to the Al foil. Image magnification 200x.

From the images shown, short, discontinuous fibers were produced. The overall aspect ratio of the fibers was not measured as the actual dimension was uncertain based on the appearance in the film. The desired morphology for the target application of this project was Figure 4.28 sample (a/b). The porous features of the film were thought to improve the thermal degradation, which would allow for the pyrolysis gas to travel through the sample quicker and produce the gas layer quicker.

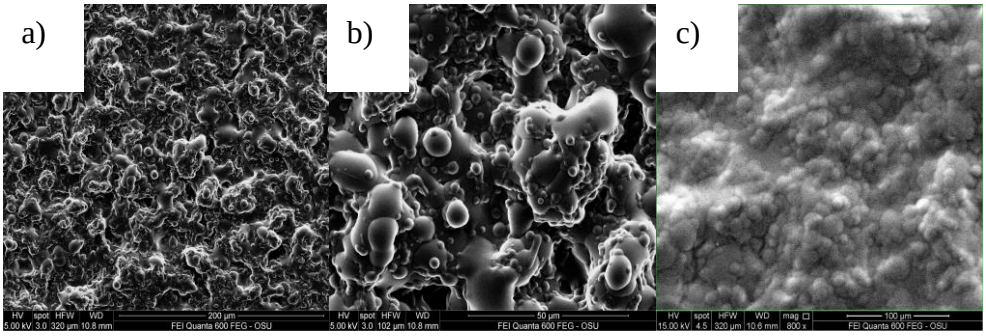

Figure 4.28: SEM micrographs of different morphology of A-POSS/EB in THF film for a bumpy surface. Images (a) + (b) are the same sample with an increase in magnification for (b). Image magnification is at 800x, 2,500x, and 800x, respectively.

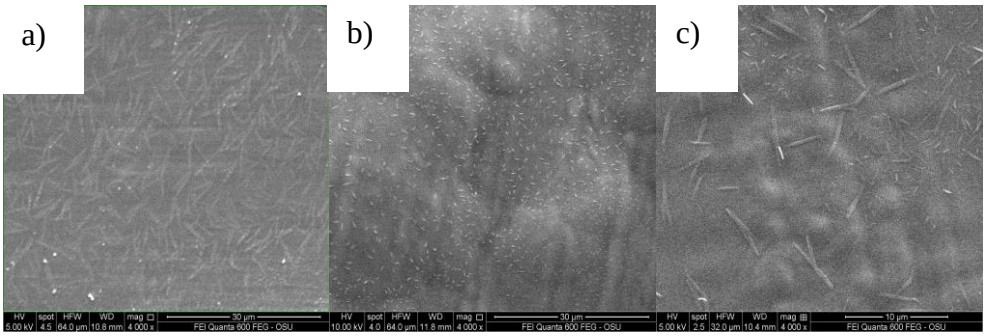

Figure 4.29: SEM micrographs of different morphology of A-POSS/EB in THF film for a smooth (a + c) or bumpy (b) surface with evidence of fiber formation**.** Image magnification at 4,000x.

The thermal analysis of the A-POSS/EB is shown in Figure 4.30. The initial breakdown in the cured polymer A-POSS/EB could be attributed to the chemical breakdown of a functional group from the EB before the main backbone of the polymer is broken within the structure. The TGA data taken of the EB (Figure 4.39) shows two peaks. The first one is noted on the A-POSS/EB plot. Multiple measurements of the A-POSS/EB show the same two regions will appear with a

slower run at 5 °C/min, leading to a possible 3rd peak. The broad peaks shown in the XRD data (Figure 4.30) are indicative of an amorphous material. The single peak represents the POSS structure indicating the Si-O-Si linkages in the structure. There was no significant difference between the A-POSS and A-POSS/EB other than a slight shift in peak position and height.

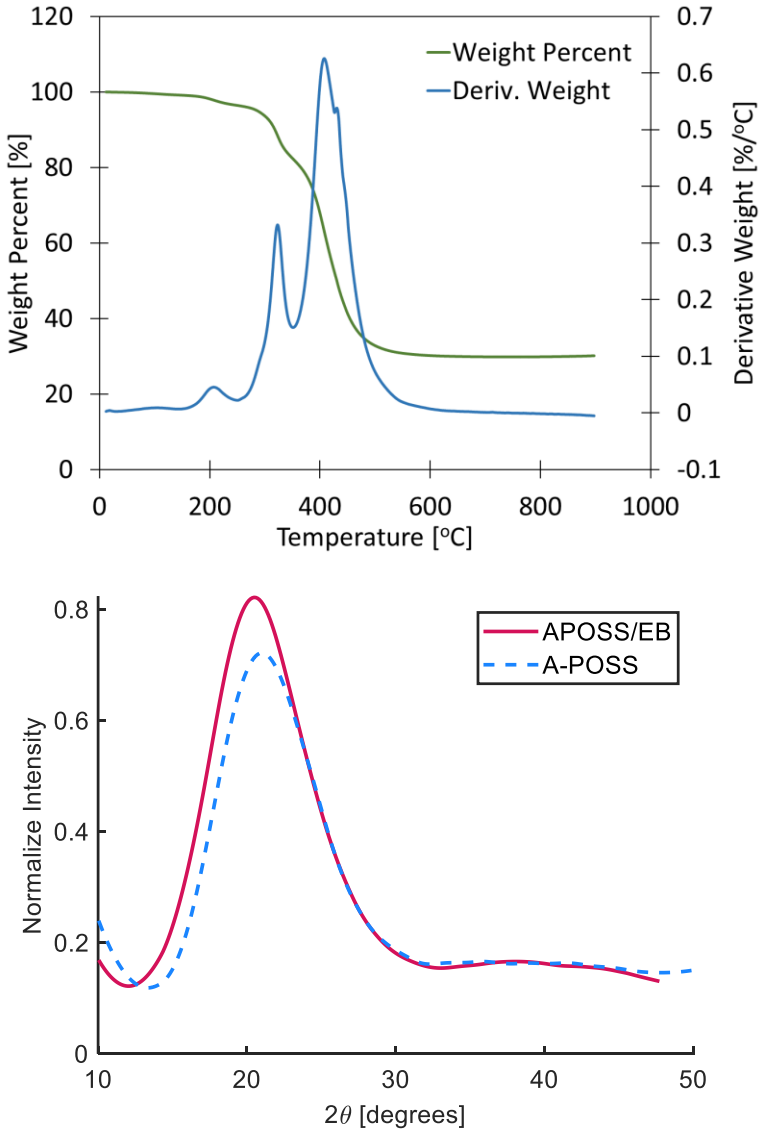

Figure 4.30: TGA of pure A-POSS/EB cured at 5 °C/min ramp rate (left) and XRD of A-POSS and APOSS/EB (right)

A comparative study was done between the pure, solution cured, cast, and ES samples to evaluate the effect that the curing method has on thermal stability (Figure 4.31). There was no significant difference between the methods. The difference in the

residual amount can be attributed to the quantity of Si content within each sample. A decrease in Si content leads to a lower formation of the SiO_2 glassy residual, thereby decreasing the residual amount.

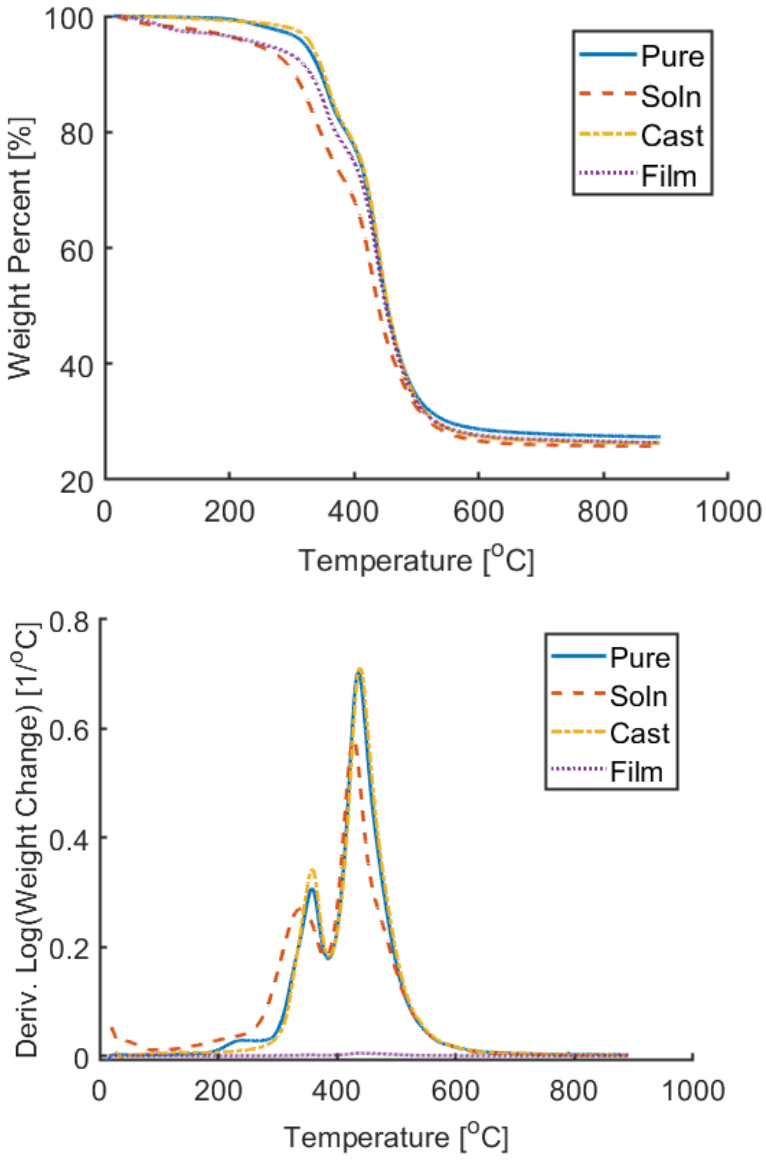

Figure 4.31: TGA and DTG of the cured A-POSS/EB from a pure mixture, solution in ethanol, cast, and electrodeposited film.

4.2.1 Effects of sparging on the ES film

The effects of sparging the solution were investigated for electrospinning to see if the removal of the dissolved oxygen would improve the curability of the A-POSS/EB and

if there was a difference in the appearance of the cured polymer using ethanol or THF. The A-POSS/EB solution was sparged with nitrogen gas after it was completely mixed to reduce the introduction of oxygen through transferring for 30 minutes. The solution was quickly pulled into the glass syringe and attached to the ES set-up once all the other pre-steps were completed to reduce the amount of time between sparging to ES.

An initial trial using sparged ethanol showed that the solution curing improved by a significant amount as shown in Figure 4.32. Curing was observed around the needle for the sparged solution. A hissing sound was heard during ES from the syringe pump as it pumped the solution, indicating that the gas pressure within the solution was in

Figure 4.32: Effect of sparging the ES solution as depicted from the needle perspective. Top row – Image of the needle during electrospinning for a non-sparged (left) and sparged (right). Bottom row – two of the samples collected for the non-sparged (left) and sparged (right) ethanol solution

the process of equilibrating. This was proven to be correct as after approximately two and a half hours had passed after sparging, the hissing noise disappeared. Curing around the needle no longer occurred and the deposited material showed little evidence of fully curing. It was determined from this experiment that sparging the solution substantially improved the film curing. This method, however, would not be feasible without continuously sparging the solution before ES as a maximum time of

~ two and a half hours would require more work to produce a layered composite. A similar trial was conducted with the THF solution with no noticeable difference between the sparged and non-sparged samples using the naked eye.

Since the selection of a solvent is important, the possible use of ethanol for future development is further explored when comparing the cured product produced. In Figure 4.33, the difference in appearance is shown with the more transparent solution being THF and the white, opaque one being ethanol. As both monomers are stated to be ideal for transparency, the possible difference in appearance was hypothesized to be due to a difference in polymer structure or dissolved oxygen. As the chemical structure of the polymer was explored, the determination as to whether dissolved oxygen was the cause was addressed by sparging the A-POSS: EB solution with nitrogen gas after it was completely mixed to reduce the introduction of oxygen through transferring.

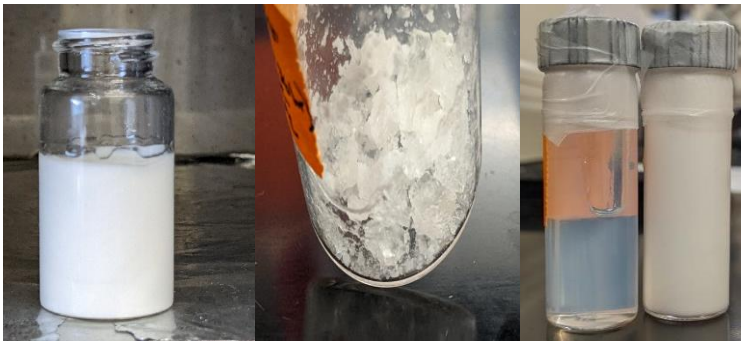

Figure 4.33: Polymer formed while curing in a solution of EtOH (right) and THF (middle) without sparging and after sparging (left) with the THF on the right of the image and ETOH on the left.

After sparging both solutions (100 mL of 8 wt.% of A-POSS: EB) for about 30 minutes, 5 mL was quickly transferred into glass vials and immediately sealed. The solutions were cured using the Novacure Hg lamp without the 365 nm filter for one hr. Thirty minutes was initially applied, however, there were still portions of uncured solution within the ethanol solution. The results for the sparged solution are shown in Figure 4.33, as a similar result was obtained from the non-sparged solution, leaving the possible difference to be the polymer structure formed. From the A-POSS/EB in THF sample, a gel-like appearance was achieved indicative of a gel

photopolymerization occurring with a high degree of crosslinking to form the network structure of the gel. After drying to remove the THF, the product became a hard and brittle material. The ethanol product became a powdery material after drying. The difference in the electrodeposited film was not as stark, as the THF film and EtOH film are still transparent. The ethanol exhibited a yellow tinge majority of the time for semi-cured coatings. A fully cured deposit would infrequently produce a white deposit. Possible solvent-monomer interactions should as be considered as they may have led to a white deposition observed. Ethanol as a solvent could not be considered for further ES experiments as transparency is needed for optimal photo-polymerization.

The SEM confirmed a different morphology was observed even though there was no visual difference between the THF films with or without sparging. The non-sparged sample in Figure 4.34, typically showed a smooth surface or more flatten bead-like (bumpy) pattern as if the shell did not have enough time to become more rigid prior to hitting the collector.

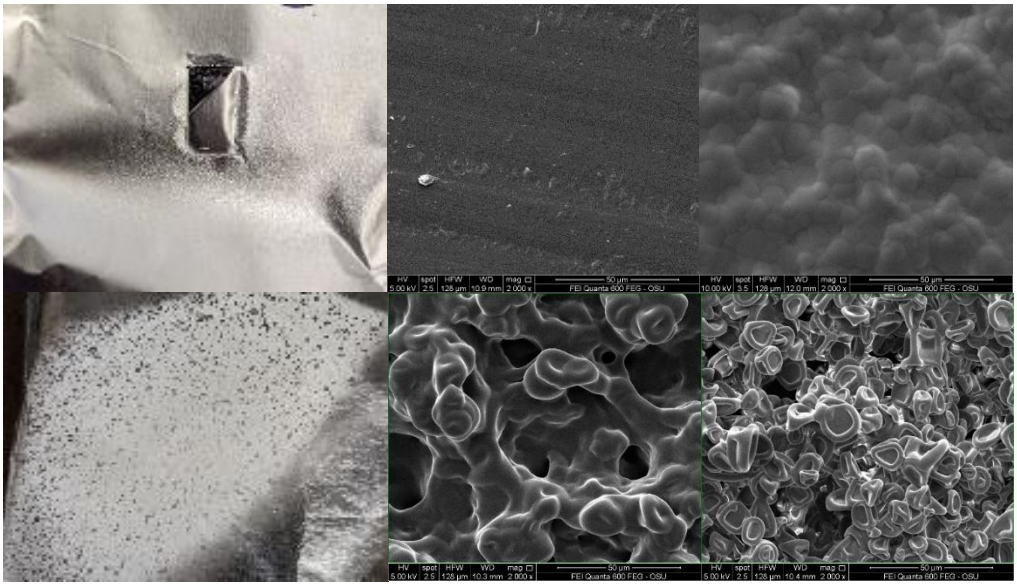

Figure 4.34: Image of A-POSS/EB sample created with unsparged (top) and sparged (bottom) solution of THF. SEM image magnification is 2,000x.

After sparging, a beading pattern was shown for the two samples in the bottom row (Figure 4.34). The only difference in parameters between the two was the distance from the collector with the sample on the bottom-right one cm closer than the bottom middle image. The bead morphology is more distinct with the droplet size visible with just that slight change in distance. It also showed that a rigid shell was fully developed before collection as further curing shrunk the bead shape giving them a "blood platelet" look. The sample collected one cm back depicts a different occurrence as the shell was not fully developed enough to maintain its shape, creating a porous network web of partial beads. A subsequent trial to repeat this effect saw a return to the bumpy film morphology again highlighting the inconsistency in morphologies.

An FTIR analysis was performed to detect any difference in the functional group chemistry for both cured materials. From the spectra shown in Figure 4.35, there is no difference between the ethanol and THF samples. However, the difference between the uncured and cured samples does bring into the question why the N-H, C-H, and C=O peaks virtually disappeared as these peaks are still present based on previous data collected from a cured A-POSS/EB sample as the disappearance of the C=C bond is expected at about 1650 cm^{-1}. Both samples were run twice obtaining the same results, leaving the assumption that either these functional groups disappeared when curing in solution or both materials were not transmitting the infrared beam well enough to distinctly detect the chemical bonds for a proper analysis due to the low intensity of the peaks. XRD was performed to help determine the crystal structure of the polymer and better understand the degree of crystallinity. Two samples were used to observe for any differences in the chemical structure between the THF and ethanol cured in solution. The XRD graph in Figure 4.35 shows a broad peak for both samples, which was expected of an amorphous material, with a decrease in peak area for the THF sample. A similar trend also indicated that there may not be a possible difference in structure, however, this cannot be concluded without a proper analysis of the polymer structure.

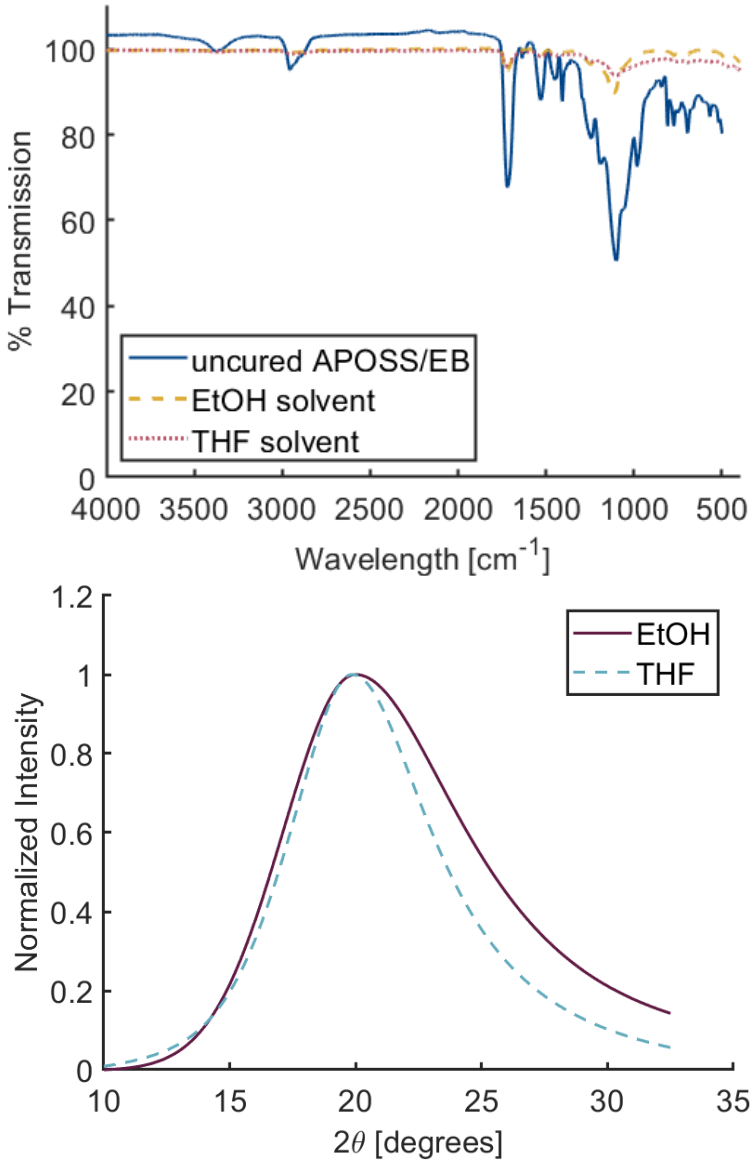

Figure 4.35: FTIR spectra of A-POSS/EB cured in ethanol and THF (left). XRD of A-POSS: EB polymer cured in a solution of EtOH and THF (right).

Using the deposited weight, the efficiency of the electrospinning trials was evaluated and compared based on the needle gauge and distance from the sample. The surface area of deposition was not considered due to factors influencing the travel path such as jet arcing and deposition in the application area of the UV light. For the needle gauge samples, the distance (17 cm), flow rate (0.5 mL/hr), and applied voltage (within groups) were kept as consistent as much as possible leaving only the needle gauge (20, 22, and 25 Ga) as the dependent variable. The distance samples had the same applied voltage (within groups). The flow rate (0.5 mL/hr) and needle gauge (20

Ga) were held constant. The distance to collectors explored were 10, 17, and 24 cm. The equipment and environment (nitrogen and vacuum) were the same for all the samples with an ES duration of one hour. An 8 wt.% A-POSS/EB THF solution was used for these trials.

Based on the plots in Figure 4.36, an increase in deposition was recorded with an increase in needle gauge. An increase in deposition with an increase in needle diameter was not expected as the reduction in the droplet radius could have led to less

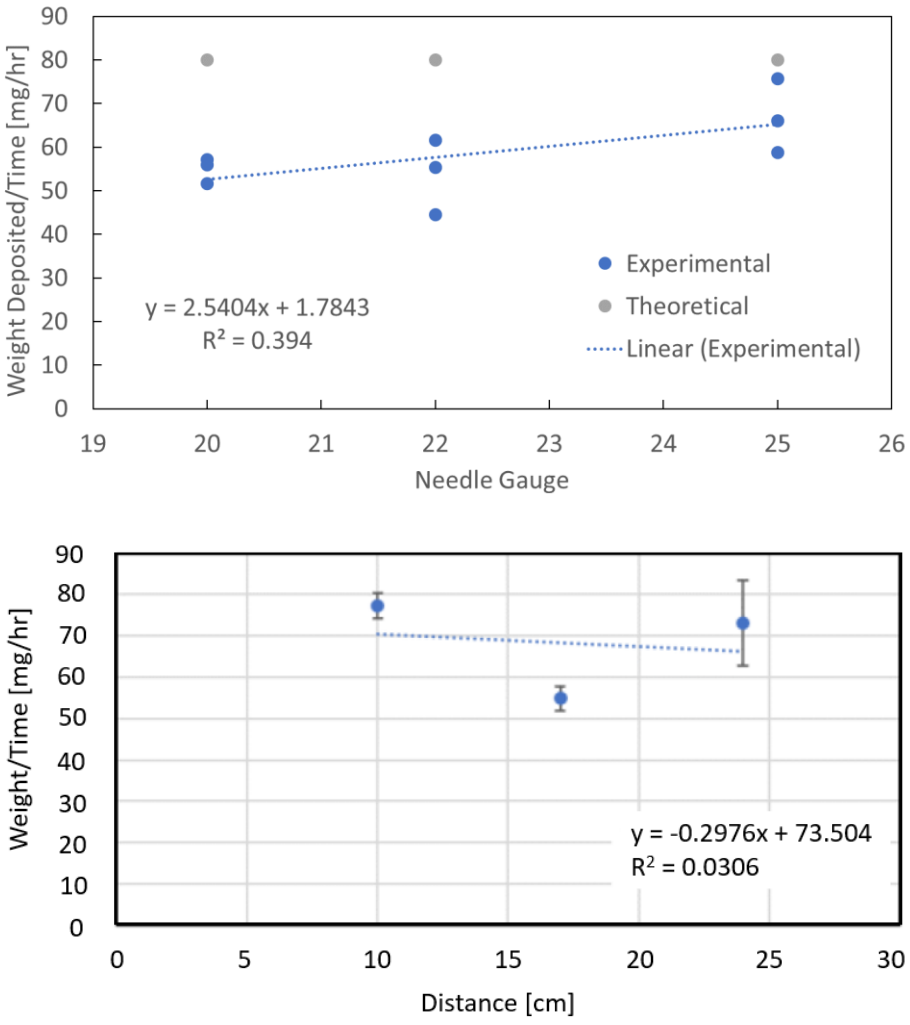

Figure 4.36: Plot depicting the effect the needle gauge and distance have on the weight of the sample

material depositing. However, the reduction in droplet radius would have helped to reduce jet branching and improve the amount of material deposited on the collector. An increased distance should have led to a decrease in the deposition as the droplet size will shrink the further it travels, increasing the chances of having jet branching. The increased deposition at 24 cm is seen as an outlier and could be due to the collector design as the first two distances showed the expected trend. The collector was an Al sheet covered in Al foil with a ground cable connected towards the back. The arcing of the solution towards the back of the collector was an issue as deposit was found on the back of the Al sheet and alligator clip for the ground cable.

A sample size (n = 3) does not allow for a proper statistical comparison as changes in equipment eliminated many of the samples collected. As the equipment changed throughout the project, the effects of changing the hardware were observed. The applied voltage was influenced by a change in the positive voltage clip where switching to a smaller clip reduced the applied voltage needed to produce a cone shape. A change in collector improved deposition but did not fully address the issues relating to the jet arcing that were observed with the initial collector design for the cylinder set-up. Even changing the UV position due to overcuring at the needle tip improved the amount of cured sample but introduced an issue regarding the film shape.

4.3 A-POSS/Ebecryl composites with filler [Microphenoset (MP), Glass fibers (GF), Hollow glass microballoons (HGMB)

The A-POSS/EB composites were studied using glass fibers, hollow glass microballoons, or microphenosets as reinforcements (Figure 4.37) to evaluate thermal degradation behavior under high temperatures as TPS are typically reinforced with carbon or silica-based materials for increased thermal stability and mechanical properties (Table 4.5).

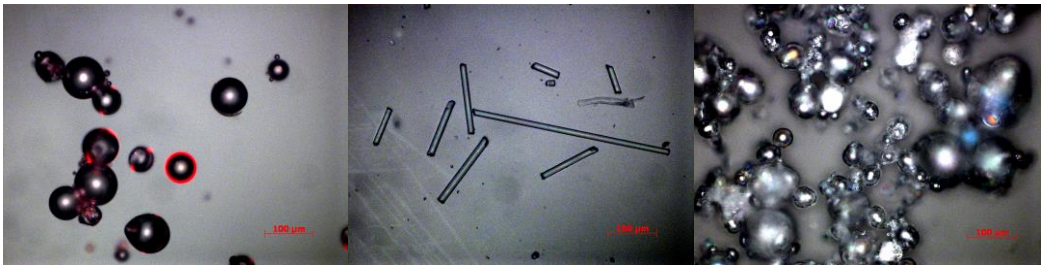

Figure 4.37: Optical images of filler material, MP, GF, and HGMB. (From left to right, 20x magnification)

Table 4.5: Filler physical properties

	MP	GF	HGMB
Appearance	Red-brown, fine powder	Solid, white to grey	Solid, white powder
Density [g/cm^3]	0.2 – 0.8	2.55 – 2.58	2.35
Melting point [^{o}C]	N/A	>800	N/A
Average diameter [μm]	52.72 ± 17.90	16	44.42 ± 24.88
Average length [μm]	N/A	162.46 ± 74.17	N/A

4.3.1 A-POSS/EB reinforced cast samples

Cast samples were created to compare traditional methods of producing cured material to ES. The casting mold were semi-transparent silicone molds to allow for UV light to cure the samples and easy sample removal. The cast solutions were prepared using 5 g A-POSS/EB (1:1 ratio) with 4 wt.% TPO per total monomer weight and 5 wt.% of filler per total amount of monomer and TPO. 5 mL of ethanol was added to decrease the viscosity of the solution and allow for easier mixing overnight and pouring into the molds. 5 mL of the dilute solution was pipetted out into the mold and left overnight to evaporate as much of the ethanol as possible (Figure 4.38).

The solutions were then cured using the Xe and H lamps. An initial attempt using only the Xe lamp showed issues in the sample bowing due to the high light intensity and unevenness of the curing from the front and back of the samples. A repeat trial used a Hg lamp for 2 hours along the front and sides of the sample first to create the shell of the sample followed by the Xe lamp to cure in the inner portion. This help to create a flatter sample with better uniformity and less uncured residual.

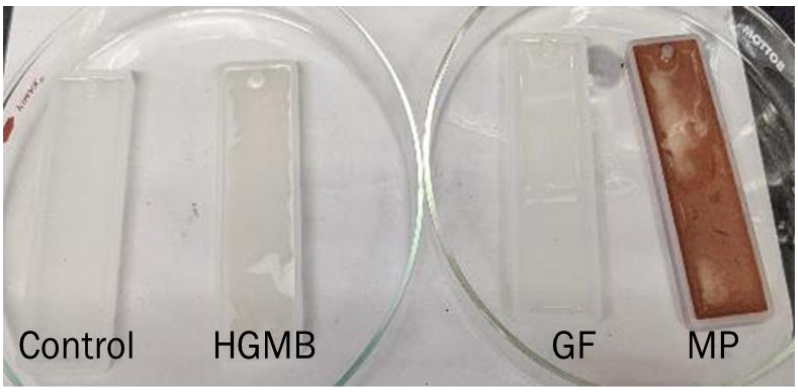

Figure 4.38: Cast sample created of A-POSS/EB with HGMB, GF, and MP fillers.

A TGA analysis (Figure 4.39) of the cast samples showed that the GF and HGMB performed better than the MP. The MP sample showed a large decrease in weight earlier than the control which can be attributed to the degradation of the MP.

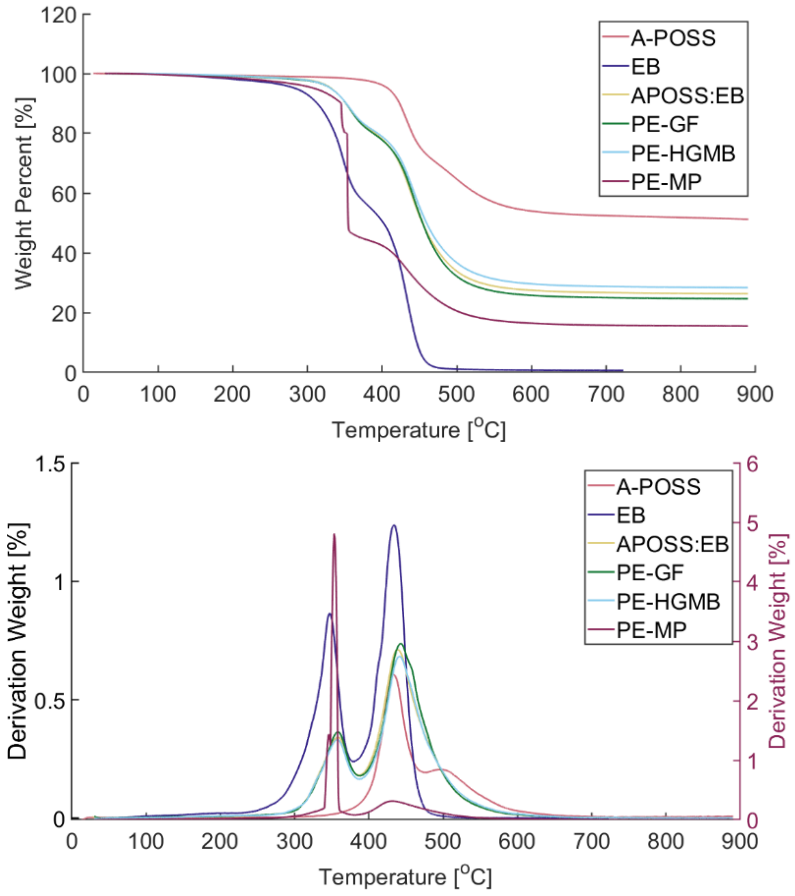

Figure 4.39: TGA and DTG of cast samples

While the GF and HGMB showed an earlier onset of degradation than the control, the difference was not great enough to be significant. Comparing residual amount, an increase in residual was expected for the GF and HGMB samples, however, the control sample showed a greater amount. As the presence of the SiO_2 core within the A-POSS contributes greatly to the residual left after thermal degradation, the offset of material with the addition of the filler should have still resulted in an increase. The DSC of the cast molds, shown in Figure 4.40, was collected to observe if a glass transition temperature appeared on the 2nd heating ramp and the melt flow behavior. For the cast molds, a Tg was only observed for the EB and A-POSS/EB samples. The T_g in the A-POSS/EB is attributed to the EB content as no T_g is observed for the A-POSS run.

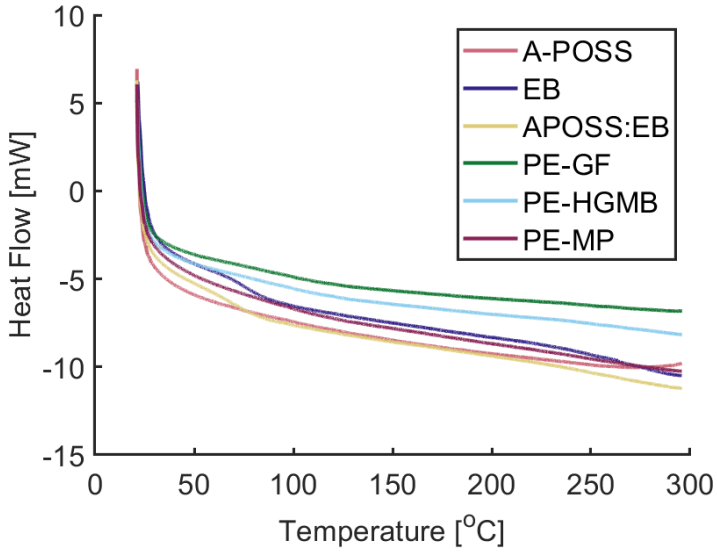

Figure 4.40: DSC of A-POSS/EB cast samples

4.3.1 A-POSS/EB reinforced film samples

The fillers were introduced into the solution before electrospinning. All fillers showed issues with staying in the solution, with the MP and HGMB floating at the top of the sample and the GF staying half in the solution but sinking to the bottom over time. This was to be expected as the difference in densities between the solutions and the fillers would not allow them to stay in the solution long enough to be

electrodeposited. Due to this, the ES set-up was changed to include a magnetic stirrer to mix the solution within the syringe using a tiny magnetic stir bar. (Figure 4.41)

The first filler trials performed used just 5 wt.% filler in order to provide a comparative analysis of the cast samples. This amount was later increased as visual inspection of the MP samples showed no filler present on the film. This filler was selected to judge the filler deposition due to its color standing out more. A second run-through with 10 wt.% showed some deposition of the MP and GF but very little

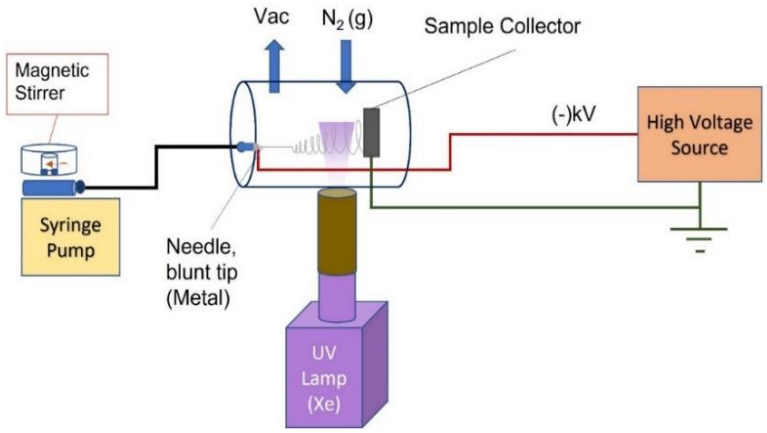

Figure 4.41: ES set-up for reinforced films with the addition of a magnetic stirrer.

of the HGMB when viewed under SEM and an optical microscope. Compared to the amount present in the solution and the amount deposited in the film, it was suspected that there was an issue in the ES set-up. An inspection of the equipment showed this to be true as the majority of the filler bottlenecked within the plastic body of the needle and settle there. As the MP and HGMB have a tendency to agglomerate in solution, the design of the needle body increased the possibility of the filler settling out of the solution, resulting in less deposition. The filler amount was then increased to 15 wt.% in hopes to compensate for this as a new design of the needle was not feasible at the time.

The parameters used for the successful trials are listed in Table 4.6, with the distance and flow rate were held constant at 17 cm and 0.55 mL/hr., respectively, to evaluate the applied voltage due to the presence of the fillers in the solution. The applied voltage for the GF is the only one to show a large increase while the others only show

an insignificant increase as applied voltage tends to drift ±1.5 kV for the same solutions.

Table 4.6: ES parameters used for reinforced composite films

Sample	Applied Voltage [kV]
A-POSS/EB	11.5
A-POSS/EB - MP	12
A-POSS/EB - GF	15.5
A-POSS/EB - HGMB	12.5

At 15 wt.% filler content, deposition was observed as shown in Figure 4.42 - Figure 4.44, in the optical and the SEM images.

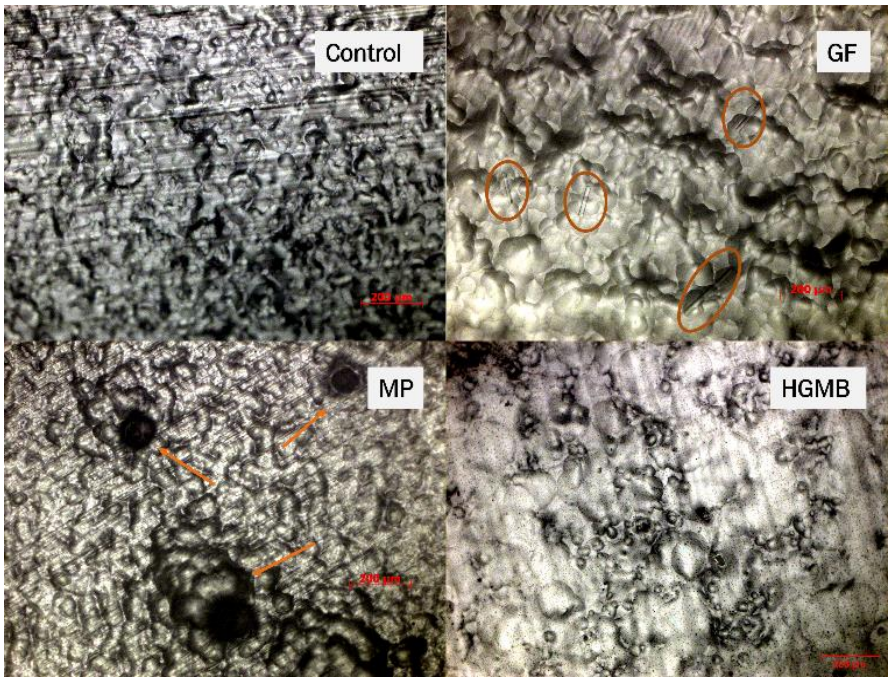

Figure 4.42: Optical images of the reinforced film composites at 10x magnification.

As expected, there was a sparse amount of filler presence due to them settling out of the solution during fluid transport. The GF and MP are easily detected at 10x magnification due to the color, shape, and size of the material. HGMBs are more clearly visible at 20x (Figure 4.45) magnification due to their smaller diameter.

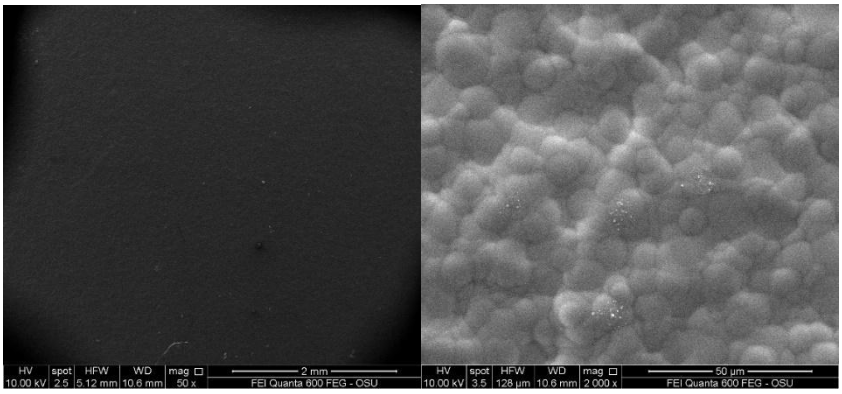

Figure 4.43: SEM image of control film sample taken at 50x (left) and 2,000x (left) magnification.

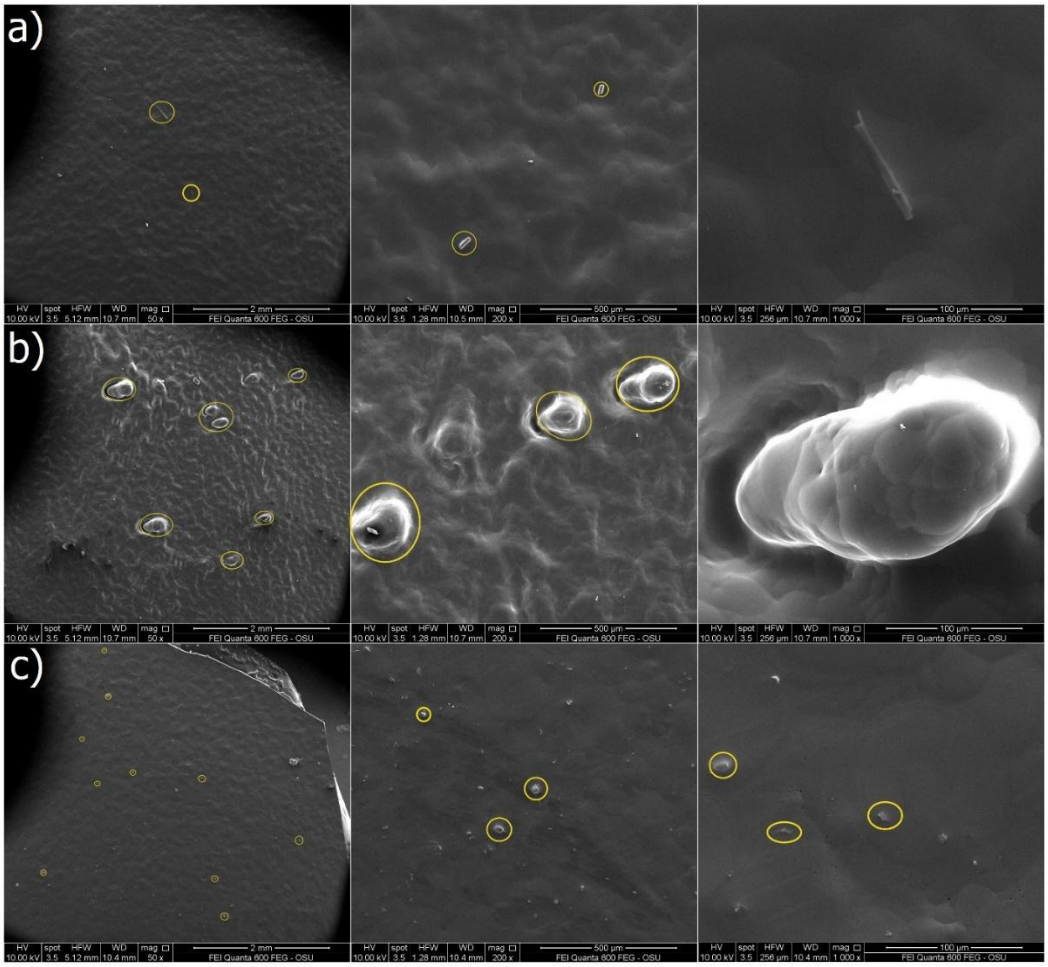

Figure 4.44: SEM image of filler for a) GF, b) MP, and c) HGMB. The magnifications used from left to right are 50x, 200x, and 1,000x.

An SEM image of the control film (Figure 4.43) shows that a bead-like deposition likely occurred due to the flattened round-like morphology shown. This feature was

viewed across a majority of the electrodeposited samples using A-POSS/EB for this trial. The appearance of the filler on the surface of the films is shown in Figure 4.44 as the GF lies on top of or embedded in the film. The MPs are embedded in the film coated with the matrix material while the HGMB are embedded in the film with broken shards viewed at 1000x. Some breakage of the HGMB during processing was expected as this has been reported in the literature.[135] Due to the smaller size of the HGMB in the film, a single image of a microballoon is shown in Figure 4.45, further highlighting the size difference in the fillers.

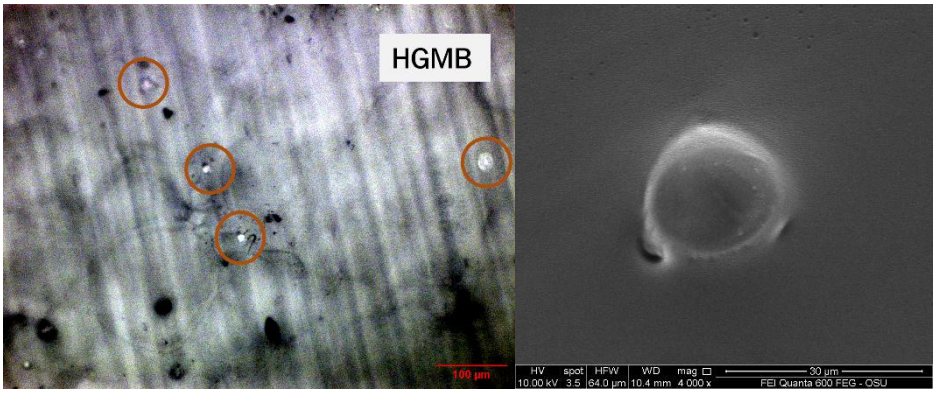

Figure 4.45: HGMB reinforced composite film taken with an optical microscope at 20x (left). An SEM image of a single HGMB is shown on the right at 4,000x magnification. (right)

The thermal analysis of the reinforced composite samples showed that due to the amount of filler present in the samples, a notable significance could not be observed as was seen with the cast samples. Figure 4.46 shows that a similar plot for each filler was obtained nearly overlapping the control with some slight weight loss under 200 ^{o}C for the HGMB and control. The most significant difference between the cast and film samples is the absence of the degradation peak for MP, which was caused by the MP filler. This missing peak in the DTG was an obvious indication that the amount of filler presence was not enough to have an impact on the degradation of A-POSS/EB matrix.

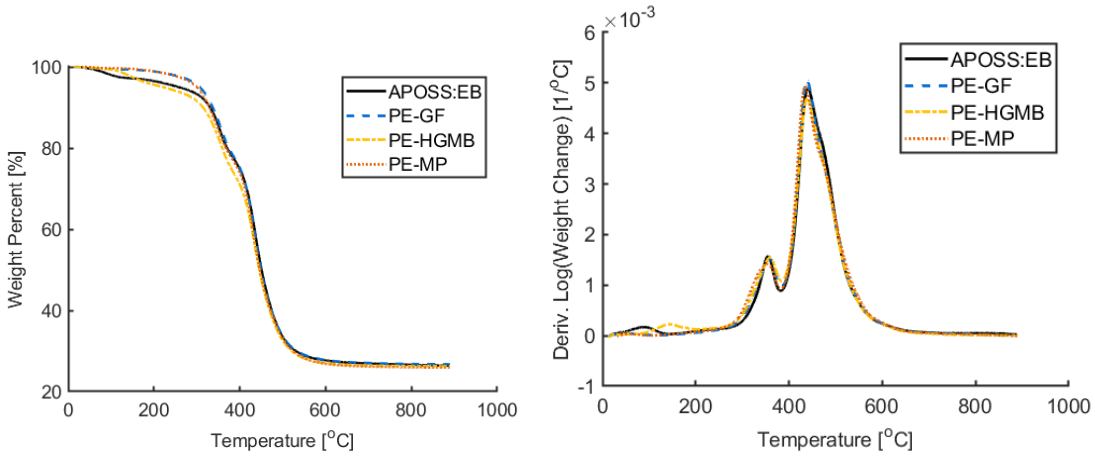

Figure 4.46: TGA (left) and DTG (right) of control and filled film samples

A comparison of the mold and cast samples is shown in Table 4.7, where the initial weight loss and residual weight are stated. Evaluating the thermal behavior of the cast and film samples, the cast samples exhibited a higher degree of thermal resistance comparing the 5% weight loss values. For the residual weight, the cast and film samples are similar in range with the exception of the hollow glass microballoon and microphenoset cast samples performing better and worst, respectively, compared to the film samples.

Table 4.7: Comparison of thermal degradation behavior for cast and ES samples

		5% weight loss [°C]	Residual Weight [%]
Cast	A-POSS	407.89	51.24
	EB	284.16	0.6849
	A-POSS/EB	332.01	26.36
	A-POSS/EB - MP	309.71	15.51
	A-POSS/EB - HGMB	331.31	28.38
	A-POSS/EB - GF	331.36	24.66
ES	A-POSS/EB	259.05	26.40
	A-POSS/EB - MP	300.03	25.91
	A-POSS/EB - HGMB	222.91	26.26
	A-POSS/EB - GF	307.21	26.76

Chapter 5 Conclusion

The use of electrodeposition as an additive manufacturing method for the production of thermal protection systems was evaluated in this work. Thermal protection systems are an essential component of space vehicles that protect the interior from thermal damage. Ablative TPS are used in high-velocity entry applications and primarily protect the space vehicle through a charring mechanism, which generates a char layer and pyrolysis gas to reduce heat transfer between the heat source and base material of the space vehicle. Current manufacturing of TPS is costly due to the specialty materials used and the labor intensity of the manufacturing process. Additive manufacturing, via electrodeposition, was investigated as a cost-effective technique with an environmentally friendly aspect using photopolymerization to produce a viable reinforced composite for ablative applications.

The electrodeposition process was designed for a composite film using cure in-flight photopolymerization. The design was optimized for an acrylate monomer system with an inert environment using nitrogen gas and a constant vacuum applied to maintain atmospheric pressure. The application of the UV light was introduced perpendicular to the flight path between the needle tip and the collector to allow for a greater degree of exposure as the electrocharged droplets traveled to the collector. The electrodeposition parameters (applied voltage, flow rate, and distance from the needle to the collector) were optimized through various trials for film production. Special attention was given to the applied voltage to ensure that a Taylor cone formed for each trial. THF was selected to conduct the electrodeposition for the matrix and reinforced composite films following the solvent trials which showcased its ability to form a cured film. The composite films formed were post-cured to ensure complete polymerization before testing. The curing of the films was evaluated using FTIR, which showed a reduction of the double carbon bonds indicative of the acrylate bonds breaking and forming the polymer chains. The XRD analysis of the film showcased an amorphous material with a confirmation peak for the Si-O-Si linkages present in the cured film for the A-POSS/EB sample. The main surface morphology of the film

was flattened droplets with a bead-like deposition. This feature of the film's surface was indicative of electrospraying conditions. The other features observed showed a more-distinct bead-like shaped or fiber-like material on the surface which showed that some degree of electrospinning occurred. The films were overall non-porous with a transparent appearance.

The thermal behavior of the matrix and reinforce materials were compared using a casting method and electrodeposition. The cast samples were prepared with a 5% filler content using A-POSS/EB as the matrix. The film samples used a filler content of 15% due to a slight design issue. The thermal degradation profile of the control and reinforced cast samples showed that the hollow glass microballoons samples exhibited an increase in char residual while maintaining a thermal degradation profile similar to the A-POSS/EB control. The initial onset of thermal degradation was higher for the silica-based filler (glass fiber and hollow glass microballoons) composites compared to the carbon-based filler (microphenoset). The reinforced film samples exhibited similar thermal degradation profiles to the control A-POSS/EB film. The DSC data evaluated for the cast samples showed that the filled samples were cured when assessing the second heating curve with the presence of a glass transition and crystallization peak for the EB and A-POSS/EB.

This work provides an initial evaluation of electrodeposition as a manufacturing technique for ablative TPS. The cure in-flight electrodeposition was able to produce a fully cured film using photopolymerization offering an alternative to thermal curing processes. Successful films produced demonstrated high thermal stability for control and reinforced samples. The A-POSS cast composites exhibited the best char residual close to the NASA specifications. The cast samples showed that HGMB was the best filler to increase the char residual of the A-POSS/EB cast composites. Issues and setbacks associated with electrodeposition of the reinforced composite films are addressed in Chapter 5.1 for future recommendations. The use of A-POSS as part of a TPS matrix does have an advantage over traditional matrix material due to its inorganic base structure. The inorganic nature of A-POSS can lessen the need for additional inorganic fillers to aid in the char formation compared to TPS systems that

use an additive to increase their inorganic content. Pairing it with a second monomer, such as EB, can increase flexibility and maintain a thermal behavior close to the original material which would be ideal for future research investigating A-POSS for re-entry applications.

5.1 Future recommendations

Due to the purpose of using this technique for TPS manufacturing, there were some setbacks associated with solvent, process environment, and reproducibility of the film's surface morphology. The initial solvent used to electrodeposit the matrix material, ethanol, was selected to provide a safe alternative to commonly used solvent systems with the hopes of achieving successful film production. Ethanol proved to be a concern because of the presence of dissolved oxygen within the solvent. Oxygen inhibition had a huge effect on the curing process. The amount of dissolved oxygen in ethanol inhibited the production of free radicals available for polymerization resulting in consistently under-cured films on the collector. The introduction of an inert atmosphere had virtually no effect on this. As shown after sparging the ethanol solution with nitrogen, a greater degree of curing was observed. Even at the needle tip compared to prior trials. Similar results were observed with the THF, indicating that any oxygen present within the solvent will prove to be a hindrance. A potential solution for this would be to increase TPO concentration above 3 wt.% per total monomers as the presence of more photoinitiators has been reported to help overcome issues related to oxygen inhibition in literature as more could be added to a solution to avoid the removal process for 4-methoxyphenol (MeHQ), a typical inhibitor found in acrylate polymers including the ones in this study. Another solution would be to introduce a second photoinitiator to act as an oxygen scavenger for a two-component system. Photopolymerization is driven by the creation of the free radicals when the photoinitiator reacts with a UV light source. It is essential to choose the most optimal photoinitiators that will not easily be quenched by dioxygen molecules present in the environment or solvent. A second photoinitiator can also help reduce the need for an inert environment making electrodeposition of the A-POSS/EB more feasibly for a standard manufacturing condition.

The surface morphology of the film is an important aspect to track during electrodeposition. The film's surface morphology is an indication of the condition in which electrodeposition is occurring: electrospraying or electrospinning. The common surface morphology observed was flattened bead-like shapes suggesting electrospraying conditions. Evidence of electrospinning was observed but unreproducible under the same conditions. The films produced were also non-porous with no visible void space. Parameters that can affect the morphology of the films are the solution viscosity and the amount of UV light applied. While these parameters were not evaluated, they do influence the electrodeposition conditions (viscosity) and affect the degree of curing (UV light) the electrocharged droplets undergo before reaching the grounded collector. Two ways in which to investigate viscosity are to evaluate the monomer concentration and the solvent system. As shown in the solvent study, the use of THF did help with the film production but the lack of fiber formation could be attributed to the viscosity. If the solution viscosity or concentration is too low, electrospraying is more likely to occur, creating beads rather than fibers. The application of the UV light which initiates the polymerization should be measured and observed using optical microscopy and SEM to visually judge the electrodeposition condition based on the appearance of the bead- or fiber-like material.

The creation of the reinforced composite film was an important metric to highlight the abilities of electrodeposition. Filler was observed to be present within the samples, however all samples displayed an uneven filler distribution. After a thorough inspection of the equipment was performed, the lack of filler was revealed to be a result of agglomeration within the polymer body of the needle. Most of the filler gathered around the opening to the metal portion as the shape of the polymer body was a bottleneck. The filler content was increased from 5 wt.% to 15 wt.% compensate for this. The solution to this would be to use a capillary or needle with a flat or taper shape with no grooves that could lead to filler dropout. With this design adjustment, evenly distributed reinforced films will be obtainable for a comparative analysis of their thermal properties.

Chapter 6 Bibliography

(1) Venkatapathy, E.; Ellerby, D.; Gage, P.; Prabhu, D.; Gasch, M.; Kazemba, C.; Kellerman, C.; Langston, S.; Libben, B.; Mahzari, M.; Milos, F.; Murphy, A.; Nishioka, O.; Peterson, K.; Poteet, C.; Splinter, S.; Stackpoole, M.; Williams, J.; Young, Z. Entry System Technology Readiness for Ice-Giant Probe Missions. *Space Sci. Rev.* **2020**, *216* (2), 22. https://doi.org/10.1007/s11214-020-0638-2.

(2) Venkatapathy, E.; Szalai, C. E.; Laub, B.; Hwang, H. H.; Conley, J. L.; Arnold, J. Thermal Protection System Technologies for Enabling Future Sample Return Missions. *NASA Sol. Syst. Explor.* **2017**, 8.

(3) Johnson, S. M. Thermal Protection Materials and Systems: Past, Present, and Future, 2013.

(4) Kafi, A.; Wu, H.; Langston, J.; Atak, O.; Kim, H.; Kim, S.; Fahy, W. P.; Reber, R.; Misasi, J.; Bateman, S.; Koo, J. H. Evaluation of Additively Manufactured Ultraperformance Polymers to Use as Thermal Protection Systems for Spacecraft. *J. Appl. Polym. Sci.* **2020**, *137* (37), 49117. https://doi.org/10.1002/app.49117.

(5) Haider, S.; Haider, A. *Electrospinning - Material, Techniques, and Biomedical Applications*; 2016. https://doi.org/10.5772/62860.

(6) Xue, J.; Wu, T.; Dai, Y.; Xia, Y. Electrospinning and Electrospun Nanofibers: Methods, Materials, and Applications. *Chem. Rev.* **2019**, *119* (8), 5298–5415. https://doi.org/10.1021/acs.chemrev.8b00593.

(7) Zagho, M. M.; Elzatahry, A. Recent Trends in Electrospinning of Polymer Nanofibers and Their Applications as Templates for Metal Oxide Nanofibers Preparation. *Electrospinning - Mater. Tech. Biomed. Appl.* **2016**. https://doi.org/10.5772/65900.

(8) Wu, L.; Lu, S.; Pan, L.; Luo, Q.; Yang, J.; Hou, L.; Li, Y.; Yu, J. Enhanced Thermal and Mechanical Properties of Polypropylene Composites with Hyperbranched Polyester Grafted Sisal Microcrystalline. *Fibers Polym.* **2016**, *17* (12), 2153–2161. https://doi.org/10.1007/s12221-016-6257-6.

(9) Chapline, G.; Rodriguez, A.; Snapp, C.; Pessin, M.; Bauer, P.; Steinetz, B.; Stevenson, C. Thermal Protection Systems. **2015**, 18.

(10) Mishra, J. K.; Rao, C. S. P.; Bose, P. S. C.; Nath, N. K.; Rao, G. R. Experimental Studies of Resin Systems for Ablative Thermal Protection System. *Def. Sci. J.* **2021**, *71* (2), 289–295. https://doi.org/10.14429/dsj.71.16252.

(11) Qian, W.; He, K.; Zhou, Y. Estimation of Surface Heat Flux for Ablation and Charring of Thermal Protection Material. *Heat Mass Transf.* **2016**, *52* (7), 1275–1281. https://doi.org/10.1007/s00231-015-1653-9.

(12) Liu, S.; Zhang, B. Experimental Study on a Transpiration Cooling Thermal Protection System. *Sci. China Technol. Sci.* **2010**, *53* (10), 2765–2771. https://doi.org/10.1007/s11431-010-4055-8.

(13) Yuan, G.; Yang, B.; Chen, Y.; Jia, Y. Synthesis of a Novel Multi-Structure Synergistic POSS-GO-DOPO Ternary Graft Flame Retardant and Its

Application in Polypropylene. *Compos. Part Appl. Sci. Manuf.* **2019**, *117*, 345–356. https://doi.org/10.1016/j.compositesa.2018.12.006.

(14) Amar, A. J.; Oliver, B.; Kirk, B.; Salazar, G.; Droba, J. Overview of the CHarring Ablator Response (CHAR) Code. In *46th AIAA Thermophysics Conference*; American Institute of Aeronautics and Astronautics: Washington, D.C., 2016. https://doi.org/10.2514/6.2016-3385.

(15) Li, W.; Huang, H.; Zhang, Z.; Xu, X. Effects of Gradient Density on Thermal Protection Performance of AVCOAT Composites under Varied Heat Flux. *Polym. Compos.* **2016**, *37* (4), 1034–1041. https://doi.org/10.1002/pc.23263.

(16) Torre, L.; Kenny, J. M.; Maffezzoli, A. M. Degradation Behaviour of a Composite Material for Thermal Protection Systems Part I–Experimental Characterization. *J. Mater. Sci.* **1998**, *33* (12), 3137–3143. https://doi.org/10.1023/A:1004399923891.

(17) Li, W.; Huang, H.; Tian, Y.; Zhao, Z. Nonlinear Analysis on Thermal Behavior of Charring Materials with Surface Ablation. *Int. J. Heat Mass Transf.* **2015**, *84*, 245–252. https://doi.org/10.1016/j.ijheatmasstransfer.2015.01.004.

(18) Sawant, S. S.; Rao, P.; Harpale, A.; Chew, H. B.; Levin, D. A. Multi-Scale Thermal Response Modeling of an AVCOAT-like Thermal Protection Material. *Int. J. Heat Mass Transf.* **2019**, *133*, 1176–1195. https://doi.org/10.1016/j.ijheatmasstransfer.2018.12.182.

(19) Xiao, J.; Jiang, L.; Xu, Q. Insight into Chemical Reaction Kinetics Effects on Thermal Ablation of Charring Material. *Therm. Sci.* **2022**, *26* (1 Part B), 529–543. https://doi.org/10.2298/TSCI201010085X.

(20) Xiao, J.; Das, O.; Mensah, R. A.; Jiang, L.; Xu, Q.; Berto, F. Ablation Behavior Studies of Charring Materials with Different Thickness and Heat Flux Intensity. *Case Stud. Therm. Eng.* **2021**, *23*, 100814. https://doi.org/10.1016/j.csite.2020.100814.

(21) Bessire, B. K.; Lahankar, S. A.; Minton, T. K. Pyrolysis of Phenolic Impregnated Carbon Ablator (PICA). *ACS Appl. Mater. Interfaces* **2015**, *7* (3), 1383–1395. https://doi.org/10.1021/am507816f.

(22) Pesci, P. G. S.; Araújo Machado, H.; de Paula e Silva, H.; Paterniani Rita, C. C.; Filho, G. P.; Botelho, E. C. Numerical-Experimental Analysis of a Carbon-Phenolic Composite via Plasma Jet Ablation Test. *Mater. Res. Express* **2018**, *5* (6), 065601. https://doi.org/10.1088/2053-1591/aac624.

(23) Tran, H. K.; Rasky, D. J.; Esfahani, L. Thermal Response and Ablation Characteristics of Lightweight Ceramic Ablators. *J. Spacecr. Rockets* **1994**, *31* (6), 993–998. https://doi.org/10.2514/3.26549.

(24) Natali, M.; Kenny, J. M.; Torre, L. Science and Technology of Polymeric Ablative Materials for Thermal Protection Systems and Propulsion Devices: A Review. *Prog. Mater. Sci.* **2016**, *84*, 192–275. https://doi.org/10.1016/j.pmatsci.2016.08.003.

(25) Lombardi, M.; Fino, P.; Malucelli, G.; Montanaro, L. Exploring Composites Based on PPO Blend as Ablative Thermal Protection Systems – Part I: The Role of Layered Fillers. *Compos. Struct.* **2012**, *94* (3), 1067–1074. https://doi.org/10.1016/j.compstruct.2011.10.019.

(26) Kumar, L. M.; Anandapadmanabhan, E. N.; Chakravarthy, P. Investigative Studies on the Critical Prepreg Variables Influencing the Functional Performance of Ablative Composites for Extreme Environments in Launch Vehicles and Re-Entry Missions. *Mater. Res. Express* **2019**, *6* (8), 085613. https://doi.org/10.1088/2053-1591/ab1ac7.

(27) Venkatapathy, E.; Laub, B.; Hartman, G. J.; Arnold, J. O.; Wright, M. J.; Allen, G. A. Thermal Protection System Development, Testing, and Qualification for Atmospheric Probes and Sample Return Missions: Examples for Saturn, Titan and Stardust-Type Sample Return. *Adv. Space Res.* **2009**, *44* (1), 138–150. https://doi.org/10.1016/j.asr.2008.12.023.

(28) Tucker, N.; Stanger, J. J.; Staiger, M. P.; Razzaq, H.; Hofman, K. The History of the Science and Technology of Electrospinning from 1600 to 1995. *J. Eng. Fibers Fabr.* **2012**, *7* (2_suppl), 155892501200702S10. https://doi.org/10.1177/155892501200702S10.

(29) F.R.S, L. R. On the Equilibrium of Liquid Conducting Masses Charged with Electricity. *Lond. Edinb. Dublin Philos. Mag. J. Sci.* **1882**, *14* (87), 184–186. https://doi.org/10.1080/14786448208628425.

(30) Taylor, G. I. Disintegration of Water Drops in an Electric Field. *Proc. R. Soc. Lond. Ser. Math. Phys. Sci.* **1964**, *280* (1382), 383–397. https://doi.org/10.1098/rspa.1964.0151.

(31) Cooley, J. F. Apparatus for Electrically Dispersing Fluids. US692631A, February 4, 1902.

(32) Morton, W. J. Method of Dispersing Fluids. US705691A, July 29, 1902.

(33) Reneker, D. H.; Yarin, A. L.; Fong, H.; Koombhongse, S. Bending Instability of Electrically Charged Liquid Jets of Polymer Solutions in Electrospinning. *J. Appl. Phys.* **2000**, *87* (9), 4531–4547. https://doi.org/10.1063/1.373532.

(34) Yarin, A. L.; Koombhongse, S.; Reneker, D. H. Bending Instability in Electrospinning of Nanofibers. *J. Appl. Phys.* **2001**, *89* (5), 3018–3026. https://doi.org/10.1063/1.1333035.

(35) Yarin, A. L.; Koombhongse, S.; Reneker, D. H. Taylor Cone and Jetting from Liquid Droplets in Electrospinning of Nanofibers. *J. Appl. Phys.* **2001**, *90* (9), 4836–4846. https://doi.org/10.1063/1.1408260.

(36) Hohman, M. M.; Shin, M.; Rutledge, G.; Brenner, M. P. Electrospinning and Electrically Forced Jets. I. Stability Theory. *Phys. Fluids* **2001**, *13* (8), 2201–2220. https://doi.org/10.1063/1.1383791.

(37) Ma, M.; Krikorian, V.; Yu, J. H.; Thomas, E. L.; Rutledge, G. C. Electrospun Polymer Nanofibers with Internal Periodic Structure Obtained by Microphase Separation of Cylindrically Confined Block Copolymers. *Nano Lett.* **2006**, *6* (12), 2969–2972. https://doi.org/10.1021/nl062311z.

(38) Rutledge, G. C.; Fridrikh, S. V. Formation of Fibers by Electrospinning. *Adv. Drug Deliv. Rev.* **2007**, *59* (14), 1384–1391. https://doi.org/10.1016/j.addr.2007.04.020.

(39) Shin, Y. M.; Hohman, M. M.; Brenner, M. P.; Rutledge, G. C. Electrospinning: A Whipping Fluid Jet Generates Submicron Polymer Fibers. *Appl. Phys. Lett.* **2001**, *78* (8), 1149–1151. https://doi.org/10.1063/1.1345798.

(40) Angammana, C. J.; Jayaram, S. H. A Theoretical Understanding of the Physi-Cal Mechanisms of Electrospinning. **2011**, 9.
(41) Haghi, A. K. *Electrospinning of Nanofibers in Textiles*; Apple Academic Press: Toronto, 2012.
(42) Wendorff, J. H. *Electrospinning Materials, Processing, and Applications*; John Wiley & Sons, Inc: Weinheim ; Hoboken, New Jersey, 2012.
(43) Fuh, Y. K.; Chen, S. Z.; He, Z. Y. Direct-Write, Highly Aligned Chitosan-Poly(Ethylene Oxide) Nanofiber Patterns for Cell Morphology and Spreading Control. *Nanoscale Res. Lett.* **2013**, *8* (1), 97. http://dx.doi.org.ezproxy.proxy.library.oregonstate.edu/10.1186/1556-276X-8-97.
(44) Wang, Y.; Liu, F.; Xue, X. Morphology and Properties of UV-Curing Epoxy Acrylate Coatings Modified with Methacryl-POSS. *Prog. Org. Coat.* **2015**, *78*, 404–410. https://doi.org/10.1016/j.porgcoat.2014.07.003.
(45) Reneker, D. H.; Yarin, A. L. Electrospinning Jets and Polymer Nanofibers. *Polymer* **2008**, *49* (10), 2387–2425. https://doi.org/10.1016/j.polymer.2008.02.002.
(46) Carroll, C. P.; Joo, Y. L. Discretized Modeling of Electrically Driven Viscoelastic Jets in the Initial Stage of Electrospinning. *J. Appl. Phys.* **2011**, *109* (9), 094315. https://doi.org/10.1063/1.3582119.
(47) Han, T.; Yarin, A. L.; Reneker, D. H. Viscoelastic Electrospun Jets: Initial Stresses and Elongational Rheometry. *Polymer* **2008**, *49* (6), 1651–1658. https://doi.org/10.1016/j.polymer.2008.01.035.
(48) Hohman, M. M.; Shin, M.; Rutledge, G.; Brenner, M. P. Electrospinning and Electrically Forced Jets. II. Applications. *Phys. Fluids* **2001**, *13* (8), 2221–2236. https://doi.org/10.1063/1.1384013.
(49) YangYing; Zhidong, J.; Qiang, L.; Zhicheng, G. Controlling the Electrospinning Process by Jet Current and Taylor Cone. In *CEIDP '05. 2005 Annual Report Conference on Electrical Insulation and Dielectric Phenomena, 2005.*; 2005; pp 453–456. https://doi.org/10.1109/CEIDP.2005.1560718.
(50) Lee, J.; Sallam, K. a. Three-Dimensional Trajectory of Electrospun Polymer Solution Jet Using Digital Holographic Microscopy. *Polym. Eng. Sci.* **2014**, *54* (8), 1765–1773. https://doi.org/10.1002/pen.23725.
(51) Han, T.; Reneker, D. H.; Yarin, A. L. Buckling of Jets in Electrospinning. *Polymer* **2007**, *48* (20), 6064–6076. https://doi.org/10.1016/j.polymer.2007.08.002.
(52) Xin, Y.; Reneker, D. H. Hierarchical Polystyrene Patterns Produced by Electrospinning. *Polymer* **2012**, *53* (19), 4254–4261. https://doi.org/10.1016/j.polymer.2012.06.048.
(53) Angammana, C. J.; Jayaram, S. H. Fundamentals of Electrospinning and Processing Technologies. *Part. Sci. Technol.* **2016**, *34* (1), 72–82. https://doi.org/10.1080/02726351.2015.1043678.
(54) Thompson, C. J.; Chase, G. G.; Yarin, A. L.; Reneker, D. H. Effects of Parameters on Nanofiber Diameter Determined from Electrospinning Model.

Polymer **2007**, *48* (23), 6913–6922. https://doi.org/10.1016/j.polymer.2007.09.017.

(55) Fuh, Y.-K.; Chen, S.; Jang, J. S. C. Direct-Write, Well-Aligned Chitosan-Poly(Ethylene Oxide) Nanofibers Deposited via Near-Field Electrospinning. *J. Macromol. Sci. Part A* **2012**, *49* (10), 845–850. https://doi.org/10.1080/10601325.2012.714676.

(56) Fuh, Y. K.; Wang, B. S. Near Field Sequentially Electrospun Three-Dimensional Piezoelectric Fibers Arrays for Self-Powered Sensors of Human Gesture Recognition. *Nano Energy* **2016**, *30*, 677–683. https://doi.org/10.1016/j.nanoen.2016.10.061.

(57) Benavides, R. E.; Jana, S. C.; Reneker, D. H. Role of Liquid Jet Stretching and Bending Instability in Nanofiber Formation by Gas Jet Method. *Macromolecules* **2013**, *46* (15), 6081–6090. https://doi.org/10.1021/ma400900s.

(58) Ramakrishna, S.; Fujihara, K.; Teo, W.-E.; Lim, T.-C.; Ma, Z. *An Introduction to Electrospinning and Nanofibers*; World Scientific Publishing CoPteLtd, World Scientific Publishing Company, World Scientific Publishing: Singapore, 2005; Vol. 3. https://doi.org/10.1142/9789812567611_0003.

(59) Zuo, W.; Zhu, M.; Yang, W.; Yu, H.; Chen, Y.; Zhang, Y. Experimental Study on Relationship between Jet Instability and Formation of Beaded Fibers during Electrospinning. *Polym. Eng. Sci.* **2005**, *45* (5), 704–709. https://doi.org/10.1002/pen.20304.

(60) Luo, G.; Teh, K. S.; Liu, Y.; Zang, X.; Wen, Z.; Lin, L. Direct-Write, Self-Aligned Electrospinning on Paper for Controllable Fabrication of Three-Dimensional Structures. *ACS Appl. Mater. Interfaces* **2015**, *7* (50), 27765–27770. https://doi.org/10.1021/acsami.5b08909.

(61) Tripatanasuwan, S.; Zhong, Z.; Reneker, D. H. Effect of Evaporation and Solidification of the Charged Jet in Electrospinning of Poly(Ethylene Oxide) Aqueous Solution. *Polymer* **2007**, *48* (19), 5742–5746. https://doi.org/10.1016/j.polymer.2007.07.045.

(62) Bi, H.; Feng, T.; Li, B.; Han, Y. In Vitro and In Vivo Comparison Study of Electrospun PLA and PLA/PVA/SA Fiber Membranes for Wound Healing. *Polymers* **2020**, *12* (4), 839. https://doi.org/10.3390/polym12040839.

(63) Zhang, S.; Ye, J.; Sun, Y.; Kang, J.; Liu, J.; Wang, Y.; Li, Y.; Zhang, L.; Ning, G. Electrospun Fibrous Mat Based on Silver (I) Metal-Organic Frameworks-Polylactic Acid for Bacterial Killing and Antibiotic-Free Wound Dressing. *Chem. Eng. J.* **2020**, *390*, 124523. https://doi.org/10.1016/j.cej.2020.124523.

(64) Li, Y.; Bou-Akl, T. Electrospinning in Tissue Engineering. *Electrospinning - Mater. Tech. Biomed. Appl.* **2016**. https://doi.org/10.5772/65836.

(65) Pham, Q. P.; Sharma, U.; Mikos, A. G. Electrospinning of Polymeric Nanofibers for Tissue Engineering Applications: A Review. *Tissue Eng.* **2006**, *12* (5), 1197–1211. https://doi.org/10.1089/ten.2006.12.1197.

(66) Gao, J.; Zhu, J.; Luo, J.; Xiong, J. Investigation of Microporous Composite Scaffolds Fabricated by Embedding Sacrificial Polyethylene Glycol

Microspheres in Nanofibrous Membrane. *Compos. Part Appl. Sci. Manuf.* **2016**, *91*, 20–29. https://doi.org/10.1016/j.compositesa.2016.09.015.

(67) Forouharshad, M.; Putti, M.; Basso, A.; Prato, M.; Monticelli, O. Biobased System Composed of Electrospun Sc-PLA/POSS/Cyclodextrin Fibers To Remove Water Pollutants. *ACS Sustain. Chem. Eng.* **2015**, *3* (11), 2917–2924. https://doi.org/10.1021/acssuschemeng.5b00892.

(68) Gopal, R.; Kaur, S.; Ma, Z.; Chan, C.; Ramakrishna, S.; Matsuura, T. Electrospun Nanofibrous Filtration Membrane. *J. Membr. Sci.* **2006**, *281* (1), 581–586. https://doi.org/10.1016/j.memsci.2006.04.026.

(69) Balakrishnan, N. K.; Koenig, K.; Seide, G. The Effect of Dye and Pigment Concentrations on the Diameter of Melt-Electrospun Polylactic Acid Fibers. *Polymers* **2020**, *12* (10), 2321. https://doi.org/10.3390/polym12102321.

(70) Catalani, L. H.; Collins, G.; Jaffe, M. Evidence for Molecular Orientation and Residual Charge in the Electrospinning of Poly(Butylene Terephthalate) Nanofibers. *Macromolecules* **2007**, *40* (5), 1693–1697. https://doi.org/10.1021/ma061342d.

(71) Park, J. H.; Rutledge, G. C. Ultrafine High Performance Polyethylene Fibers. *J. Mater. Sci.* **2018**, *53* (4), 3049–3063. https://doi.org/10.1007/s10853-017-1724-z.

(72) Bellan, L. M.; Craighead, H. G. Nanomanufacturing Using Electrospinning. *J. Manuf. Sci. Eng.* **2009**, *131* (3), 034001. https://doi.org/10.1115/1.3123342.

(73) Banerji, A.; Jin, K.; Liu, K.; Mahanthappa, M. K.; Ellison, C. J. Cross-Linked Nonwoven Fibers by Room-Temperature Cure Blowing and in Situ Photopolymerization. *Macromolecules* **2019**, *52* (17), 6662–6672. https://doi.org/10.1021/acs.macromol.9b01002.

(74) Decker, C. UV-Radiation Curing Chemistry. *Pigment Resin Technol.* **2001**, *30* (5), 278. https://doi.org/10.1108/03699420110404593.

(75) Fairbanks, B. D.; Macdougall, L. J.; Mavila, S.; Sinha, J.; Kirkpatrick, B. E.; Anseth, K. S.; Bowman, C. N. Photoclick Chemistry: A Bright Idea. *Chem. Rev.* **2021**, *121* (12), 6915–6990. https://doi.org/10.1021/acs.chemrev.0c01212.

(76) Wang, S.; Wu, Y.; Dai, J.; Teng, N.; Peng, Y.; Cao, L.; Liu, X. Making Organic Coatings Greener: Renewable Resource, Solvent-Free Synthesis, UV Curing and Repairability. *Eur. Polym. J.* **2020**, *123*, 109439. https://doi.org/10.1016/j.eurpolymj.2019.109439.

(77) Masson, F.; Decker, C.; Jaworek, T.; Schwalm, R. UV-Radiation Curing of Waterbased Urethane–Acrylate Coatings. *Prog. Org. Coat.* **2000**, *39* (2), 115–126. https://doi.org/10.1016/S0300-9440(00)00128-4.

(78) Wang, X.; Hu, Y.; Song, L.; Xing, W.; Lu, H.; Lv, P.; Jie, G. UV-Curable Waterborne Polyurethane Acrylate Modified with Octavinyl POSS for Weatherable Coating Applications. *J. Polym. Res.* **2011**, *18* (4), 721–729. https://doi.org/10.1007/s10965-010-9468-3.

(79) Gupta, P.; Trenor, S. R.; Long, T. E.; Wilkes, G. L. In Situ Photo-Cross-Linking of Cinnamate Functionalized Poly(Methyl Methacrylate- *Co* -2-Hydroxyethyl Acrylate) Fibers during Electrospinning. *Macromolecules* **2004**, *37* (24), 9211–9218. https://doi.org/10.1021/ma048844g.

(80) Kim, S.-S.; Ha, H.; Ellison, C. J. Soybean Oil-Based Thermoset Films and Fibers with High Biobased Carbon Content via Thiol–Ene Photopolymerization. *ACS Sustain. Chem. Eng.* **2018**, *6* (7), 8364–8373. https://doi.org/10.1021/acssuschemeng.8b00435.

(81) Niu, Q.; Zeng, L.; Mu, X.; Nie, J.; Ma, G. Preparation and Characterization of Core-Shell Nanofibers by Electrospinning Combined with in Situ UV Photopolymerization. *J. Ind. Eng. Chem.* **2016**, *34*, 337–343. https://doi.org/10.1016/j.jiec.2015.12.006.

(82) Zhu, X.; Niu, Q.; Xu, Y.; Wu, G.; Li, G.; Nie, J.; Ma, G. From Small Molecules to Polymer Fibers: Photopolymerization with Electrospinning on the Fly. *J. Photochem. Photobiol. Chem.* **2018**, *353*, 101–107. https://doi.org/10.1016/j.jphotochem.2017.11.011.

(83) Ravve, A. *Principles of Polymer Chemistry*; Springer New York: New York, NY, 2012. https://doi.org/10.1007/978-1-4614-2212-9.

(84) Khudyakov, I. V. Fast Photopolymerization of Acrylate Coatings: Achievements and Problems. *Prog. Org. Coat.* **2018**, *121*, 151–159. https://doi.org/10.1016/j.porgcoat.2018.04.030.

(85) Ma, C.; Ma, S.; Chen, Y.; Wang, Y.; Ou, J.; Zhang, J.; Ye, M. Fast Fabrication and Modification of Polyoctahedral Silsesquioxane-Containing Monolithic Columns via Two-Step Photo-Initiated Reactions and Their Application in Proteome Analysis of Tryptic Digests. *Talanta* **2020**, *209*, 120526. https://doi.org/10.1016/j.talanta.2019.120526.

(86) Senyurt, A. F.; Wei, H.; Hoyle, C. E.; Piland, S. G.; Gould, T. E. Ternary Thiol−Ene/Acrylate Photopolymers: Effect of Acrylate Structure on Mechanical Properties. *Macromolecules* **2007**, *40* (14), 4901–4909. https://doi.org/10.1021/ma062534b.

(87) Mandal, B. M. *Fundamentals of Polymerization*; WORLD SCIENTIFIC, 2013. https://doi.org/10.1142/7882.

(88) Mayo, F. R.; Lewis, F. M.; Walling, C. (B) Propagation. Copolymerisation: The Effects of Structure on the Reactions of Ethylenic Bonds with Free Radicals. *Discuss. Faraday Soc.* **1947**, *2*, 285. https://doi.org/10.1039/df9470200285.

(89) Siegmann, R.; Beuermann, S. Individual Rate Coefficients for 1H,1H,2H,2H-Tridecafluorooctyl Methacrylate Radical Polymerizations. *Macromolecules* **2010**, *43* (8), 3699–3704. https://doi.org/10.1021/ma902653b.

(90) Brazel, C. S.; Rosen, S. L.; Rosen, S. L. *Fundamental Principles of Polymeric Materials*, Third edition.; John Wiley & Sons, Inc: Hoboken, N.J, 2012.

(91) Fouassier, J. P.; Allonas, X.; Laleve, J.; Dietlin, C. Photoinitiators for Free Radical Polymerization Reactions. In *Photochemistry and Photophysics of Polymer Materials*; Allen, N. S., Ed.; John Wiley & Sons, Inc.: Hoboken, NJ, USA, 2010; pp 351–419. https://doi.org/10.1002/9780470594179.ch10.

(92) Fouassier, J. P. *Photoinitiators*, 1st ed.; John Wiley & Sons, Ltd, 2021. https://doi.org/10.1002/9783527821297.

(93) Scherzer, T.; Tauber, A.; Mehnert, R. UV Curing of Pressure Sensitive Adhesives Studied by Real-Time FTIR-ATR Spectroscopy. *Vib. Spectrosc.* **2002**, *29* (1), 125–131. https://doi.org/10.1016/S0924-2031(01)00198-9.

(94) Williams, R. M.; Khudyakov, I. V.; Purvis, M. B.; Overton, B. J.; Turro, N. J. Direct and Sensitized Photolysis of Phosphine Oxide Polymerization Photoinitiators in the Presence and Absence of a Model Acrylate Monomer: A Time Resolved EPR, Cure Monitor, and PhotoDSC Study. *J. Phys. Chem. B* **2000**, *104* (44), 10437–10443. https://doi.org/10.1021/jp001348j.

(95) Tauber, A.; SCHERZER, T.; MEHNERT, R. UV Curing of Aqueous Polyurethane Acrylate Dispersions. A Comparative Study by Real-Time FTIR Spectroscopy and Pilot Scale Curing. *J. Coat. Technol.* **2000**, *72* (911), 51–60.

(96) Allen, N. *Photochemistry and Photophysics of Polymer Materials*; J. Wiley: Hoboken, N.J., 2010.

(97) Decker, C. The Use of UV Irradiation in Polymerization. *Polym. Int.* **1998**, *45* (2), 133–141. https://doi.org/10.1002/(SICI)1097-0126(199802)45:2<133::AID-PI969>3.0.CO;2-F.

(98) Studer, K.; Decker, C.; Beck, E.; Schwalm, R. Overcoming Oxygen Inhibition in UV-Curing of Acrylate Coatings by Carbon Dioxide Inerting: Part II. *Prog. Org. Coat.* **2003**, *48* (1), 101–111. https://doi.org/10.1016/S0300-9440(03)00149-8.

(99) Cramer, N. B.; O'Brien, C. P.; Bowman, C. N. Mechanisms, Polymerization Rate Scaling, and Oxygen Inhibition with an Ultra-Rapid Monovinyl Urethane Acrylate. *Polymer* **2008**, *49* (22), 6. https://doi.org/10.1016/j.polymer.2008.08.051.

(100) Imai, K.; Kaneko, Y. Preparation of Ammonium-Functionalized Polyhedral Oligomeric Silsesquioxanes with High Proportions of Cagelike Decamer and Their Facile Separation. *Inorg. Chem.* **2017**, *56* (7), 4133–4140. https://doi.org/10.1021/acs.inorgchem.7b00131.

(101) Alex, A. S.; Bhuvaneswari, S.; Sreenivas, N.; Sekkar, V.; Gouri, C. Short Silica Fibre-Reinforced Polymethylsilsesquioxane–Phenolic Interpenetrating Networks: Exploration for Use as Ablative Thermal Protection System in Aerospace. *Polym. Bull.* **2019**, *76* (8), 3941–3956. https://doi.org/10.1007/s00289-018-2579-4.

(102) Helleur, R.; Popovic, N.; Ikura, M.; Stanciulescu, M.; Liu, D. Characterization and Potential Applications of Pyrolytic Char from Ablative Pyrolysis of Used Tires. *J. Anal. Appl. Pyrolysis* **2001**, *58–59*, 813–824. https://doi.org/10.1016/S0165-2370(00)00207-2.

(103) Fu, J.; Shi, L.; Chen, Y.; Yuan, S.; Wu, J.; Liang, X.; Zhong, Q. Epoxy Nanocomposites Containing Mercaptopropyl Polyhedral Oligomeric Silsesquioxane: Morphology, Thermal Properties, and Toughening Mechanism. *J. Appl. Polym. Sci.* **2008**, *109* (1), 340–349. https://doi.org/10.1002/app.27917.

(104) Niemczyk, A.; Adamczyk-Tomiak, K.; Dziubek, K.; Czaja, K.; Rabiej, S.; Szatanik, R.; Dutkiewicz, M. Study of Polyethylene Nanocomposites with Polyhedral Oligomeric Silsesquioxane Nanofillers—from Structural Characteristics to Mechanical Properties and Processability. *Polym. Compos.* **2019**, *40* (S1). https://doi.org/10.1002/pc.24678.

(105) Döring, A.; Xiong, Y.; Li, Y.; Schneider, J.; Cherevkov, S. A.; Ushakova, E. V.; Rogach, A. L. Composite Nanospheres Comprising Luminescent Carbon Dots Incorporated into a Polyhedral Oligomeric Silsesquioxane Matrix. *J. Phys. Chem. C* **2021**, *125* (27), 15094–15102. https://doi.org/10.1021/acs.jpcc.1c04505.

(106) Gao, J.; Zhu, F. L.; Yang, J.; Liu, X. Synthesis and Curing Kinetics of UV-Curable Waterborne Bisphenol-S Epoxy-Acrylate/Polyurethane-Acrylate/Methylacryloylpropyl-POSS Nanocomposites. *J. Macromol. Sci. Part B* **2014**, *53* (12), 1800–1813. https://doi.org/10.1080/00222348.2014.970953.

(107) Karabiyik, U.; Paul, R.; Swift, M. C.; Satija, S. K.; Esker, A. R. Effects of POSS Nanoparticles on Glass Transition Temperatures of Ultrathin Poly(t-Butyl Acrylate) Films and Bulk Blends. *J. Polym. Sci. Part B Polym. Phys.* **2015**, *53* (3), 175–182. https://doi.org/10.1002/polb.23603.

(108) Qin, Y.; Bi, Y.; Ren, H.; Zhu, F.; Luo, M.; Zhang, L. Poly(Methyl Methacrylate)/Methacryl-POSS Nanocomposites with Excellent Thermal Properties. *Chin. J. Chem.* **2010**, *28* (12), 2527–2532. https://doi.org/10.1002/cjoc.201190033.

(109) Su, C.; Chiu, Y.; Teng, C.; Chiang, C. Preparation, Characterization and Thermal Properties of Organic-Inorganic Composites Involving Epoxy and Polyhedral Oligomeric Silsesquioxane (POSS). *J. Polym. Res.* **2010**, *17* (5), 673–681. http://dx.doi.org.ezproxy.proxy.library.oregonstate.edu/10.1007/s10965-009-9355-y.

(110) Xue, M.; Zhang, X.; Ma, L.; Gu, Z.; Lin, Y.; Bao, C.; Tian, X. Structure and Thermal Behavior of EPDM/POSS Composite Fibers Prepared by Electrospinning. *J. Appl. Polym. Sci.* **2013**, *128* (4), 2395–2401. https://doi.org/10.1002/app.38349.

(111) Yazıcı, N.; Dursun, S.; Yarıcı, T.; Kılıç, B.; Arıcan, M. O.; Mert, O.; Karaağaç, B.; Özkoç, G.; Kodal, M. The Outstanding Interfacial Adhesion between Acrylo-POSS/Natural Rubber Composites and Polyamide-Based Cords: 'An Environmentally Friendly Alternative to Resorcinol-Formaldehyde Latex Coating.' *Polymer* **2021**, *228*, 123880. https://doi.org/10.1016/j.polymer.2021.123880.

(112) Dong, Y.; He, J.; Yang, R. Phenolic Resin/Polyhedral Oligomeric Silsesquioxane (POSS) Composites: Mechanical, Ablative, Thermal, and Flame Retardant Properties. *Polym. Adv. Technol.* **2019**, *30* (8), 2075–2085. https://doi.org/10.1002/pat.4640.

(113) Han, Z.; Xi, Y.; Kwon, Y. Thermal Stability and Ablation Behavior of Modified Polydimethylsiloxane-Based Polyurethane Composites Reinforced with Polyhedral Oligomeric Silsesquioxane. *J. Nanosci. Nanotechnol.* **2016**, *16* (2), 1928–1933. https://doi.org/10.1166/jnn.2016.11986.

(114) Xi, Y.; Wang, L.; Kwon, Y. Thermal and Ablation Properties of Poly(Urethane-Isocyanurate)/Polyhedral Oligomeric Silsesquioxane Composites. *J. Nanosci. Nanotechnol.* **2016**, *16* (11), 11517–11522. https://doi.org/10.1166/jnn.2016.13543.

(115) Gao, J.; Dong, C.; Du, Y. Nonisothermal Curing Kinetics and Physical Properties of Unsaturated Polyester Modified with EA-POSS. *Int. J. Polym. Mater.* **2009**, *59* (1), 1–14. https://doi.org/10.1080/00914030903172866.

(116) Gu, J.-L.; Khil, M.-S.; Beom, K. K.; Gopiraman, M.; Song, K.-H.; Kim, I.-S. Effect of POSS Content on the Electrical, Thermal, Mechanical, and Wetting Properties of Electrospun Polyacrylonitrile (PAN)/POSS Nanofibrous Mats. *J. Exp. Nanosci.* **2016**, *11* (7), 500–511. https://doi.org/10.1080/17458080.2015.1087062.

(117) Kim, K.; Lichtenhan, J. D.; Otaigbe, J. U. Facile Route to Nature Inspired Hydrophobic Surface Modification of Phosphate Glass Using Polyhedral Oligomeric Silsesquioxane with Improved Properties. *Appl. Surf. Sci.* **2019**, *470*, 733–743. https://doi.org/10.1016/j.apsusc.2018.11.181.

(118) Pi, P.; Hou, K.; Wen, X.; Xu, S.; Cheng, J.; Xu, G.; Wang, S. A Facile One-Step Fabrication of Robust Superhydrophobic/Superoleophilic Cotton Fabric Using a Crosslinkable POSS-Containing Fluorinated Copolymer. *Prog. Org. Coat.* **2016**, *101*, 522–529. https://doi.org/10.1016/j.porgcoat.2016.09.023.

(119) Phillips, S. H.; Haddad, T. S.; Tomczak, S. J. Developments in Nanoscience: Polyhedral Oligomeric Silsesquioxane (POSS)-Polymers. *Curr. Opin. Solid State Mater. Sci.* **2004**, *8* (1), 21–29. https://doi.org/10.1016/j.cossms.2004.03.002.

(120) Kim, Y.; Choi, J. Thermal Ablation Mechanism of Polyimide Reinforced with POSS under Atomic Oxygen Bombardment. *Appl. Surf. Sci.* **2021**, *567*, 150578. https://doi.org/10.1016/j.apsusc.2021.150578.

(121) Wang, B.; Shi, M.; Ding, J.; Huang, Z. Polyhedral Oligomeric Silsesquioxane (POSS)-Modified Phenolic Resin: Synthesis and Anti-Oxidation Properties. *E-Polym.* **2021**, *21* (1), 316–326. https://doi.org/10.1515/epoly-2021-0031.

(122) Cozza, E. S.; Monticelli, O.; Marsano, E. Electrospinning: A Novel Method to Incorporate POSS Into a Polymer Matrix. *Macromol. Mater. Eng.* **2010**, *295* (9), 791–795. https://doi.org/10.1002/mame.201000214.

(123) Ganesh, V. A.; Nair, A. S.; Raut, H. K.; Tan, T. T. Y.; He, C.; Ramakrishna, S.; Xu, J. Superhydrophobic Fluorinated POSS–PVDF-HFP Nanocomposite Coating on Glass by Electrospinning. *J. Mater. Chem.* **2012**, *22* (35), 18479–18485. https://doi.org/10.1039/C2JM33088A.

(124) Song, X.; Li, T.; Cheng, B.; Xing, J. POSS–PU Electrospinning Nanofibers Membrane with Enhanced Blood Compatibility. *RSC Adv.* **2016**, *6* (70), 65756–65762. https://doi.org/10.1039/C6RA07681E.

(125) Xue, Y.; Wang, H.; Yu, D.; Feng, L.; Dai, L.; Wang, X.; Lin, T. Superhydrophobic Electrospun POSS-PMMA Copolymer Fibres with Highly Ordered Nanofibrillar and Surface Structures. *Chem. Commun.* **2009**, *0* (42), 6418–6420. https://doi.org/10.1039/B911509A.

(126) Zhan, X.; Wang, M.; Gao, T.; Lu, J.; He, Y.; Li, J. A Highly Selective Sorption Process in POSS-g-PDMS Mixed Matrix Membranes for Ethanol Recovery via Pervaporation. *Sep. Purif. Technol.* **2020**, *236*, 116238. https://doi.org/10.1016/j.seppur.2019.116238.

(127) Zhao, J.; Fu, Y.; Liu, S. Polyhedral Oligomeric Silsesquioxane (POSS)-Modified Thermoplastic and Thermosetting Nanocomposites: A Review.

Polym. Compos. **2008**, *16* (8), 18. https://doi.org/10.1177/096739110801600802.

(128) Gavande, V.; Im, D.; Lee, W.-K. Development of Highly Transparent UV-Curable Nylon 6 Nanofiber-Reinforced Polyurethane Acrylate Nanocomposite Coatings for Pre-Coated Metals. *J. Appl. Polym. Sci.* **2021**, *138* (26), 50614. https://doi.org/10.1002/app.50614.

(129) Kim, E. H.; Myoung, S. W.; Jung, Y. G.; Paik, U. Polyhedral Oligomeric Silsesquioxane-Reinforced Polyurethane Acrylate. *Prog. Org. Coat.* **2009**, *64* (2), 205–209. https://doi.org/10.1016/j.porgcoat.2008.07.026.

(130) Shukla, V.; Bajpai, M.; Singh, D. K.; Singh, M.; Shukla, R. Review of Basic Chemistry of UV-curing Technology. *Pigment Resin Technol.* **2004**, *33* (5), 272–279. https://doi.org/10.1108/03699420410560461.

(131) Kodaira, T.; Urushisaki, M.; Usugaya, M.; Ohora, K.; Okumura, M. Cyclopolymerization.20.Anionic Cyclopolymerization of N-Tert-Butyl-N-Allylacrylamide: Five-Membered Ring Formation through Head-to-Head and Tail-to-Tail Additions. *Macromolecules* **1994**, *27* (6), 1320–1324. https://doi.org/10.1021/ma00084a006.

(132) Urushisaki, M.; Kodaira, T.; Furuta, T.; Yamada, Y.; Oshitani, S. Cyclopolymerization. 25. Five-Membered Ring Formation through Head-to-Head and Tail-to-Tail Additions in Radical and Anionic Polymerizations of α-(Allyloxymethyl)Acrylates. *Macromolecules* **1999**, *32* (2), 322–327. https://doi.org/10.1021/ma981037v.

(133) Wang, Y.; Liu, F.; Xue, X. Synthesis and Characterization of UV-Cured Epoxy Acrylate/POSS Nanocomposites. *Prog. Org. Coat.* **2013**, *76* (5), 863–869. https://doi.org/10.1016/j.porgcoat.2013.02.007.

(134) Zhang, H.; Ou, J.; Wei, Y.; Wang, H.; Liu, Z.; Zou, H. A Hybrid Fluorous Monolithic Capillary Column with Integrated Nanoelectrospray Ionization Emitter for Determination of Perfluoroalkyl Acids by Nano-Liquid Chromatography–Nanoelectrospray Ionization-Mass Spectrometry/Mass Spectrometry. *J. Chromatogr. A* **2016**, *1440*, 66–73. https://doi.org/10.1016/j.chroma.2016.02.025.

(135) Li, J.; Luo, X.; Lin, X. Preparation and Characterization of Hollow Glass Microsphere Reinforced Poly(Butylene Succinate) Composites. *Mater. Des.* **2013**, *46*, 902–909. https://doi.org/10.1016/j.matdes.2012.11.054.

Appendices

Appendix A: Electrodeposition trial data

The data presented below is a brief representation of the results obtained from the ES trials. The metric to visual grade the curing of the samples that as followed:

- Uncured – samples that had no coating observed at all. This could be determined by scratching a small section of the film and evaluating if the coating was a viscous layer or a rigid cure coating.
- Semi-cured – samples that had some rigidity present. Even samples that the bottom section of the film was cured despite having agglomeration or gather present
- Cured – samples that were declared fully cured had little uncured material present and were almost dry to touch.
- N/A – no deposition present

The plot of the effect of the lamp type, shown in Figure A.1, had on the overall curing is displayed below with Xe lamp showing overall the best cure results when using EtOH solvent. In comparison to that, the ethanol solvent produced less fully cured samples than the THF solvent (Figure A.2). The mixed solvents were largely unsuccessful as well.

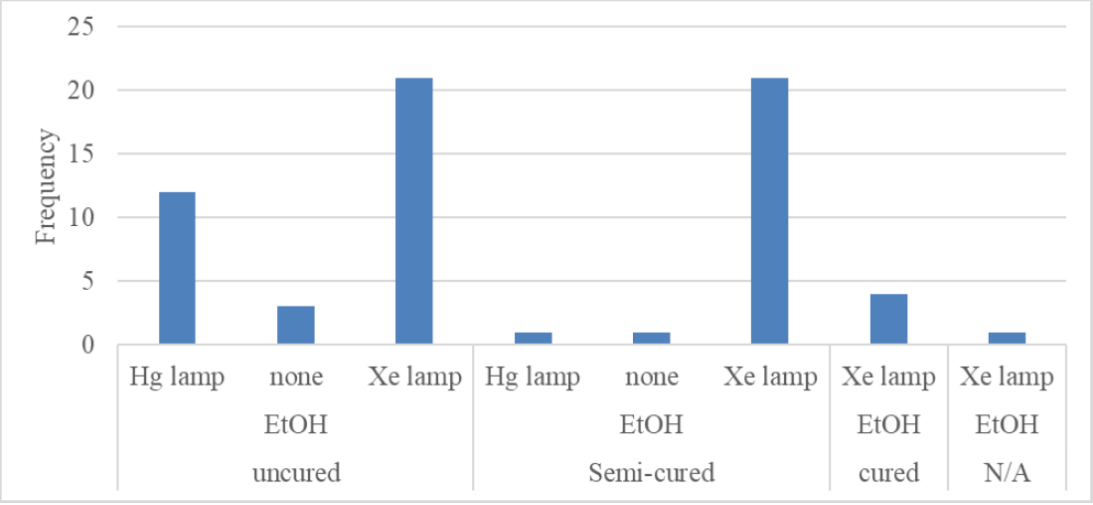

Figure A.1: Frequency for curing appearance based on UV lamp used for ethanol solution

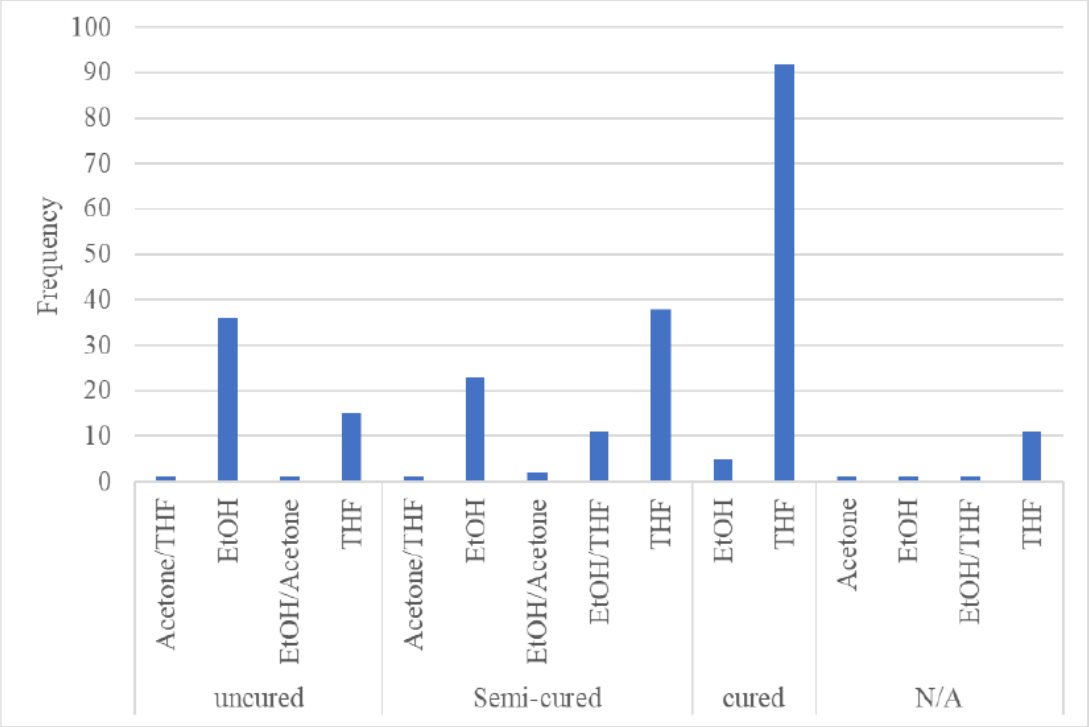

Figure A.2: Frequency in which an uncured, semi-cured, cured, or no deposition (N/A) occurred by solvents used

A comparison of the difference in the sparged in the solution is shown for ethanol in Figure A.3. The sample count of the non-sparged solution is higher, however, just judging the samples included within the cure field will show that, despite the lower sample size, more samples were cure by sparging the solution compared to using it without. The microfeature visual observed on the film using the naked eye is shown in Figure A.4. The stated within the result, the most common appearance was a bumpy film. This showed that the system was on average electrospraying or electrospinning beaded jet. The samples that were counted amongst the white deposits were the sparged films and the few ethanol samples created. A coating classification referred to samples that showed only a clear smooth coating that resemble the droplet cured samples. The drippage was included if the sample showed clear signs that it had gathered towards the bottom of the film collector. A smooth film was a sample without any prominent bumps.

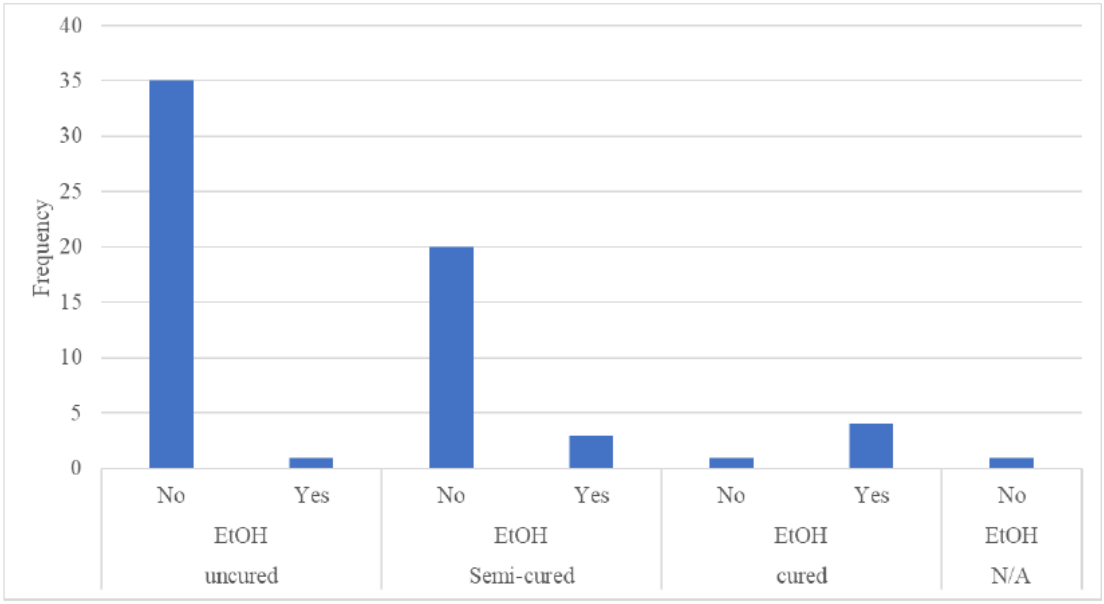

Figure A.3: Frequency in which a cured film formed for sparged ethanol (EtOH) solvent. Yes, refers to sparged solutions.

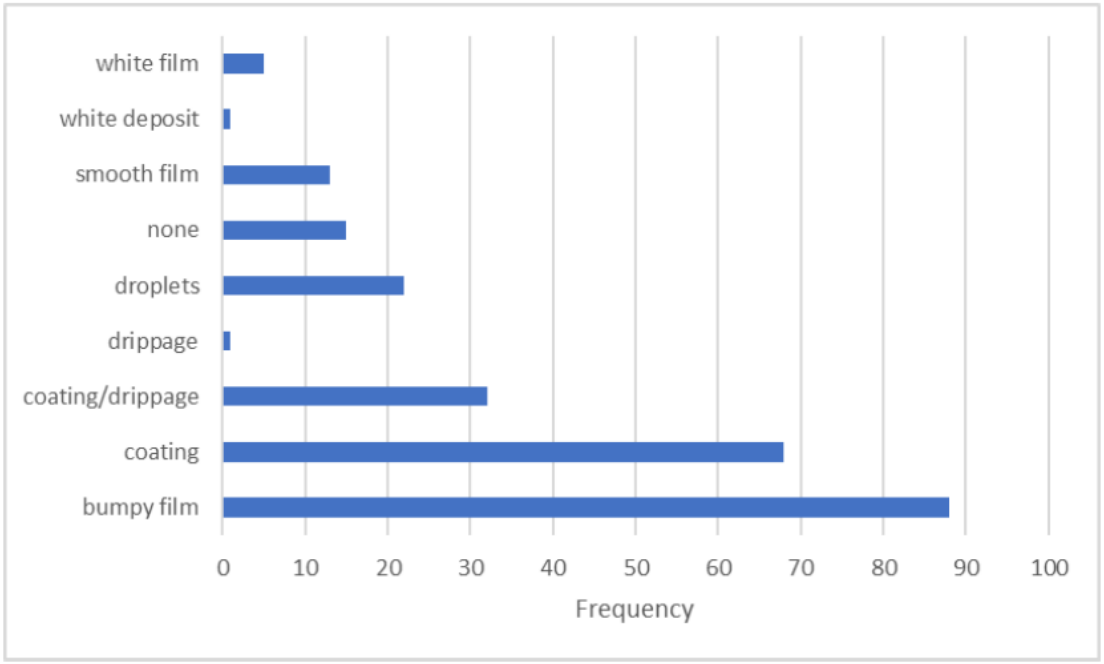

Figure A.4: Frequency of the characteristic visual deposition appearance

Appendix B. Distribution of the filler diameters

The filler diameter or length was obtained using images taken with the optical microscope and Image J Fiji (Figure B.5). The distribution of the fillers shows that each skewed more to the lower range of the distribution than the median. This is more pronounced with the HGMB. The range of the fillers and the median value are stated in Table B.1.

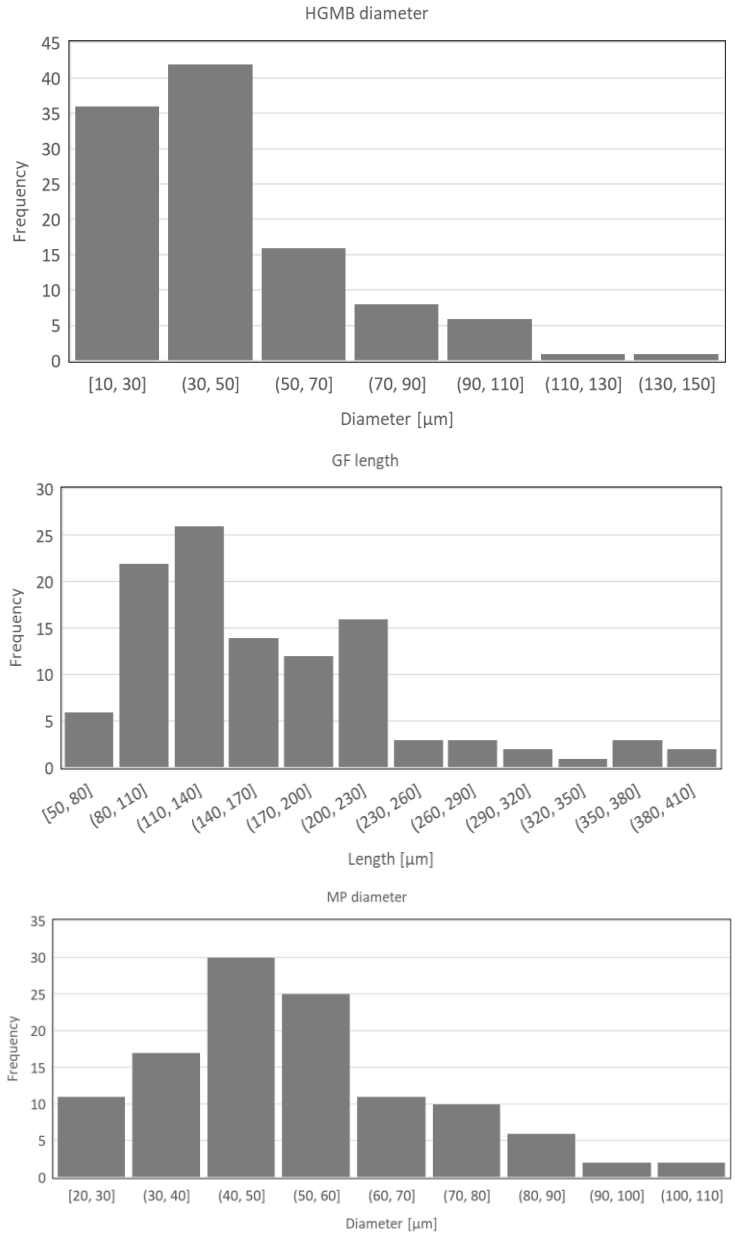

Figure B.5: Histogram of the length/diameter measurement for the filler materials using optical micrograph images. Sample size = 110.

Table B.1: Range and median value for filler distribution

Filler	Range [μm]	Median [μm]
HGMB	9.96 – 133.33	37.48
GF	51 – 392.66	143.39
MP	20.06 – 106.32	49.61

Appendix C. EDX thermal degradation analysis for the A-POSS/EB sample

The EDX samples were collected to compare the elemental values for A-POSS/EB samples before and after thermal degradation. The images of the section scanned are shown in Figure C.6. The two samples shown are not the same with the same areas but were separate sections of the same film. The before sample displays the only feature that was found on the smooth film produced.

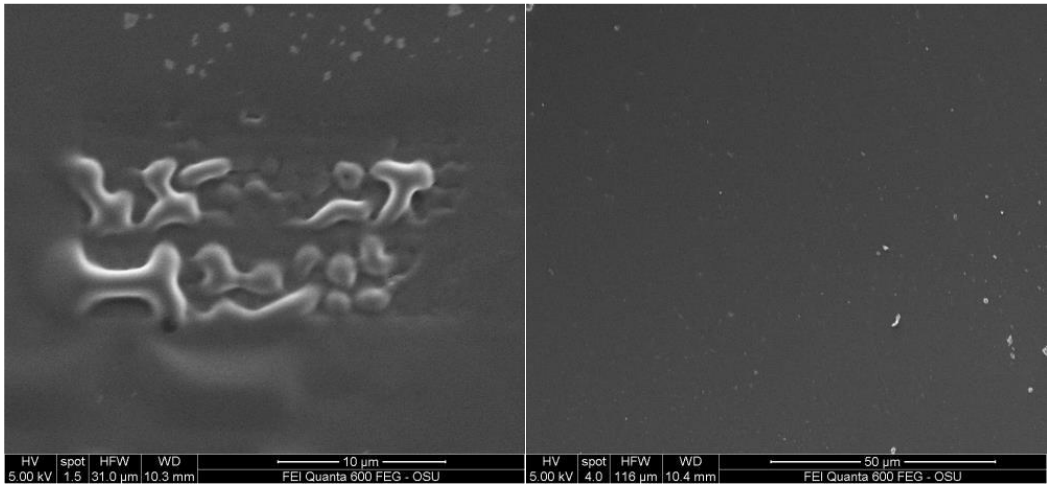

Figure C.6: SEM images of A-POSS/EB film before (left) and after (right) thermal degradation

Table C.2: EDX values for A-POSS/EB sample before and after TGA analysis

Sample	Element	Wt.%	At.%
A-POSS/EB	C K	73.76	80.57
	N K	1.87	1.75
	O K	14.63	14.63
	Si K	6.53	3.05
A-POSS/EB after TGA	C K	-	-
	N K	-	-
	O K	40.63	54.57
	Si K	59.37	45.43

From the EDX data (Figure C.7), there is a reduction in the carbon and oxygen peak, while there is an increase in silicon intensity. The weight percent of the carbon was approximately 75 percent of the sample area of the untested sample. After being measured in the TGA, the amount of silicon increased as expected in relation to the residual carbon and oxygen present. A comparison of the exact weight or atomic percent cannot be done unless carbon and nitrogen are excluded as there were not included in the EDX results for the degraded sample (Table C.2).

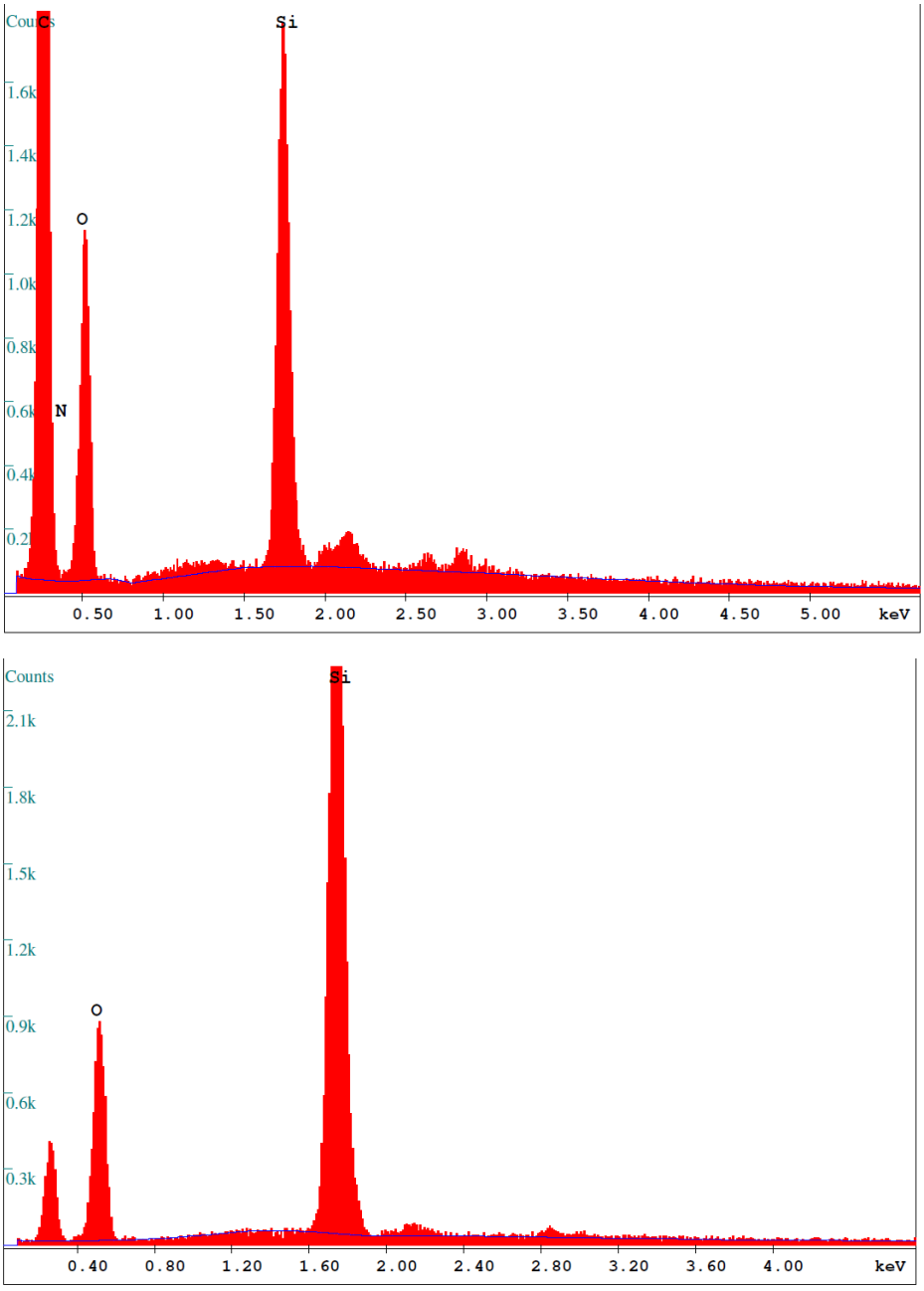

Figure C.7: EDX plots for A-POSS/EB sample before (top) and after (bottom) TGA analysis

Appendix D. Thermal analysis data for composites and fillers

Thermal degradation and heat flow measurements were taken for various samples to gain a better understanding of how that material will behave under thermal stress. The DSC data below was taken for the cast samples to compare the second heat curve for possible glass transition or melting point information. The full version of the curves depicted in Figure 4.40, is shown in Figure D.8.

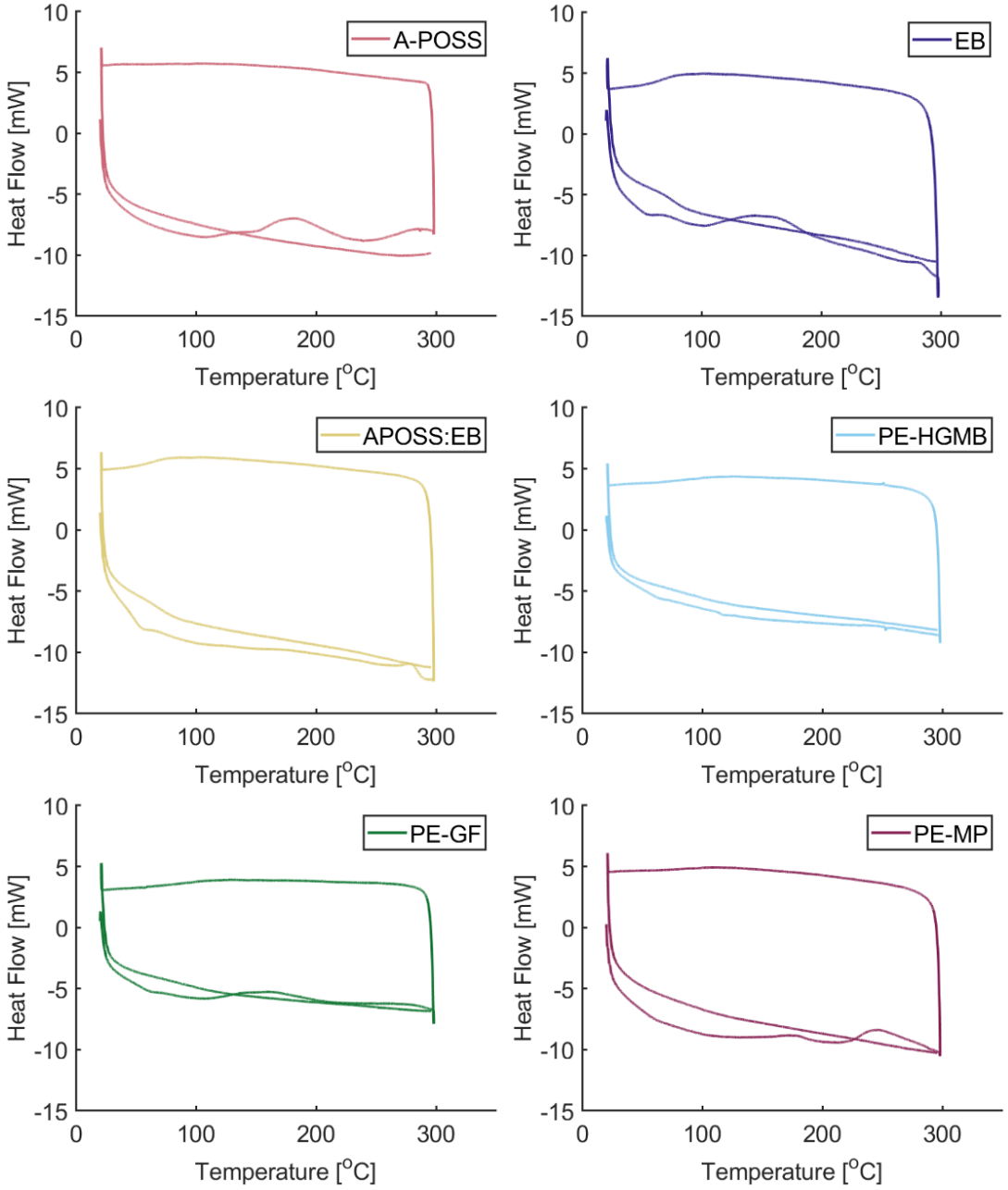

Figure D.8: DSC plots for the A-POSS, EB, A-POSS/EB cast samples

There is a potential crystallization peak with the A-POSS and EB samples that are observed on the first run. While there is a slight peak shown in the first run for the A-POSS/EB-MP and A-POSS/EB -GF samples, it can not be assumed to be anything significant. Glass transition (T_g) points are shown for the EB and A-POSS/EB samples and can be observed clearly in the second run for each sample.

The DSC for the sparged A-POSS/EB cured in THF is shown in Figure D.9. The first thing to notice is that there is a glass transition and crystallization peak present. It is hard to determine where the glass transition point starts with the initial downward slope showing a short dip. The second pass of the samples does not show any of the data observed in the first as the material already crystallized during the initial heating run.

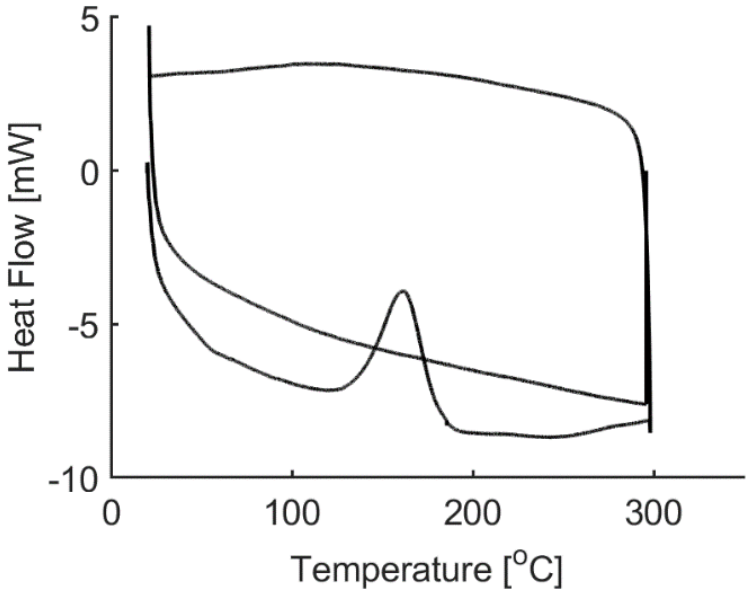

Figure D.9: DSC data for the A-POSS/EB cured in a THF solution (right)

Since not much data was found on the microphenosets, a TGA analysis (Figure D.10) was run to determine its thermal degradation behavior before it was incorporated into the A-POSS/ EB matrix. From the TGA data, an initial onset is observed below 100 ^{o}C. This is noticeable in the DTG data but not significant in the weight loss profile. The first major decrease is around 350 – 400 ^{o}C. This is quickly followed by another peak before a residual of 25 wt.% remains. Compared to the A-POSS/EB samples, the microphenoset had slightly less char residual.

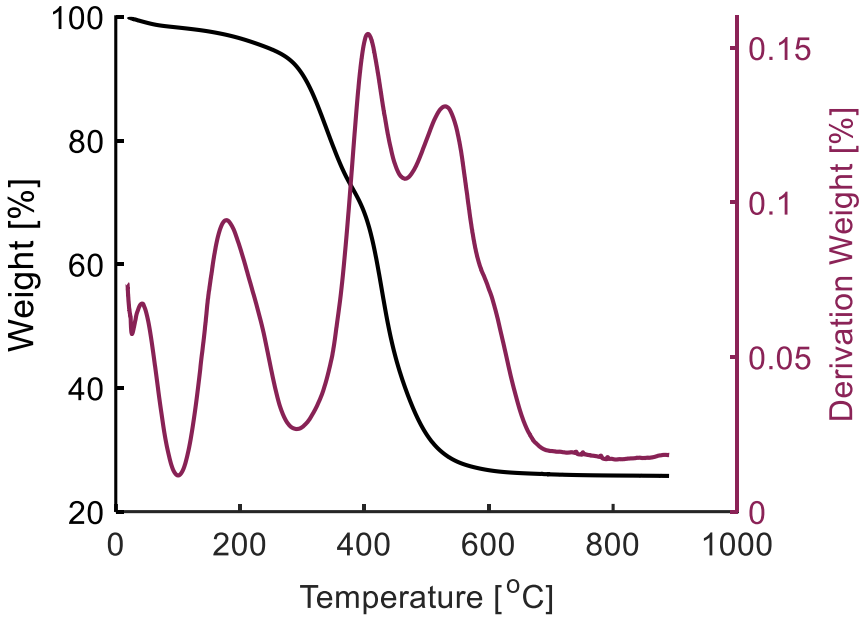

Figure D.10: TGA and DTG of the microphenoset (left)